Correlations in
Exotic Nuclear Matter

Dissertation zur Erlangung des Doktorgrads
der Naturwissenschaftlichen Fakultät
der Justus-Liebig-Universität Gießen
Fachbereich 07 - Mathematik und Informatik,
Physik, Geographie

vorgelegt von
Patrick Konrad
aus Wieseck

Gießen, Oktober 2009

D26

God does not play dice with the universe. He plays an ineffable game of his own devising, which might be compared, from the perspective of any of the other players, to being involved in an obscure and complex variant of poker in a pitch-dark room, with blank cards, for infinite stakes, with a Dealer who won't tell you the rules, and who smiles all the time.

– Terry Pratchett, Good Omens

Contents

1 Introduction

1.1 From SU(3) symmetry to flavor dynamics

Nuclear physics is a demanding field incorporating the dynamics of a quantum many-body system and accounting for the specific nature of the interacting entities namely mesons and baryons being governed by the strong interaction and the rules of quantum chromodynamics (QCD) [Ynd98]. The building blocks of QCD are the quarks and gluons. The bosonic gluons are responsible for the interaction of the fermionic quarks, which are the fundamental constituents of matter. There are six types of quarks, known as flavors, up (u), down (d), strange (s), charmed (c), top (t) and bottom (b). The up, charm and top quarks carry $+2/3$ and the down, strange and bottom carry $-1/3$ of the elementary charge. Therefore, the quarks are the only particles which have a fractional electric charge. The three lightest quarks, namely the u, d and s quark can be grouped together to a triplett. Mathematically the underlying symmetry can be described by the special unitary group SU(3) [A+08].

The main part of the visible matter in the universe consists of baryons, which are made out of three quarks. The baryons can be characterized by their rest mass and spin. Beyond that one introduces the quantum number isospin I and strangeness S. We note that in analogy to the spin, the total isospin is denoted with I, while the third component is denoted with I_3. The quantum numbers (I, I_3, S) for the u, d and s quarks are (I=1/2, I_3=1/2, S=0), (I=1/2, I_3=-1/2, S=0) and (I=0, I_3=0, S=-1), respectively. Baryons with almost same masses can be grouped together in multiplets. The dynamics of the u, d and s quark is mathematically also described by special unitary group SU(3). All multiplets can be formed out of the fundamental SU(3) triplett of u, d and s quarks and their antiparticles. As fermions, the baryons must fulfill the Pauli principle and have a antisymmetric wavefunction. If we restrict ourselves to the lowest mass states, i.e. the orbital angular momentum of the quarks $l = 0$, we have two options to couple the spins of the quarks. Since each of the quarks has spin $s = 1/2$, the total angular momentum of the baryons can be either $J = 1/2$ or $J = 3/2$. For the total angular momentum $J = 1/2$ and $J = 3/2$ we then obtain eight and ten possible states forming the baryon octet and decuplet, shown in Fig. 1.1. The particles are sorted from left to right with increasing isospin I_3 and from top to bottom with decreasing strangeness S. Stellar objects made out of dense baryonic matter is believed not only made out of proton and neutrons, but
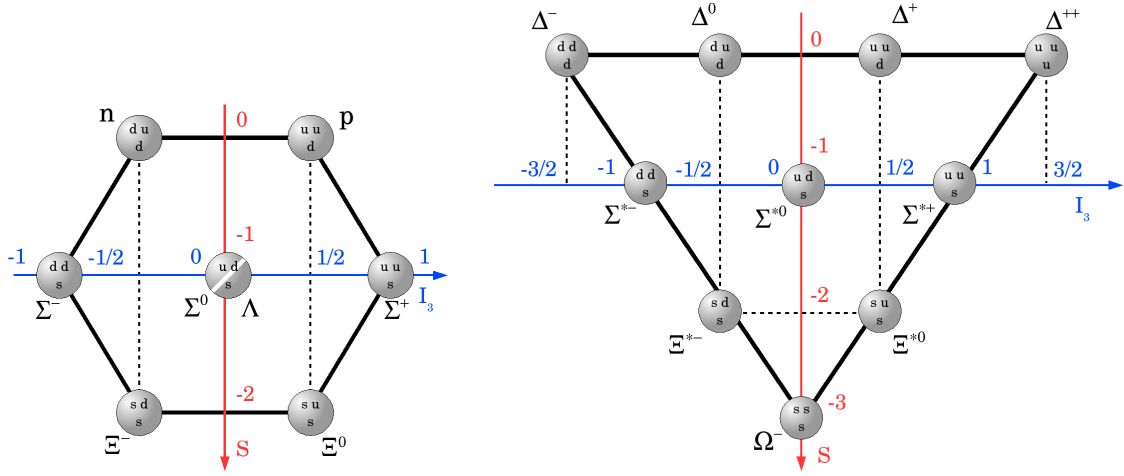
Figure 1.1: The left picture shows the baryon octet and the right picture the baryon decuplet.

also containing strange baryons, the hyperons. Due to the short lifetime of hyperons there are neither hyperon targets nor hyperon beams with proper energy available. Hypernuclei, where a hyperon is bound in the nuclear system, provide information on the YN and YY interaction. Since hyperons bound in a nucleus do not underlie the Pauli principle, the physics of hypernuclei provides also a good tool to examine the struture of nuclei. The first hypernucleus was observed in September 1952 [Wro04] by Marian Danysz and Jerzy Pniewski. They discovered nuclei with a Λ-hyperon by observing cosmic ray in emulsion chambers. Since that time, hypernuclei have been observed and studied in many experiments, such in (K^-, π^-) and (π^-, K^-) reactions at CERN, KEK, MAMI, JLAB and other facilities. At the future facility FAIR at GSI, PANDA will give new insights to $\Lambda\Lambda$-double-hypernuclei. Also the NUSTAR facility at FAIR will give access to exotic hypernuclei away from the β-stability line using rare isotope beams. In Fig. 1.2, the extension of the nuclear chart to strangeness is shown, where Λ-hypernuclei and $\Lambda\Lambda$-double-hypernuclei appears as an additional degree of freedom above the chart of pure isospin (i.e. p and n) nuclei.

Another source, which provides information on hypernuclear physics, is provided by the examination of neutron stars. Neutron stars are the smallest and densest compact objects bulit by matter known in the universe. Instead of consiting only of neutrons and protons, dense stellar objects, such as neutrons stars, may also contain a core of hyperons or quarks. A neutron star can be dived into the atmosphere, the outer crust, the inner crust an the outer and inner core, as shown in Fig. 1.3. But the specific composition of the inner of a neutron star, especially the inner core, is

Figure 1.2: The nuclear chart including known the hypernuclei. The picture is taken from "IX International Conference on Hypernuclear and Strange Particle Physics" at Johannes Gutenberg-Universität Mainz.

still an open question (see e.g. [Gle96, HPY07]) and is depending on the model. Neutron stars are formed during a supernova explosion, after the fusion reaction of massive stars reaches the endpoint of energy release, the core collapses. Under the immense gravitational force the matter is compressed to such high densities that nuclear and particle physics play an important role for their understanding. Neutrinos, for example, are important to understand the cooling of the neutron stars. Due to angular momentum conservation and the magnetic flux conservation, a fast rotating relict with high magnetic dipole field is left over as neutron star. This neutron star can be detected as the periodic signal of a pulsar. The basis for the calculation of neutron stars are the Tollman-Oppenheimer-Volkoff (TOV) equations [OV39], which shows that the maximum mass of a neutron star is directley connected with the equation of state of nuclear matter. A more stiff equation of state leads to a higher pressure, which then leads to more massive neutron star. The weak interaction allows the conversion of nucleon into hyperons which is energetically favorable because the Fermi energy of the highest lying nucleon will otherwise exceed the masses of the hyperons. Therefore, hyperons in many models necessary to bring maximum masses of the TOV equations down to the upper limit of neutrons stars of about 3 times the solar mass. In this work, we will point out the role of hyperons in infinite nuclear matter and their correlations.

Figure 1.3: Schematic structure of a neutron star according to [HPY07]. The picture is taken from http://commons.wikimedia.org.

1.2 From the independent particle model to short-range correlations

In recent years, the interest in correlations inside nuclei became an important issue in nuclear physics. Indeed, many properties such as binding energies of nuclei can be described by an independent particle model. In this model the many-body problem is reduced to a single particle moving in an overall potential. Historically, the independent particle model was introduced to describe the structure of atoms. The model of Hartree [Har28] and Fock [Foc30] is very successful in describing the shell structure of noble-gas atoms. In the Hartree-Fock method the electron is assumed to move in a single particle potential which is created by the Coulomb interaction with the other electrons and by itself. Later, the Hartree-Fock method was also applied to nuclear physics by Negele [Neg82] and [DG80] using effective interactions or energy-density functionals. Together with the shell model, many nuclear properties, such as the existence of magic nuclei with extra stability, spins and parities of the nuclear ground states as well as the existence of deformed nuclei could be explained by these calculations.

However, nucleon knockout experiments $A(e, e'p)X$ or $A(e, e'pp)X$, where on nucleon or two nucleons are knocked out from the target nucleus, show that the nucleons in a nucleus do not move independently [CdAPS91, DH90]. Fig. 1.4 shows the excitation energy spectrum of the reaction $^{12}C(e, e'p)^{11}B$ [dWH90]. The shell model calculation predicts that the $1s_{1/2}$ $(1/2^+)$, $1p_{3/2}$ $(3/2^-)$ and the $1p_{1/2}$ $(1/2^-)$ shells are occupied by the protons. The knockout of $1p$-protons leads to three final states, the $3/2^-$ ground state and the $1/2^-$ $(E_x = 2.125$ MeV$)$ and $3/2^-$ $(E_x = 5.020$ MeV$)$ excited states of ^{11}B. These states can clearly be seen in Fig. 1.4. However, there are also states for $(E_x > 6$ MeV$)$, corresponding to the knockout of protons populating the $2s_{1/2}$ $(1/2^+)$ and the $1d$ $(5/2^+, 3/2^+)$ states. This shows that correlations play an important role for understanding nuclear physics and we refer to [PSH97] for a
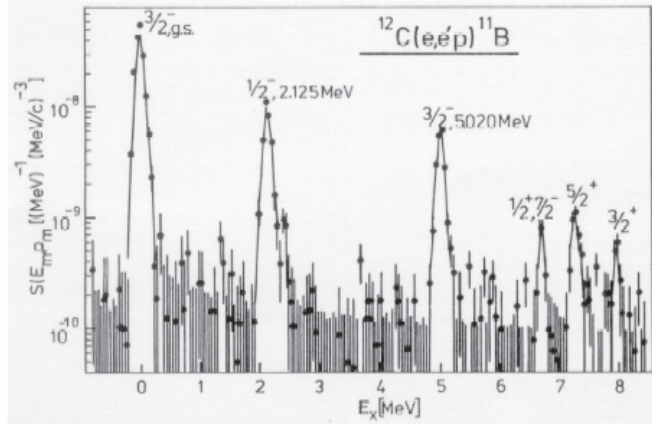
Figure 1.4: The spectral function found in the $^{12}C(e,e'p)^{11}B$ nucleon knockout reaction as a function of the excitation energy. (Figure taken from [dWH90])

more detailed discussion.

On the theoretical, side several calculations using different models including short-range correlation have been done for symmetric nuclear matter for temperature $T = 0$ (e.g. [RPD89, RDP91, BFF92]) and at finite temperature (e.g. [FLM03]). First results for asymmetric nuclear matter are reported in [Boz04, HM04, KLM05]. A good overview of theoretical models can be found in [DB04].

However, there is still not much known about the role of correlations of nucleons and hyperons in neutron star matter. The first calculation including correlations are done by [HJPRM96] and [RD04] for a single Λ in nuclear matter. But so far, no systematic investigations of their in infinite strange nuclear matter have been done. The aim of this work is to examine short-range correlations of nucleons and especially of Λ-hyperons in nuclear matter at extreme isospin and neutron star matter.

In chapter 2, we give a general introduction to the Green's function method, which provides a good basis for describing dynamical correlations. After the basic properties of the single particle Green's function we define the spectral function and we use perturbation theory to expand the single particle Green's functions in terms of the interaction. Finally, we show how the spectral function is connected to the self-energy. In our approach, correlations are included by the one-particle-two-hole (1p2h) and the two-particle-one-hole (2p1h) self-energy. For our calculations, we assume the interaction matrix element $\mathcal{M}$ to be independent of energy and momentum, which corresponds to a contact interaction. Lehr et al. [LEL+00, LLLM02] showed that this assumption leads to good results, which are in good agreement with other many-body calculations.

In our approach, the mean-field effects are included by the Skyrme parameterization of the energy density functional. In chapter 3 we discuss the parameterization. After the introduction of the basic ideas of the parameterization and different parameter sets, we discuss results for the equation of state, the effective mass and the effective potential for different sets of the Skyrme parameterizations.

The main idea of our approach is using a contact interaction matrix element. In chapter 4, we discuss how we calculate an average energy and momentum independent interaction matrix element. First we give an introduction to the Fermi liquid theory and Landau-Migdal parameters. Then we use the Landau-Migdal parameters to calculate an average interaction matrix element. Finally, we show results for the interaction matrix elements in nuclear matter.

Results for the dynamical correlation in nuclear matter are shown in chapter 5. We start the chapter with a short discussion of calculational details. Afterwards we show results for the self-energies, the spectral function and the momentum distribution for symmetric and asymmetric nuclear matter. In particular we point out how using different Skyrme parameterizations influence our results. At the end of the chapter, we introduce the quasiparticle strength, which we use to discuss results for correlations.

In chapter 6, we investigate results for dynamical correlations in hypernuclear matter. At the beginning of the chapter, we introduce an extension of the Skyrme parameterization to the strange sector. We show results for the equation of state, the effective mass and the effective potential as a function of the the strangeness fraction. Thereafter, we calculate the average interaction matrix element for the nucleons and Λ-hyperons. We show results for the imaginary part of the self-energy, the spectral function and the momentum distribution in hypernuclear matter with a certain strangeness fraction. At the end of the chapter, we discuss results in β-equilibrium. We show the influence using different Skyrme parameterizations to the fraction of particles. Finally, we discuss results for the imaginary part of the self-energy, the spectral function and the quasiparticle strength for different densities.

2 Introduction to the Green's Function Formalism

A very powerful concept of many-body theory is based on the fact, that one can approximately describe interacting many-body systems in terms of non-interacting "quasi-particles" plus appropriately chosen residual interactions. Since the theory of quasiparticles is very closely related to the theory of Green's functions, we introduce the basic ideas of Green's functions methods in this chapter. After introducing the basics definitions of the single particle Green's function, we discuss some analytic properties, which leads us to the definition of the spectral function. At the end we shortly discuss the perturbation expansion of the single particle Green's function. For a more detailed discussion of the Green's function methods and many-body theory we refer to [DVN05], [FW71] or [GR86].

2.1 The Single Particle Green's Function

The single particle Green's function $G(\vec{r}_1, t_1, \vec{r}_2, t_2)$ of a system of N interacting particles is given by means of the exact wave function Ψ_0^N and the field operators $\Psi_H(\vec{r}, t)$ and $\Psi_H^\dagger(\vec{r}, t)$ in the Heisenberg picture

$$G(\vec{r}_1, t_1, \vec{r}_2, t_2) = -\frac{i}{\hbar} \left\langle \Psi_0 \left| T \left\{ \Psi_H(\vec{r}_1, t_1) \Psi_H^\dagger(\vec{r}_2, t_2) \right\} \right| \Psi_0 \right\rangle. \tag{2.1}$$

We note that we define for simplicity $|\Psi_0\rangle \equiv |\Psi_0^N\rangle$. The creation operator $\Psi_H^\dagger(\vec{r}, t)$ attaches an additional particle at the space-time coordinate $(\vec{r}, t)$ to the ground state $|\Psi_0\rangle$, whereas the annihilation operator $\Psi_H(\vec{r}, t)$ removes a particle at the space-time coordinate $(\vec{r}, t)$ from the ground state. The time evolution of the creation operator $\Psi^\dagger(\vec{r})$ and annihilation operator $\Psi(\vec{r})$ in the Heisenberg picture is given by the relations

$$\Psi_H(\vec{r}, t) = e^{iHt/\hbar} \Psi(\vec{r}) e^{-iHt/\hbar}, \tag{2.2}$$

$$\Psi_H^\dagger(\vec{r}, t) = e^{-iHt/\hbar} \Psi^\dagger(\vec{r}) e^{iHt/\hbar}. \tag{2.3}$$

Since the Heisenberg ground state $|\Psi_0\rangle$, which we assume to be normalized, is the exact ground state of the Hamiltonian H, it fullfills the Schrödinger equation

$$H|\Psi_0\rangle = E|\Psi_0\rangle. \tag{2.4}$$

Finally, the time ordering operator T for fermions is defined by the relation

$$T\left\{\Psi(\vec{r}_1, t_1)\Psi^\dagger(\vec{r}_2, t_2)\right\} = \begin{cases} \Psi(\vec{r}_1, t_1)\Psi^\dagger(\vec{r}_2, t_2) \text{ for } t_1 > t_2 \\ -\Psi^\dagger(\vec{r}_2, t_2)\Psi(\vec{r}_1, t_1) \text{ for } t_1 < t_2 \end{cases}. \tag{2.5}$$

According to the definitions of the time ordering operator T, the Green's function is given by the propagation of a particle or hole depending on whether $t_1 > t_2$ or $t_1 < t_2$:

$$G(\vec{r}_1, t_1, \vec{r}_2, t_2) = \theta(t_1 - t_2)G^>(\vec{r}_1, t_1, \vec{r}_2, t_2) + \theta(t_2 - t_1)G^<(\vec{r}_1, t_1, \vec{r}_2, t_2). \tag{2.6}$$

Here we introduced the particle and hole correlation function

$$G^>(\vec{r}_1, t_1, \vec{r}_2, t_2) = -\frac{i}{\hbar}\langle\Psi_0|\Psi_H(\vec{r}_1, t_1)\Psi_H^\dagger(\vec{r}_2, t_2)|\Psi_0\rangle, \tag{2.7}$$

$$G^<(\vec{r}_1, t_1, \vec{r}_2, t_2) = \frac{i}{\hbar}\langle\Psi_0|\Psi_H^\dagger(\vec{r}_2, t_2)\Psi_H(\vec{r}_1, t_1)|\Psi_0\rangle. \tag{2.8}$$

The particle correlation function $G^>(\vec{r}_1, t_1, \vec{r}_2, t_2)$ denotes the propagation of an additional particle in the medium. Whereas the hole correlation function $G^<(\vec{r}_1, t_1, \vec{r}_2, t_2)$ denotes the propagation of a removed particle in the medium. Since for our next consideration this aspect does not play a role, we will consider the time-ordered Green's function.

2.2 The Spectral Representation

From the definition of the single particle Green's function Eq. (2.1), one can derive some interesting results which will lead us to the definition of the spectral function. Inserting a complete set of Heisenberg states between the field operators yields the expression

$$\begin{aligned} G(\vec{r}_1, t_1, \vec{r}_2, t_2) = -\frac{i}{\hbar}\Bigg\{ &\theta(t_1 - t_2)\sum_n\langle\Psi_0|\Psi_H(\vec{r}_1, t_1)|\Psi_n^{N+1}\rangle\langle\Psi_n^{N+1}|\Psi_H^\dagger(\vec{r}_2, t_2)|\Psi_0\rangle \\ &- \theta(t_2 - t_1)\sum_m\langle\Psi_0|\Psi_H^\dagger(\vec{r}_2, t_2)|\Psi_m^{N-1}\rangle\langle\Psi_m^{N-1}|\Psi_H(\vec{r}_1, t_1)|\Psi_0\rangle\Bigg\}. \end{aligned} \tag{2.9}$$

Here $|\Psi_n^{N+1}\rangle$ and $|\Psi_m^{N-1}\rangle$ are the states where a particle is added and removed from the ground state $|\Psi_0\rangle$ of the N-particle system, respectively. The included set of

state are assumed to be complete, and since the eigen-states are exact according to the full Hamiltonian H, they fullfill the Schrödinger equations

$$H|\Psi_n^{N+1}\rangle = E_n^{N+1}|\Psi_n^{N+1}\rangle, \tag{2.10}$$

$$H|\Psi_m^{N-1}\rangle = E_m^{N-1}|\Psi_m^{N-1}\rangle. \tag{2.11}$$

Using Eq. (2.3) together with Eq. (2.10) and Eq. (2.11) allows us to make the time dependence of the matrix elements explicit

$$G(\vec{r}_1, t_1, \vec{r}_2, t_2) = -\frac{i}{\hbar} \left\{ \theta(t_1 - t_2) \sum_n e^{-\frac{i}{\hbar}(E_n^{N+1} - E)(t_1 - t_2)} \right. \tag{2.12}$$

$$\times \langle\Psi_0|\Psi(\vec{r}_1)|\Psi_n^{N+1}\rangle\langle\Psi_n^{N+1}|\Psi^\dagger(\vec{r}_2)|\Psi_0\rangle$$

$$-\theta(t_2 - t_1) \sum_m e^{\frac{i}{\hbar}(E_m^{N-1} - E)(t_1 - t_2)}$$

$$\left. \times \langle\Psi_0|\Psi^\dagger(\vec{r}_2)|\Psi_m^{N-1}\rangle\langle\Psi_m^{N-1}|\Psi(\vec{r}_1)|\Psi_0\rangle \right\}.$$

For a translational invariant systems the single particle Green's function G will only depend on the differences in space $\vec{r}_1 - \vec{r}_2$ and time $t_1 - t_2$ and the Fourier transform of the single particle Green's function G is given by the expression

$$G(\vec{k}, \omega) = \int \mathrm{d}^3(\vec{r}_1 - \vec{r}_2) \int \mathrm{d}(t_1 - t_2) e^{-i\vec{k}\cdot(\vec{r}_1 - \vec{r}_2)} e^{i\omega(t_1 - t_2)} G(\vec{r}_1 - \vec{r}_2, t_1 - t_2). \tag{2.13}$$

After some algebra, where we use the integral representation for the step function

$$\theta(t_1 - t_2) = -\int_{-\infty}^{\infty} \frac{\mathrm{d}\omega}{2\pi i} \frac{e^{-i\omega(t_1 - t_2)}}{\omega + i\eta}, \tag{2.14}$$

we obtain the Lehmann representation [FW71, GR86] for the single particle Green's function

$$G(\vec{k}, \omega) = \frac{1}{\hbar} \sum_n \frac{\langle\Psi_0|\Psi(\vec{k})|\Psi_n^{N+1}\rangle\langle\Psi_n^{N+1}|\Psi^\dagger(\vec{k})|\Psi_0\rangle}{\omega - \mu/\hbar - w_n^{N+1} + i\eta} \tag{2.15}$$

$$+ \frac{1}{\hbar} \sum_m \frac{\langle\Psi_0|\Psi^\dagger(\vec{k})|\Psi_m^{N-1}\rangle\langle\Psi_m^{N-1}|\Psi(\vec{k})|\Psi_0\rangle}{\omega - \mu/\hbar - w_m^{N-1} - i\eta}.$$

Where μ denotes the chemical potential and $w_n^{N\pm 1} = \pm\frac{1}{\hbar}(E_n^{N\pm 1} - E)$ is the excitation energy of a $N+1$ and $N-1$ particle state, respectively. The convergences factor $\pm i\eta$ means that the limit $\eta \to 0^+$ is taken. Eq. (2.15) shows the the single particle Green's function $G(\vec{k}, \omega)$ is neither analytic in the upper nor in the lower complex ω plane. As shown in Fig. 2.1 the Green's function $G(\vec{k}, \omega)$ has a cut at $\mu/\hbar$. For
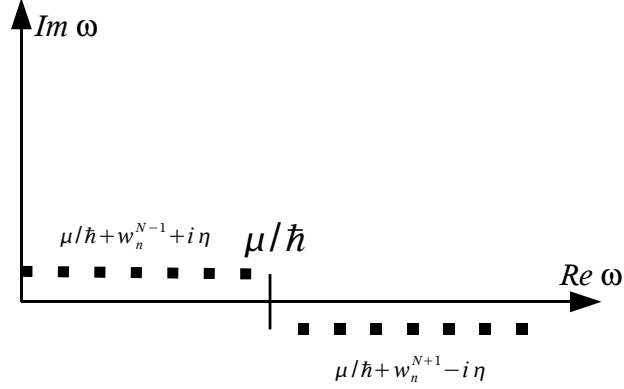
Figure 2.1: Singularities of the Green's function $G(\vec{k}, \omega)$ in the complex ω plane.

energies $\omega < \mu/\hbar$ we have poles in the upper complex ω plane at the exact eigen-energies of the $N-1$ particle states. Whereas for energies $\omega > \mu/\hbar$ we have poles in the lower complex plane at the exact eigen-energies of the $N+1$ particle state. For contour integration it is useful to consider a function analytic in one half of the plane. Therefore, we define the retarded and the advanced Green's function

$$G^{(r)}(\vec{r}_1, t_1, \vec{r}_2, t_2) = -\frac{i}{\hbar} \langle \Psi_0 | [\Psi_H(\vec{r}_1, t_1) \Psi_H^\dagger(\vec{r}_2, t_2)]_+ | \Psi_0 \rangle \theta(t_1 - t_2), \qquad (2.16)$$

$$G^{(a)}(\vec{r}_1, t_1, \vec{r}_2, t_2) = \frac{i}{\hbar} \langle \Psi_0 | [\Psi_H(\vec{r}_1, t_1) \Psi_H^\dagger(\vec{r}_2, t_2)]_+ | \Psi_0 \rangle \theta(t_1 - t_2). \qquad (2.17)$$

From that relation we immediately find

$$\left[G^{(r)}(\vec{r}_1, t_1, \vec{r}_2, t_2) \right]^* = G^{(a)}(\vec{r}_1, t_1, \vec{r}_2, t_2). \qquad (2.18)$$

The analytic properties of these function follow closely those of the time-ordered Green's function $G(\vec{r}_1, t_1, \vec{r}_2, t_2)$. After a Fourier transformation in the case of a homogenous system we obtain the retarded and advanced Green's function in the Lehmann representation

$$\begin{aligned} G^{(r,a)}(\vec{k}, \omega) =& \frac{1}{\hbar} \sum_n \frac{\langle \Psi_0 | \Psi(\vec{k}) | \Psi_n^{N+1} \rangle \langle \Psi_n^{N+1} | \Psi^\dagger(\vec{k}) | \Psi_0 \rangle}{\omega - \mu/\hbar - w_n^{N+1} \pm i\eta} \\ &+ \frac{1}{\hbar} \sum_m \frac{\langle \Psi_0 | \Psi^\dagger(\vec{k}) | \Psi_m^{N-1} \rangle \langle \Psi_m^{N-1} | \Psi(\vec{k}) | \Psi_0 \rangle}{\omega - \mu/\hbar - w_m^{N-1} \pm i\eta}. \end{aligned} \qquad (2.19)$$

Comparing Eq. (2.15) with Eq. (2.19) shows that the retarded, advanced and the time ordered Green's functions only differ in the convergence factors $\pm i\eta$, which

are important near the singularities. As discussed before, the time ordered Green's function is neither in the upper nor in the lower complex ω plane analytic, but as seen in Eq. (2.19), the retarded and advanced Green's functions are analytic in the upper and lower complex ω plane, respectively. If ω is real and greater than $\mu/\hbar$, then the convergence factors $\pm i\eta$ do not play a role. Therefore, we conclude for a real $\hbar\omega > \mu$

$$G^{(r)}(\vec{k}, \omega) = G(\vec{k}, \omega) \tag{2.20}$$

and

$$G^{(a)}(\vec{k}, \omega) = G(\vec{k}, \omega). \tag{2.21}$$

In thecase of a spectral distribution as e.g. in the thermodynamic limit, where the discrete index n can be replaced by an integration, Eq. (2.15) can be written (see [FW71]) as

$$G(\vec{k}, \omega) = \int\limits_0^\infty \frac{d\omega'}{2\pi} \left[\frac{\mathcal{A}_p(\vec{k}, \omega')}{\omega - \mu/\hbar - \omega' + i\eta} + \frac{\mathcal{A}_h(\vec{k}, \omega')}{\omega - \mu/\hbar + \omega' - i\eta} \right]. \tag{2.22}$$

Here $\mathcal{A}_h$ and $\mathcal{A}_h$ are the hole and the particle spectral function, respectively, defined as

$$\mathcal{A}_h(\vec{k}, \omega) = 2\pi \sum_n \left| \langle \Psi_n^{N-1} | \Psi(\vec{k}) | \Psi_0 \rangle \right|^2 \delta(\omega - w_n^{N-1}), \tag{2.23}$$

$$\mathcal{A}_p(\vec{k}, \omega) = 2\pi \sum_n \left| \langle \Psi_n^{N+1} | \Psi^\dagger(\vec{k}) | \Psi_0 \rangle \right|^2 \delta(\omega - w_n^{N+1}). \tag{2.24}$$

For the advanced and retarded Green's functions, we obtain the same results, except with other convergence factors:

$$G^{(r,a)}(\vec{k}, \omega) = \int\limits_0^\infty \frac{d\omega'}{2\pi} \left[\frac{\mathcal{A}_p(\vec{k}, \omega')}{\omega - \mu/\hbar - \omega' \pm i\eta} + \frac{\mathcal{A}_h(\vec{k}, \omega')}{\omega - \mu/\hbar + \omega' \pm i\eta} \right]. \tag{2.25}$$

As seen in Eq. (2.22), the time ordered, retarded and advanced Green's functions can be constructed out of the knowledge of the hole and particle spectral functions. Since the spectral functions also play an important role for our later discussion of correlations, we will examine some of its analytic properties.

2.3 Analytic Properties of the Spectral Function

As seen from the definition Eq. (2.23) and Eq. (2.24) the spectral functions are real and positive:

$$\mathcal{A}_h^*(\vec{k},\omega) = \mathcal{A}_h(\vec{k},\omega) \geq 0, \tag{2.26}$$

$$\mathcal{A}_p^*(\vec{k},\omega) = \mathcal{A}_p(\vec{k},\omega) \geq 0. \tag{2.27}$$

Since the excitation energies $w_n^{N\pm1} > 0$, we conclude from the definition of the spectral functions that

$$\mathcal{A}_h(\vec{k},\omega) = \mathcal{A}_p(\vec{k},\omega) = 0 \quad \text{for } \omega < 0. \tag{2.28}$$

Furthermore we use the symbolic expression valid for real ω

$$\frac{1}{\omega \pm i\eta} = \mathcal{P}\frac{1}{\omega} \mp i\pi\delta(\omega) \tag{2.29}$$

to rewrite Eq. (2.22) and Eq. (2.25) as

$$
\begin{aligned}
G(\vec{k},\omega) &= \int_0^\infty \frac{\mathrm{d}\omega'}{2\pi} \left[\frac{-\mathcal{A}_p(\vec{k},\omega')}{\omega' + \mu/\hbar - \omega - i\eta} + \frac{\mathcal{A}_h(\vec{k},\omega')}{\omega' + \omega - \mu/\hbar - i\eta} \right] \\
&= \mathcal{P}\int_0^\infty \frac{\mathrm{d}\omega'}{2\pi} \frac{\mathcal{A}_p(\vec{k},\omega')}{\omega - \mu/\hbar - \omega'} + \mathcal{P}\int_0^\omega \frac{\mathrm{d}\omega'}{2\pi} \frac{\mathcal{A}_h(\vec{k},\omega')}{\omega - \mu/\hbar + \omega'} \\
&\quad - \frac{i}{2}\mathcal{A}_p(\vec{k},\omega - \mu/\hbar) + \frac{i}{2}\mathcal{A}_h(\vec{k},\mu/\hbar - \omega).
\end{aligned} \tag{2.30}
$$

and

$$
\begin{aligned}
G^{(r,a)}(\vec{k},\omega) &= \int_0^\infty \frac{\mathrm{d}\omega'}{2\pi} \left[\frac{-\mathcal{A}_p(\vec{k},\omega')}{\omega' + \mu/\hbar - \omega \mp i\eta} + \frac{\mathcal{A}_h(\vec{k},\omega')}{\omega' + \omega - \mu/\hbar \pm i\eta} \right] \\
&= \mathcal{P}\int_0^\infty \frac{\mathrm{d}\omega'}{2\pi} \frac{\mathcal{A}_p(\vec{k},\omega')}{\omega - \mu/\hbar - \omega'} + \mathcal{P}\int_0^\infty \frac{\mathrm{d}\omega'}{2\pi} \frac{\mathcal{A}_h(\vec{k},\omega')}{\omega - \mu/\hbar + \omega'} \\
&\quad \mp \frac{i}{2}\mathcal{A}_p(\vec{k},\omega - \mu/\hbar) \mp \frac{i}{2}\mathcal{A}_h(\vec{k},\mu/\hbar - \omega)
\end{aligned} \tag{2.31}
$$

We now see that the imaginary part of the retarded Green's function is directly related to the spectral functions

$$\mathrm{Im}\left[G^{(r,a)}(\vec{k},\omega)\right] = \mp\frac{1}{2}[\mathcal{A}_p(\vec{k},\omega - \mu/\hbar) + \mathcal{A}_h(\vec{k},\mu/\hbar - \omega)] \equiv \mp\frac{1}{2}\mathcal{A}(\vec{k},\omega). \tag{2.32}$$

Here we introduced the sum of the particle and whole spectral functions as $\mathcal{A}(\vec{k}, \omega)$, corresponding to the total spectral function. From Eq. (2.28) and Eq. (2.32) follows that the spectral function is given by the particle and hole spectral function for $\omega > \mu/\hbar$ and $\omega < \mu/\hbar$

$$\mathcal{A}(\vec{k}, \omega) = \begin{cases} \mathcal{A}_p(\vec{k}, \omega - \mu/\hbar) & \text{for } \omega > \mu/\hbar \\ \mathcal{A}_h(\vec{k}, \mu/\hbar - \omega) & \text{for } \omega < \mu/\hbar \end{cases}. \tag{2.33}$$

From Eq. (2.31) and Eq. (2.32), the real part of the retarded and advanced Green's function the dispersion relation is found to be given by

$$\text{Re}\left[G^{(r,a)}(\vec{k}, \omega)\right] = \pm \frac{1}{2}\mathcal{P}\int\limits_{-\infty}^{\infty} \frac{d\omega'}{2\pi} \frac{\mathcal{A}(\vec{k}, \omega)}{\omega - \omega'}. \tag{2.34}$$

For our later considerations it is usefull to find relations between the spectral function and the hole and particle Green's functions. Therefore, we initially examine the case of a many-particle system at finite temperature T in the thermodynamic equilibrium and then take the limit $T \to 0$.

In the thermodynamic equilibrium, the Green's functions are defined as ensemble averages with respect to the grand canonical density operator $\rho = e^{-\beta(H-\mu N)}$ (see [KB62, BM90]). Where $\beta = 1/kT$ is the inverse temperature, $N = \Psi^\dagger \Psi$ the number operator and μ and H as before the chemical potential and the full interaction Hamiltonian, respectively. Using the cyclic invariance of the ensemble trace and the specific property from of the density operator leads to a relation between the particle and the hole correlation function

$$G^>(\vec{k}, \omega) = -e^{\beta(\hbar\omega-\mu)}G^<(\vec{k}, \omega). \tag{2.35}$$

With the definitions of the particle, the hole, the retarded and the advanced spectral function Eq. (2.7), Eq. (2.8), Eq. (2.16) and Eq. (2.17) we can rewrite Eq. (2.32) as

$$\mathcal{A}(\vec{k}, \omega) = -2\text{Im}\left[G^r(\vec{k}, \omega)\right] = i\left[G^r(\vec{k}, \omega) - G^r(\vec{k}, \omega)\right]$$
$$= i\left[G^>(\vec{k}, \omega) - G^<(\vec{k}, \omega)\right]. \tag{2.36}$$

We can make use of Eq. (2.35) and Eq. (2.36) to express the particle and hole Green's function by the spectral function $\mathcal{A}(\vec{k}, \omega)$

$$G^<(\vec{k}, \omega) = i\mathcal{A}(\vec{k}, \omega)f(\omega), \tag{2.37}$$
$$G^>(\vec{k}, \omega) = -i\mathcal{A}(\vec{k}, \omega)[1 - f(\omega)], \tag{2.38}$$
$$f(\omega) = \frac{1}{e^{\beta(\hbar\omega-\mu)} + 1}. \tag{2.39}$$

Here $f(\omega)$ denotes the Fermi distribution function for the energy ω, which becomes a step function for $T \to 0$.

2.4 Perturbation Expansion of the Single Particle Green's Function

In the last section, we defined the single particle Green's function and examined its properties. However, we still have to solve the many-body problem to obtain a solution for the Green's function. Since the general many-body problem might not be easy to solve, we have to develop appropriate techniques to obtain a solution. One procedure might be the perturbation expansion of the Green's function. The technical details of the derivation are a standard topic of many-body theory and discussed in many textbooks (see for example [DB04, FW71, GR86]), therefore we will just summarize some results.

Consider the time-dependent Hamiltonian with an adiabatic perturbation

$$H = H_0 + e^{-\epsilon|t|}H_1, \tag{2.40}$$

where ϵ is a small positive quantity. Starting from a large time in the past and going to a large time in future, the perturbation is adiabatically switched on. At large times in the past or in the future our problem reduces to the free Hamiltonian H_0 for which we can solve the problem. For the time $t = 0$ we obtain the full interacting Hamiltonian. Therefore, if we do the perturbation expansion of our problem and let the parameter ϵ tend to zero at the end, any meaningfull result will be independent of ϵ and we have solved the problem for the full interaction Hamiltonian H. After some lengthy calculation (e.g. [FW71]), we obtain the perturbation expansion of the time-ordered Green's function

$$G(\vec{r}_1, t_1, \vec{r}_2, t_2) = -\frac{i}{\hbar} \sum_{n=0}^{\infty} \left(\frac{-i}{\hbar}\right)^n \frac{1}{n!} \int\limits_{-\infty}^{\infty} dt_1 \cdots \int\limits_{-\infty}^{\infty} dt_n e^{-\epsilon(|t_1|+\cdots+|t_n|)}$$
$$\times \frac{\left\langle \Psi_0 \left| T \left\{ H_1(t_1) \cdots H_1(t_n) \Psi(\vec{r}_1, t_1)\Psi^\dagger(\vec{r}_2, t_2) \right\} \right| \Psi_0 \right\rangle}{\left\langle \Psi_0 \left| U_\epsilon(\infty, -\infty) \right| \Psi_0 \right\rangle} \tag{2.41}$$

where the time-evolution operator $U_\epsilon(t, t_0)$ is defined as

$$U_\epsilon(t, t_0) = \sum_{n=0}^{\infty} \left(\frac{-i}{\hbar}\right)^n \frac{1}{n!} \int\limits_{t_0}^{t} dt_1 \cdots \int\limits_{t_0}^{t} dt_n$$
$$\times e^{-\epsilon(|t_1|+\cdots+|t_n|)} \left\langle \Psi_0 \left| T \left\{ H_1(t_1) \cdots H_1(t_n) \right\} \right| \Psi_0 \right\rangle. \tag{2.42}$$

We note that the divergent formfactors $e^{-\epsilon(|t_1|+\cdots+|t_n|)}$ in Eq. (2.41) and Eq. (2.42) cancel each other and the limit $\epsilon \to 0$ can be taken. Eq. (2.41) shows how to expand the Green's function $G(\vec{r}_1, t_1, \vec{r}_2, t_2)$ in a series of fully contracted products of field operators in the interaction picture. This corresponds to an expansion in terms of the non-interacting Green's function $G_0(\vec{r}_1, t_1, \vec{r}_2, t_2)$. Wick's theorem (e.g. [FW71]) tells us how to evaluate this kind of expressions. Using Feynman rules, we can associate a physical interpretation in terms of diagrams with each term in the expansion. Using the Feyman rules from the appendix, we obtain for the Green's function at the lowest order $(n = 1)$

$$G(x_1, x_2) = \quad G_0(x_1, x_2) \quad + \quad G_1(x_1, x_2) \quad + \quad O(n = 2)$$

$$+ \qquad O(n = 2). \tag{2.43}$$

A detailed analysis shows that the Feynman diagrams can be classified into various contributions. The exact Green's function consists of the unperturbed Green's function plus all connected terms with a free Green's function at each end.

2.5 The Self-Energy

The self-energy is defined as any part of a Feynman diagram which is connected to the rest by two particle lines, where one is going in and one is going out. The expansion of the Green's function can then be expressed by the self-energy, which

leads to the Dyson equation

$$G(x_1, x_2) = \underset{x_2 \qquad\qquad\qquad x_1}{\rule{0pt}{0pt}} \tag{2.44}$$

$$= \underset{x_2 \qquad\qquad\qquad x_1}{\rule{0pt}{0pt}} + \underset{x_2 \quad y_2 \quad y_1 \quad x_1}{\boxed{\Sigma}} \quad,$$

where the double line corresponds to the full Green's function G, the single line to the unperturbed Green's function G_0 and the box to the self-energy Σ. The corresponding analytic expression to Eq. (2.44) is given by

$$G(x_1, x_2) = G_0(x_1, x_2) + \int d^4 y_1 \int d^4 y_2 G_0(x_1, y_1) \Sigma(y_1, y_2) G(y_2, x_2). \tag{2.45}$$

The analysis of the self-energy shows that it can be separated into various types of diagrams. All diagrams contributing to the self-energy and which can not be separated into sub-diagrams without cutting lines are called proper self-energies

$$\Sigma(x_1, x_2) = \Sigma^*(x_1, x_2) + \int d^4 y_1 \int d^4 y_2 \Sigma^*(x_1, y_1) G_{(y_1, y_2)} \Sigma^*(y_2, x_2) + \ldots . \tag{2.46}$$

Using these definitions, we can rewrite the Dyson equation Eq. (2.44) as

$$G(x_1, x_2) = \underset{x_2 \qquad\qquad\qquad x_1}{\rule{0pt}{0pt}} \tag{2.47}$$

$$= \underset{x_2 \qquad\qquad\qquad x_1}{\rule{0pt}{0pt}} + \underset{x_2 \quad y_2 \quad y_1 \quad x_1}{\boxed{\Sigma^*}} \quad.$$

Again corresponds the double line to the full Green's function G, the single line to the unperturbed Green's function G_0 and the box to the proper self-energy Σ^*. Finally, the analytic expression is given by

$$G(x_1, x_2) = G_0(x_1, x_2) + \int \mathrm{d}^4 y_1 \int \mathrm{d}^4 y_2 G_0(x_1, y_1) \Sigma^*(y_1, y_2) G(y_2, x_2). \qquad (2.48)$$

In a translational invariant system, the self-energy will only depend of the difference in the space coordinates and we can introduce the four dimensional Fourier transform of the self-energy

$$\Sigma^*(x_1, x_2) = \frac{1}{(2\pi)^4} \int \mathrm{d}^4 k\, e^{ik \cdot (x_1 - x_2)} \Sigma^*(k). \qquad (2.49)$$

Carring out the Fourier integrals in Eq. (2.48) leads to the Dyson equation

$$G(k) = G_0(k) + G_0(k) \Sigma^*(k) G(k) \qquad (2.50)$$

for which we can find the formal solution

$$G(k) = \frac{1}{[G_0(k)]^{-1} - \Sigma^*(\vec{k}, \omega)}. \qquad (2.51)$$

The unperturbed Green's function G_0 is defined by the relation

$$\left(\hbar\omega - \epsilon_0(\vec{k}) \right) G_0(k) = 1, \qquad (2.52)$$

where $\epsilon_0(\vec{k})$ is the energy of a free particle. We replace the inverse of the unperturbed Green's function by

$$[G_0(k)]^{-1} = \hbar\omega - \epsilon_0(\vec{k}) \qquad (2.53)$$

and obtain for Eq. (2.51)

$$G(k) \equiv G(\vec{k}, \omega) = \frac{1}{\hbar\omega - \epsilon_0(\vec{k}) - \Sigma^*(\vec{k}, \omega)}. \qquad (2.54)$$

In analogy to the time-ordered Green's function we can also define the retarded and advanced self-energy. Using the Dyson equation for the retarded and advanced Green's function we obtain

$$G^{(r,a)}(k) = G_0^{(r,a)}(k) + G_0^{(r,a)}(k) \Sigma^{*(r,a)}(k) G^{(r,a)}(k). \qquad (2.55)$$

Here $\Sigma^{*(r)}$ and $\Sigma^{*(a)}$ are the retarded and advanced self-energy, respectively. The causal, retarded and advanced self-energy are quite different functions, but they are related in a simple manner. Comparing Eq. (2.30) with Eq. (2.31) shows that the

real and the imaginary parts of the retarded and time-ordered Green's functions are related by

$$\mathrm{Re}\left[G^{(r)}(\vec{k}, \omega)\right] = \mathrm{Re}\left[G(\vec{k}, \omega)\right] \tag{2.56}$$

and

$$\mathrm{Im}\left[G^{(r)}(\vec{k}, \omega)\right] = \begin{cases} \mathrm{Im}\left[G(\vec{k}, \omega)\right] & \text{for } \omega > \mu/\hbar \\ -\mathrm{Im}\left[G(\vec{k}, \omega)\right] & \text{for } \omega < \mu/\hbar \end{cases}. \tag{2.57}$$

Therefore we can conclude [Nol02] that the same relations should hold for the time ordered and retarded self-energy:

$$\mathrm{Re}\left[\Sigma^{*(r)}(\vec{k}, \omega)\right] = \mathrm{Re}\left[\Sigma^{*}(\vec{k}, \omega)\right] \tag{2.58}$$

and

$$\mathrm{Im}\left[\Sigma^{*(r)}(\vec{k}, \omega)\right] = \begin{cases} \mathrm{Im}\left[\Sigma^{*}(\vec{k}, \omega)\right] & \text{for } \omega > \mu/\hbar \\ -\mathrm{Im}\left[\Sigma^{*}(\vec{k}, \omega)\right] & \text{for } \omega < \mu/\hbar \end{cases}. \tag{2.59}$$

Furthermore, the Lehmann representation [FW71] ensures that for real ω

$$\mathrm{Im}\left[\Sigma^{*}(\vec{k}, \omega)\right] \geq \quad \text{for } \omega < \mu/\hbar, \tag{2.60}$$

$$\mathrm{Im}\left[\Sigma^{*}(\vec{k}, \omega)\right] \leq \quad \text{for } \omega > \mu/\hbar. \tag{2.61}$$

From the sign change at $\omega < \mu/\hbar$ it follows that $\mathrm{Im}\left[\Sigma^{*}(\vec{k}, \mu/\hbar)\right] = 0$, which reflects the stability of the ground state.

2.6 Dynamical Correlations

In the previous sections, we developed the formulation of many-body theory in terms of the Green's function G_0 and we showed that all information on the interacting systems is contained in the spectral function $\mathcal{A}$. In principle we could write down the self-energy and solve the Dyson equation. But in practical applications, one has always to introduce cut-offs at a limited number of terms. It also might not be sufficient to approximate a strongly interacting system by a nth-order approximation of the self-energy, since higher order correlations might have contributions to the results. But we can make use of a hierarchal scheme of the Green's function. For a first approximation of the Dyson equation we replace the fully interacting Green's

function on the right hand side of Eq. (2.50) by the free Green's function G_0, which is then used as an approximation for the next step. In this way, we make sure that with a rising number of approximations the system contains more information on higher order correlations:

$$
\begin{aligned}
G_1(k) &= G_0(k) + G_0(k)\Sigma^*(k)G_0(k), \\
G_2(k) &= G_0(k) + G_0(k)\Sigma^*(k)G_1(k), \\
&\vdots \\
G_n(k) &= G_0(k) + G_0(k)\Sigma^*(k)G_{n-1}(k).
\end{aligned}
\tag{2.62}
$$

We note that also the self-energy $\Sigma^*(k)$ contains the Green's function $G_0(k)$. In terms of Feynman diagrams, this means a summation of all diagrams at a certain order. By replacing all free Green's function G_0 by the Green's function G of the fully interacting system, it is possible to solve the many-body problem self-consistently.

For a system of particles interacting by the two-body interaction $V(\vec{r}_1 - \vec{r}_2)$, we can write down the first order of the self-energy using Feynman rules as

$$
\Sigma^*(x_1, x_2) = \tag{2.63}
$$

$$
\begin{aligned}
= -i\hbar\delta(t_1 - t_2)[\delta(\vec{r}_1 - \vec{r}_2) \int \mathrm{d}^3 x_3 G(\vec{r}_3, t_3, \vec{r}_3, t_3^+)V(\vec{r}_1 - \vec{r}_3) \\
- V(\vec{r}_1 - \vec{r}_2)G(\vec{r}_1, t_1, \vec{r}_2, t_1^+)].
\end{aligned}
$$

We note that we, as discussed before, replaced all free Green's G_0 function by the fully interacting Green's function G. Making use of the hierarchal scheme we can solve the problem self-consistently. It can be shown that this approximation is equivalent to the mean-field or Hatree-Fock approximation [Kon04, DVN05]. Since the self-energy Eq. (2.63) is local in time, a particle feels the other particles just by an effective static energy-independent potential [DVN05].

For the second order contribution $n = 2$ there are two diagrams left, which can not be obtained by summation of other diagrams. These terms contribute to the polarization of the medium and, as we will see later, can be interpreted as collision

terms,

$$\Sigma_C(x_1, x_2) = \qquad \qquad \qquad \qquad + \qquad \qquad \qquad \qquad .$$

$$(2.64)$$

The analytic expression of the diagram on the left side is given by

$$
\Sigma_d(x_1, x_2) = g\hbar^2 \int \mathrm{d}^3 r_3 \int \mathrm{d}^3 r_4 V(\vec{r}_2 - \vec{r}_4) V(\vec{r}_1 - \vec{r}_3)
$$
$$
\times \left. [G(x_1, x_2) G(x_4, x_3) G(x_3, x_4)] \right|_{t_1 = t_3, t_2 = t_4} \qquad (2.65)
$$

and the exchange diagram on the right side is given by

$$
\Sigma_e(x_1, x_2) = -g\hbar^2 \int \mathrm{d}^3 r_3 \int \mathrm{d}^3 r_4 V(\vec{r}_2 - \vec{r}_4) V(\vec{r}_1 - \vec{r}_3)
$$
$$
\times \left. [G(x_3, x_2) G(x_4, x_3) G(x_1, x_4)] \right|_{t_1 = t_3, t_2 = t_4}, \qquad (2.66)
$$

where g is the number of degenerated states. In contrast to the mean-field contribution Eq. (2.63), this polarization self-energy is not local in time. Therefore, we split, in analogy to the Green's function Eq. (2.6), the contribution to the polarization self-energy into two parts, whether $t_1 > t_2$ or $t_2 < t_1$

$$
\Sigma_C(x_1, x_2) = \theta(t_1 - t_2) \Sigma^>(x_1, x_2) + \theta(t_2 - t_1) \Sigma^<(x_1, x_2). \qquad (2.67)
$$

According to the Feynman rules we obtain for the polarization self-energy in energy-momentum space

$$\Sigma^>(\vec{k}, \omega) = \qquad \qquad \qquad + \qquad \qquad \qquad$$

$$
= -g \frac{i^2 \hbar^2}{(2\pi)^8} \int \mathrm{d}^3 k_2 \mathrm{d}\omega_2 \int \mathrm{d}^3 k_3 \mathrm{d}\omega_3 \int \mathrm{d}^3 k_4 \mathrm{d}\omega_4 \quad \delta^3(\vec{k} + \vec{k}_2 - \vec{k}_3 - \vec{k}_4)
$$
$$
\times \delta(\omega + \omega_2 - \omega_3 - \omega_4) \left[(V(k - k_3)^2 - V(k - k_3) V(k - k_4) \right]
$$
$$
\times G_0^<(\vec{k}_2, \omega_2) G_0^>(\vec{k}_3, \omega_3) G_0^>(\vec{k}_4, \omega_4) \qquad (2.68)
$$

and

$$\Sigma^<(\vec{k}, \omega) = -g \frac{i^2 \hbar^2}{(2\pi)^8} \int \mathrm{d}^3 k_2 \mathrm{d}\omega_2 \int \mathrm{d}^3 k_3 \mathrm{d}\omega_3 \int \mathrm{d}^3 k_4 \mathrm{d}\omega_4 \quad \delta^3(\vec{k} + \vec{k}_2 - \vec{k}_3 - \vec{k}_4)$$
$$\times \, \delta(\omega + \omega_2 - \omega_3 - \omega_4) \left[V(k - k_3)^2 - V(k - k_3)V(k - k_4) \right]$$
$$\times \, G_0^>(\vec{k}_2, \omega_2) G_0^<(\vec{k}_3, \omega_3) G_0^<(\vec{k}_4, \omega_4). \tag{2.69}$$

Because of the symmetry of the integrand and limits in respect of k_3 and k_4, the transformation

$$V(k - k_3)^2 - V(k - k_3)V(k - k_4) = \frac{1}{2} \left[V(k - k_3) - V(k - k_4) \right]^2 \tag{2.70}$$

under the integral is allowed. Since the two diagrams Eq. (2.68) and Eq. (2.69) contain different potentials in the integrand, but have the same Green's function structure, we can make use of Eq. (2.70) to write down Eq. (2.68) and Eq. (2.69) in a more compact way:

$$\Sigma^>(\vec{k}, \omega) = g \frac{\hbar^2}{(2\pi)^8} \int \mathrm{d}^3 k_2 \mathrm{d}\omega_2 \int \mathrm{d}^3 k_3 \mathrm{d}\omega_3 \int \mathrm{d}^3 k_4 \mathrm{d}\omega_4 \quad \delta^3(\vec{k} + \vec{k}_2 - \vec{k}_3 - \vec{k}_4)$$
$$\times \, \delta(\omega + \omega_2 - \omega_3 - \omega_4) \mid \mathcal{M} \mid^2$$
$$\times \, G_0^<(\vec{k}_2, \omega_2) G_0^>(\vec{k}_3, \omega_3) G_0^>(\vec{k}_4, \omega_4) \tag{2.71}$$

and

$$\Sigma^<(\vec{k}, \omega) = g \frac{\hbar^2}{(2\pi)^8} \int \mathrm{d}^3 k_2 \mathrm{d}\omega_2 \int \mathrm{d}^3 k_3 \mathrm{d}\omega_3 \int \mathrm{d}^3 k_4 \mathrm{d}\omega_4 \quad \delta^3(\vec{k} + \vec{k}_2 - \vec{k}_3 - \vec{k}_4)$$
$$\times \, \delta(\omega + \omega_2 - \omega_3 - \omega_4) \mid \mathcal{M} \mid^2$$
$$\times \, G_0^>(\vec{k}_2, \omega_2) G_0^<(\vec{k}_3, \omega_3) G_0^<(\vec{k}_4, \omega_4), \tag{2.72}$$

where we introduced the matrix element

$$\mid \mathcal{M} \mid^2 \equiv \frac{1}{2} \left[V(k - k_3) - V(k - k_4) \right]^2. \tag{2.73}$$

21

We note that in Eq. (2.71) and Eq. (2.72) the exchange terms are now included in the matrix element $| \mathcal{M} |^2$. Since in the expression of $\Sigma^>$ appear two particle and one hole Green's function, $\Sigma^>$ is called a two-particle-one-hole (2p1h) self-energy. In the same manner, $\Sigma^<$ is called a one-particle-two-hole (1h2p) self-energy.

We can find a physical interpretation For $\Sigma^{\gtrless}$ [KB62, Kon04]. Consider a particle with energy ω and momentum $\vec{k}$, colliding with a particle having the energy ω_2 and momentum $\vec{k}_2$. After the collision, the particles have the energies ω_3 and ω_4 and the momenta $\vec{k}_3$ and $\vec{k}_4$:
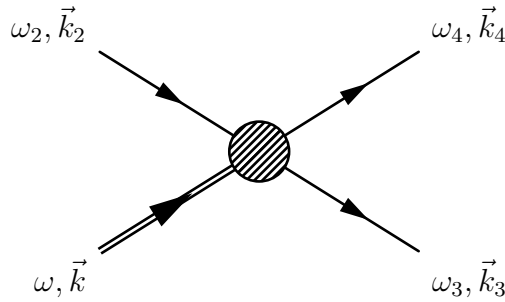
In the Born approximation, the differential cross section is then given by $[V(k - k_3) - V(k - k_4)]^2$ [KB62] times a delta function to conserve energy and momentum . To obtain a scattering rate, we have to multiply the differential cross section by the density of incoming particles and outcoming particles and integrate over all internal degrees of freedom. This procedure leads to Eq. (2.71). Therefore, we can interprete the (1p2h) polarization self-energy $\Sigma^>$ as a scattering-out rate. In the same manner, the (2p1h) polarization self-energy $\Sigma^<$ can be interpreted as a scattering-in rate. In this case two particles with the energies ω_3 and ω_4 and momenta $\vec{k}_3$ and $\vec{k}_4$ scatter into states with energies ω and ω_2 and momenta $\vec{k}$ and $\vec{k}_2$:
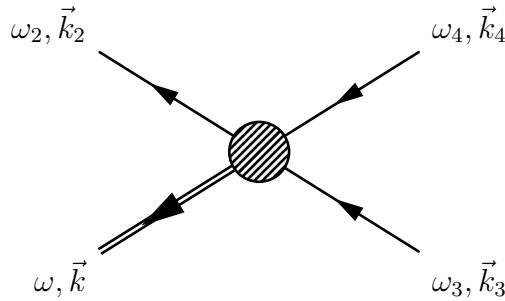
2.7 Calculation of the Spectral Function $\mathcal{A}$

In the case of an infinite medium, as it is the case for nuclear matter, all quantities will only depend on the absolute value of the momentum. It follows from Eq. (2.55), that the retarded Green's function is given by the relation

$$G^{(r)}(k,\omega) = \frac{1}{\hbar\omega - \frac{\hbar^2 k^2}{2m} - \Sigma^{(r)}(k,\omega)}. \tag{2.74}$$

Further analysis of the self-energy shows that it consists of a local and a non-local part. The local part can be identified with the mean-field, whereas the non-local part can be identified with the collisional part:

$$\Sigma^{(r)}(k,\omega) = \Sigma_{MF}(k) + \Sigma_C(k,\omega). \tag{2.75}$$

We will discuss the mean-field part in more detail in the following chapter. As seen in Eq. (2.67), the collisional part of the self-energy can be expressed by the two-particle-one-hole (2p1h) and the one-particle-one-hole (1p2h) self-energies:

$$\Sigma^{>}(k,\omega) = -ig\frac{\hbar^2}{(2\pi)^8} \mid \mathcal{M} \mid^2 \int d^3k_2 d\omega_2 \int d^3k_3 d\omega_3 \int d^3k_4 d\omega_4 \quad \delta^3(k + k_2 - k_3 - k_4)$$
$$\times \delta(\omega + \omega_2 - \omega_3 - \omega_4)\mathcal{A}(k_2,\omega_2)f(\omega_2)$$
$$\times \mathcal{A}(k_3,\omega_3)\left[1 - f(\omega_3)\right]\mathcal{A}(k_4,\omega_4)\left[1 - f(\omega_4)\right], \tag{2.76}$$

$$\Sigma^{<}(k,\omega) = ig\frac{\hbar^2}{(2\pi)^8} \mid \mathcal{M} \mid^2 \int d^3k_2 d\omega_2 \int d^3k_3 d\omega_3 \int d^3k_4 d\omega_4 \quad \delta^3(k + k_2 - k_3 - k_4)$$
$$\times \delta(\omega + \omega_2 - \omega_3 - \omega_4)\mathcal{A}(k_2,\omega_2)\left[1 - f(\omega_2)\right]$$
$$\times \mathcal{A}(k_3,\omega_3)f(\omega_3)\mathcal{A}(k_4,\omega_4)f(\omega_4). \tag{2.77}$$

We note that we made use of Eq. (2.37) and Eq. (2.38) to express the correlation functions $G^{>}$ and $G^{<}$ in terms of the spectral function $\mathcal{A}$ and the Fermi distribution $f(\omega)$. We assume the matrix element $\mid \mathcal{M} \mid^2$ to be independent of energy and momentum, which corresponds to a contact interaction in coordinate space. In chapter 4, we dicuss the matrix element $\mid \mathcal{M} \mid^2$ in more detail. Taking the imaginary part of the retarded Green's function Eq. (2.74), we obtain the spectral function (see Eq. (2.36))

$$\mathcal{A}(k,\omega) = \frac{\Gamma(k,\omega)}{\left(\hbar\omega - \frac{\hbar^2 k^2}{2m} - \mathrm{Re}\Sigma^{(r)}(k,\omega)\right)^2 + \left(\frac{\Gamma(k,\omega)}{2}\right)^2}, \tag{2.78}$$

where we defined the width $\Gamma > 0$

$$\Gamma(k,\omega) = -2\mathrm{Im}\Sigma^{(r)}(k,\omega). \tag{2.79}$$

Since the real part of the self-energy plays an important role to fulfill analyticity, we calculate the real part from the imaginary part by using a dispersion relation

$$\mathrm{Re}\Sigma^{(r)}(k) = \Sigma_{MF}(k) + \mathcal{P}\int \frac{\mathrm{d}\omega'}{2\pi}\frac{\Gamma(k,\omega')}{\omega - \omega'}. \tag{2.80}$$

3 The Mean-Field

An appropriate way to include mean-field effects is using an energy density functional. A convenient and realistic approach is the Skyrme method, which parameterizes the interaction energy density in terms of contact terms plus a quadratic dependence on momenta. The simple structure of this kind of interaction allows one to write down the energy density in an algebraic form. From the energy density one can derive the mean-field properties of nucleons in the nuclear medium. Therefore, we discuss in this chapter how to obtain the mean-field properties needed for our calculations from the Skyrme energy density functional. After a short discussion of the Skyrme interaction and how to derive the energy density functional, we derive expressions for the effective mass and the effective potential in infinite nuclear matter. At the end our results are compared for different kind of parameter sets.

3.1 The Skyrme Interaction

The Skyrme approach uses 9 parameters to write down the nuclear force and provides a simple tool for calculating the properties of nucleons in the nuclear medium and in finite nuclei. Because of its simple analytic structure, one can express the Hamiltonian density for a system as a function of the nuclear and the kinetic density. A practical approach is obtained by approximating the ground state of the system by a single Slater determinant, i.e. using the mean-field underlying Hartree-Fock scheme. The parameterization allows one to fit the parameters to experimental results such as saturation density of infinite nuclear matter, binding energies single particle separation energies and rms-radii of some finite nuclei. This approach is very successful over the whole nuclear mass range.

In his original work [Sky59], Skyrme defined the nuclear force as a sum of two- and three-body forces

$$V = \sum_{i<j} v_{ij}^{(2)} + \sum_{i<j<k} \bar{v}_{ijk}^{(3)}. \tag{3.1}$$

For simplification we write down the two-body interaction part as a short-range expansion [VB72]

$$
\begin{aligned}
v_{ij}^{(2)}(r_1 - r_2) = {} & t_0(1 + x_0 P_\sigma)\delta(r_1 - r_2) \\
& + \frac{1}{2}t_1(1 + x_1 P_\sigma)\left[k'^2\delta(r_1 - r_2) + \delta(r_1 - r_2)k^2\right] \\
& + t_2(1 + x_2 P_\sigma)\vec{k'}\delta(r_1 - r_2)\vec{k} \\
& + iW_0\vec{\sigma}\cdot[\vec{k'}\times\delta(r_1 - r_2)\vec{k}].
\end{aligned}
\tag{3.2}
$$

Using the spin- and isospin-operator P_σ and P_τ, we antisymmetrize the interaction by

$$
\tilde{v}_{ij}^{(2)}(r_1 - r_2) = v_{ij}^{(2)}(r_1 - r_2)(1 - P_\sigma P_\tau).
\tag{3.3}
$$

The operator $\vec{k}$ is a relative wave vector

$$
\vec{k} = \frac{1}{2i}(\vec{\nabla}_1 - \vec{\nabla}_2)
\tag{3.4}
$$

acting to the right. The operator $\vec{k'}$ is the complex conjugate to the operator $\vec{k}$

$$
\vec{k'} = -\frac{1}{2i}(\overleftarrow{\nabla}_1 - \overleftarrow{\nabla}_2)
\tag{3.5}
$$

and acting to the left. Finally, the operators P_σ, P_τ and $\vec{\sigma}$ are given by the Pauli matrices

$$
P_\sigma = \frac{1}{2}(1 + \vec{\sigma}_1 \cdot \vec{\sigma}_2),
\tag{3.6}
$$

$$
P_\tau = \frac{1}{2}(1 + \vec{\tau}_1 \cdot \vec{\tau}_2),
\tag{3.7}
$$

$$
\vec{\sigma} = \vec{\sigma}_1 + \vec{\sigma}_2.
\tag{3.8}
$$

For the three-body force we also assume a zero range force

$$
\bar{v}_{ijk}^{(3)}(r_1, r_2, r_3) = t_3\delta(\vec{r}_1 - \vec{r}_2)\delta(\vec{r}_2 - \vec{r}_3).
\tag{3.9}
$$

It can be shown that for Hartree-Fock calculations Eq. (3.9) can be written as [VB72]

$$
v_{ij}^{(3)}(r_1, r_2) = \frac{1}{6}t_3(1 + x_3 P_\sigma)\rho_N^\alpha\left(\frac{r_1 + r_2}{2}\right)\delta(r_1 - r_2),
\tag{3.10}
$$

giving rise to an effective density-dependent two-body interaction. To derive the Hartree-Fock equations, we assume the ground to be given by a slater determinant of the single-particle wave functions ϕ_i:

$$
\phi(\vec{r}) = \frac{1}{\sqrt{A!}}\det|\phi_i^q(\vec{r}, s)|.
\tag{3.11}
$$

We note that the single particle wave functions are characterized by the orbital, the spin and isospin quantum numbers, i, s and q, respectively. The isospin quantum number is defined by the eigenvalues of $t_3 = \frac{1}{2}\sigma_3$, i.e. $q = +1/2$ for protons and $q = -1/2$ for neutrons. The expectation value of the energy is the given by relation

$$
\begin{aligned}
E &= \langle\phi|(T+V)|\phi\rangle \\
&= \sum_i \langle i|\frac{p^2}{2m}|i\rangle + \frac{1}{2}\sum_{ij}\langle ij|\tilde{v}_{12}|ij\rangle + \frac{1}{6}\sum_{ijk}\langle ijk|\tilde{v}_{123}|ijk\rangle \\
&= \int \mathcal{H}(\vec{r})\mathrm{d}^3r.
\end{aligned}
\tag{3.12}
$$

Here, $\mathcal{H}$ denotes the energy density

$$
\mathcal{H} = \mathcal{K} + \mathcal{H}_0 + \mathcal{H}_3 + \mathcal{H}_{eff} + \mathcal{H}_{fin} + \mathcal{H}_{SO} + \mathcal{H}_{SG} + \mathcal{H}_{Coul},
\tag{3.13}
$$

where $\mathcal{K}$ is the kinetic energy term, $\mathcal{H}_0$ a zero-range term, $\mathcal{H}_3$ the density-dependent three-body term, $\mathcal{H}_{eff}$ an effective mass term, $\mathcal{H}_{fin}$ a finite range term, $\mathcal{H}_{SO}$ a spin-orbit term, $\mathcal{H}_{SG}$ a term due to the tensor coupling with the spin gradient and $\mathcal{H}_{Coul}$ the Coulomb part calculated with the Slater approximation.

We introduce the local matter ρ_q, the local kinetic τ_q and local spin density $\vec{J}_q$,

$$
\rho(\vec{r}) = \sum_{i,s} |\phi_i^q(\vec{r},s)|^2 n_i^q,
\tag{3.14}
$$

$$
\tau(\vec{r}) = \sum_{i,s} |\vec{\nabla}\phi_i^q(\vec{r},s)|^2 n_i^q,
\tag{3.15}
$$

$$
\vec{J}_q(\vec{r}) = \sum_{i,s,s'} \phi_i^{q*}(\vec{r},s')\vec{\nabla}\phi_i^q(\vec{r},s) \times \langle s'|\vec{\sigma}|s\rangle\, n_i^q,
\tag{3.16}
$$

where n_i denotes the occupation number of the corresponding state i, s, q. After some algebra the energy density $\mathcal{H}$ can be expressed by local densities as:

$$
\begin{aligned}
\mathcal{H}_0 &= \frac{1}{4}t_0[(2+x_0)\rho^2 - (2x_0+1)(\rho_p^2 + \rho_n^2)] \\
\mathcal{H}_3 &= \frac{1}{24}t_3\rho^\sigma[(2+x_3)\rho^2 - (2x_3+1)(\rho_p^2 + \rho_n^2)]
\end{aligned}
$$

$$\mathcal{H}_{eff} = \frac{1}{8}[t_1(2+x_1) + t_2(2+x_2)]\tau\rho$$

$$+ \frac{1}{8}[t_2(2x_2+1) - t_1(2x_1+1)](\tau_p\rho_p + \tau_n\rho_n) \quad (3.17)$$

$$\mathcal{H}_{fin} = \frac{1}{32}[3t_1(2+x_1) - t_2(2+x_2)](\vec{\nabla}\rho)^2$$

$$- \frac{1}{32}[3t_1(2_x1+1) + t_2(2x_2+1)][(\vec{\nabla}\rho_p)^2 + (\vec{\nabla}\rho_n)^2]$$

$$\mathcal{H}_{SO} = \frac{1}{2}W_0[\vec{J}\cdot\vec{\nabla}\rho + \vec{J}_p\cdot\vec{\nabla}\rho_p + \vec{J}_n\cdot\vec{\nabla}\rho_n]$$

$$\mathcal{H}_{SG} = -\frac{1}{16}(t_1x_1 + t_2x_2)\vec{J}^2 + \frac{1}{16}(t_1-t_2)[\vec{J}_p^2 + \vec{J}_n^2]$$

Here, $\rho = \rho_p + \rho_n$, $\tau = \tau_p + \tau_n$ and $\vec{J} = \vec{J}_p + \vec{J}_n$ are the total matter, the total kinetic and the total spin densities, respectively. For a detailed calculation of the energy density functional Eq. (3.17), we refer to [VB72]. As we will see in the next steps, the energy functional is the basis to determine the mean-field quantities. To obtain the Hartree-Fock equations, the variation of the energy density functional has to be stationary with respect to the single particle states ϕ_i

$$\frac{\delta}{\delta\phi_i}\left(E - \sum_i e_i \int |\phi_i(\vec{r})|^2 \mathrm{d}^3r\right) = 0. \quad (3.18)$$

We note that the single particle states ϕ_i are assumed to be normalized. Using the definition for the variation of the energy density functional,

$$\delta E = E(\phi_i + \delta\phi_i) - E(\phi_i), \quad (3.19)$$

one yields, by using equation Eq. (3.17) and after integration by parts, for the binding-energy difference

$$\delta E = \sum_{q=p,n} \int \mathrm{d}^3r \left[\frac{\hbar^2}{2m_q^*(\vec{r})}\delta\tau_q(\vec{r}) + U_q^{eff}(\vec{r})\delta\rho_q(\vec{r}) + \vec{W}(\vec{r})\delta\vec{J}_q(\vec{r})\right]. \quad (3.20)$$

In Eq. (3.20) we introduced the effective mass m^* and the effective potential U_q^{eff}, which we will discuss later in detail. We assume our system to have time-reversal invariance, therefore, only such variations that obey $\delta\phi_i^q(\vec{r},s) = -2s\delta\phi_i^{q*}(\vec{r},-s)$ are allowed. For the variations of the local, kinetic and spin densities one then yields

$$\delta\rho_q(\vec{r}) = 2\sum_{i,s}\delta\phi_i^{q*}(\vec{r},s)\phi_i^q(\vec{r},s)n_i^q,$$

$$\delta\tau_q(\vec{r}) = 2\sum_{i,s}[\vec{\nabla}\delta\phi_i^{q*}(\vec{r},s)]\cdot\vec{\nabla}\phi_i^q(\vec{r},s)n_i^q, \quad (3.21)$$

$$\delta\vec{J}_q(\vec{r}) = -2i\sum_{i,s,s'}\delta\phi_i^{q*}(\vec{r},s')\vec{\nabla}\phi_i^q(\vec{r},s)\times\langle s'|\vec{\sigma}|s\rangle n_i^q.$$

Using these expressions with Eq. (3.20) and integrating the $\delta\tau_q$ terms by parts, we obtain

$$\delta E = 2\sum_{i,q}\int \mathrm{d}^3r\,\delta\phi_i^{q*}\left\{-\vec{\nabla}\cdot\frac{\hbar^2}{2m_q^*}\vec{\nabla}\phi_i^q + \left[U_q + \vec{W}_q\cdot(-i)(\nabla\times\vec{\sigma})\right]\phi_i^q\right\}. \qquad (3.22)$$

We note that here ϕ_i^q is a two-component spinor, which was introduced for simplicity reason. Since the total energy has to be stationary, each component in the sum of equation Eq. (3.22) has to vanish. Hence the single particle wave functions ϕ_i have to fulfill the Schrödinger like equation

$$\left[-\vec{\nabla}\frac{\hbar^2}{2m_q^*(\vec{r})}\vec{\nabla} + U_q^{eff}(\vec{r}) + \vec{W}(\vec{r})(-i)(\vec{\nabla}\times\vec{\sigma})\right]\phi_i^q(\vec{r},s) = e_i\phi_i^q(\vec{r},s). \qquad (3.23)$$

We note that the effective mass m_q^* and the effective potential U_q^{eff} are generated by the interaction of the particles.

3.2 The Parameter Set

The simple analytic structure of the Skyrme interaction allows us to determine its parameters so that the properties of nuclear matter and finite nuclei, such as binding energies and other experimental informations are reproduced. Since the fundamental work of Skyrme [Sky59] in the late fifties and Vautherin and Brink [VB72] in the early seventies, a lot of effort has been made to improve that kind of approach. One of the first realizations of the approach led to the so-called SIII Skyrme interaction [BFvGQ75], which was very successful throughout the entire mass table. Since that time a lot of other parameter sets have been constructed depending on which nuclear properties they should reproduce. From a better understanding of the nuclear matter incompressibility modulus, obtained by the experimental measurement of the giant iscoscalar monopole resonance, the SkM Skyrme parameterization [KTB80] was developed. Later information of the nuclear surface tension, which was obtained by detailed studies of fission barriers in the actinide region, was included and the SkM* parameterization [BQB+82] was developed. Reinhard and others modified the spin-orbit term in the SkM* parameterization to obtain a better agreement of the isotope shifts in the Pb region for relativistic and non-relativistic calculations and developed the SkI3 Skyrme parameterization [RF95]. Later, Tondeur et al. examined the influence of different parameters and developed a set of Skyrme parameterization [TBFP84]. The Skyrme Lyon series [CMB+97, CBH+98] contains not only information of nuclei along the line of stability, but also information of exotic nuclei from the proton to the neutron drip line. The most advanced of the parameterizations is the SLy10 force, which provides a good basis to study exotic

Model	SLy10	SkI3	SkM*
t_0	-2506.77	-1762.88	-2645.00
t_1	430.98	561.608	410.00
t_2	-304.95	-227.09	-135.00
t_3	13826.41	8106.2	15595.00
x_0	1.0398	0.3083	0.09
x_1	-0.6745	-1.1722	0.00
x_2	-1.0	-1.0907	0.00
x_3	1.6833	1.2926	0.00
σ	1/6	1/4	1/6
W_0	-	0.00	130.0
W_1	75.86	-	-
W_2	105.50	0.00	130.0

Table 3.1: Some Skyrme parameters for the NN interaction (t_0 is given in MeV fm^3, t_1,t_2 and W_0, W_1 and W_2 are given in MeV fm^5, t_3 is given Mev fm$^{3+3\sigma}$, all other parameters are dimensionless)

nuclear matter. In table 3.1 some Skyrme parameters which we will use later are listed. We note that the parameters W_0, W_1 and W_2 are given for completeness. For the definition of the parameters W_1 and W_2 we refer to [CBH$^+$98]. A detailed discussion of the properties of different Skyrme parameter sets can be found in [SR07].

3.3 Infinite Nuclear Matter

In the case of infinite nuclear matter, which is represented by a Fermi gas in a volume sufficiently large so that surface effects can be neglected, we consider $\vec{\nabla}\rho_q = \vec{\nabla} \cdot \vec{J}_q = 0$. Since the existence of stars, bound together by the gravitational force, which is many orders weaker than the electromagnetic force, we assume the Coulomb force to be absent. In a Fermi gas at zero temperature the relations for the density ρ_q and the kinetic energy density τ_q can immediately be written down for protons and neutrons as

$$\rho_q = \frac{1}{3\pi^2}k_{fq}^3, \tag{3.24}$$

$$\tau_q = \frac{3}{5}(3\pi^2)^{\frac{2}{3}}\rho_q^{\frac{5}{3}}, \tag{3.25}$$

where k_{fq} is the Fermi momentum for protons and neutrons, respectively. This allows us to express the energy per particle as

$$\frac{E}{A}(\rho) = \frac{V}{A}\mathcal{H}(\rho) = \frac{\mathcal{H}(\rho)}{\rho}. \tag{3.26}$$

Using Eq. (3.26) with the energy density functional Eq. (3.17) yields

$$\begin{aligned}
\frac{E}{A}(\rho, Y) = {} & \frac{3}{5}\frac{\hbar^2}{2m}\left(\frac{3\pi^2}{2}\right)^{\frac{2}{3}}F_{5/3} + \frac{1}{8}t_0\rho\left[2(x_0+2) - (2x_0+1)F_2\right] \\
& + \frac{1}{48}t_3\rho^{\sigma+1}\left[2(x_3+2) - (2x_3+1)F_2\right] \\
& + \frac{3}{40}\left(\frac{3\pi^2}{2}\right)^{\frac{2}{3}}\rho^{\frac{5}{3}}\left\{\left[t_1(x_1+2) + t_2(x_2+2)\right]F_{5/3}\right. \\
& \left. + \frac{1}{2}\left[t_2(2x_2+1) - t_1(2x_1+1)\right]F_{8/3}\right\},
\end{aligned} \tag{3.27}$$

where we defined the asymmetry factor $F_m(Y) = 2^{m-1}[Y^m + (1-Y)^m]$ and the asymmetry coefficient $Y = \frac{Z}{A}$. Fig. 3.1 shows the equation of state for different Skyrme parameterizations in the case of symmetric nuclear matter. All parameterizations reproduce the properties of nuclear matter and they agree very well up to a density of $\rho = 0.4$ fm^{-3}. Especially the saturation density $\rho = 0.16$ fm^{-3} and the binding energy at the saturation point $E_{sat} = -16$ MeV of nuclear matter are well reproduced by all the parameterizations. On the other hand, there is a variation in the high density region. Unfortunately, the high density behavior of the equation of state is still an open question. In the case of asymmetric nuclear matter the saturation point of all Skyrme parameterizations is shifted to lower densities. With increasing number of neutrons, nuclear matter is less bound until, as seen in Fig. 3.2 for the case $Y = 0.1$, very neutron rich nuclear matter is not bound anymore. In Fig. 3.2 neutron rich nuclear matter for the asymmetry coefficient $Y = 0.1$ is shown, while the SLy10 and SkM* parameterizations agree very well, provides the SkI3 parameterization a more stiff equation of state.

Fig. 3.3 shows a comparison of the equation of state for symmetric nuclear matter using different models. The full line shows the result which was received with the SLy10 Skyrme parameterization, the dashed line the results of the Urbana group [APR98], the dotted line the results for the density dependent relativistic hadron field model (DDRH) [Fed09] and the thin line results of a relativistic phenomenological model with density dependent coupling constants [NcvacVFR02]. All model agree in the low density region, while the relativistic density dependent models predict a more stiff equation of state. Especially the results of the SLy10 parameterization agrees very well with the results obtained by the Urbana group. The same behavior is see in the case of pure neutron matter Fig. 3.4. Here also a more
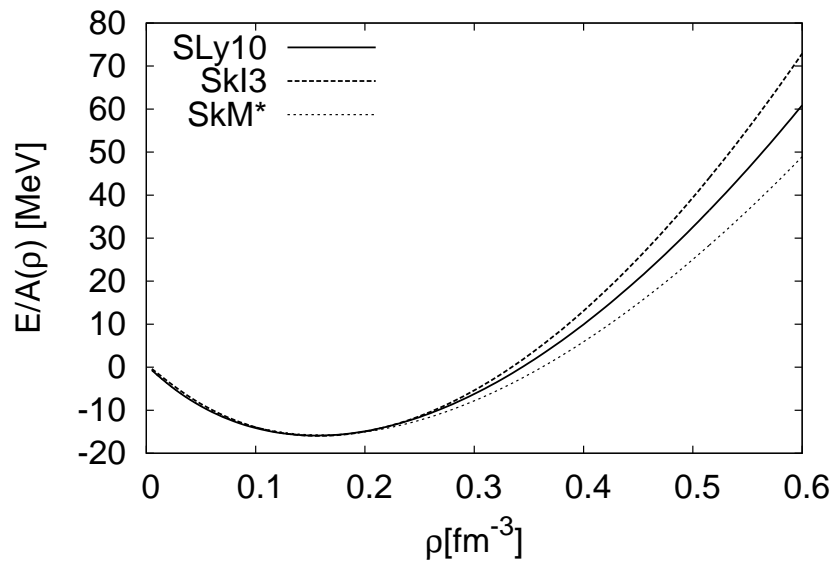
Figure 3.1: The equation of state in symmetric nuclear matter for the Skyrme parameter sets SLy10, SkI3 and SkM*.
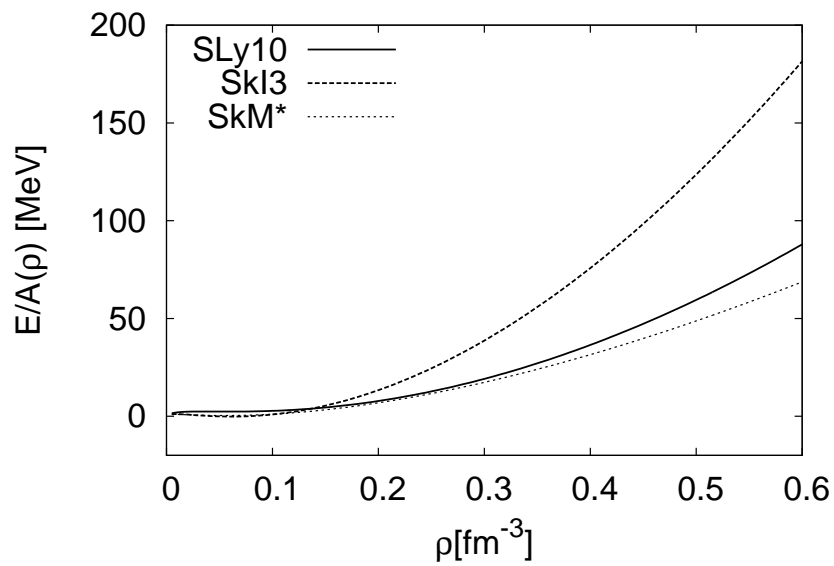
Figure 3.2: The equation of state in asymmetric nuclear matter with asymmetry coefficient $Y = 0.1$ for the Skyrme parameter sets SLy10, SkI3 and SkM*.
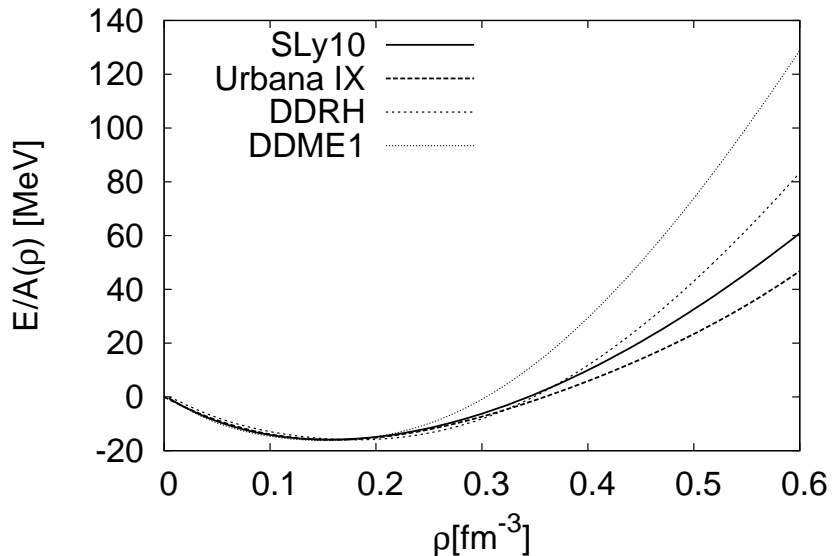
Figure 3.3: Comparison of the results for the equation of state of symmetric nuclear matter using different models. The results are compared for the SLy10 Skyrme parameterization, the Urbana IX model [APR98], the density dependent relativistic hadron field (DDRH) model [Fed09] and a relativistic phenomenological model with density dependent coupling constants (DDME1) [NcvacVFR02].

stiff equation of state is predicted by the density dependent relativistic models by a good agreement of the two non-relativistic models.

The pressure P of nuclear matter is given by the partial derivative of the energy according to the volume [CMB^{+}97] keeping the total number of particle A constant:

$$P = -\left.\frac{\partial E}{\partial V}\right|_A = \frac{A}{V^2}\left.\frac{\partial E}{\partial \rho}\right|_A = \rho^2 \left.\frac{\partial \frac{E}{A}(\rho)}{\partial \rho}\right|_A \tag{3.28}$$

We then can define the incompressibility modulus at non-zero pressure [CMB^{+}97]:

$$K = \frac{18P}{\rho} + 9\rho^2 \frac{\partial \frac{E}{A}}{\partial \rho^2}. \tag{3.29}$$

At the equilibrium density ρ_0 the pressure P vanishes and the incompressibility coefficient K_∞ is given by

$$K_\infty = 9\rho_0^2 \left.\frac{\partial \frac{E}{A}}{\partial \rho^2}\right|_{\rho=\rho_0}. \tag{3.30}$$
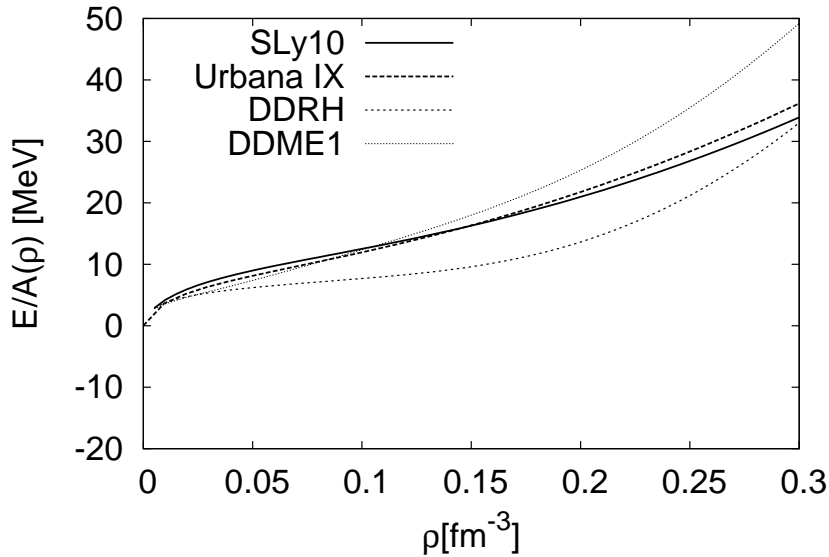
Figure 3.4: Comparison of the results for the equation of state of pure neutron matter using different models. The results are compared for the SLy10 Skyrme parameterization, the Urbana IX model, DDRH model and DDME1 model.

The incompressibility coefficient K_∞ is the second derivative of the equation of state and is therefore a measure of the stiffness of the equation of state, the higher K_∞ the stiffer is the equation of state. In Fig. 3.3 and Fig. 3.3 results for incompressibility coefficient K_∞ using different models are shown for symmetric nuclear and pure neutron matter. All models, except the relativistic phenomenological model with density dependent coupling constants [NcvacVFR02], predict the right phenomenological value of $K_\infty \approx 230$ MeV at saturation point density. The SLy10 Skyrme parameterization is in good agreement with the results obtained with the Urbana IX model for symmetric nuclear matter and for pure neutron matter, while the relativistic models predict a higher value of the incompressibility coefficient. This observation is in agreement with the observation of a stiffer equation of state in Fig. 3.1 and Fig. 3.4

We can also derive the symmetry energy coefficient [CMB[+]97] which occurs in the
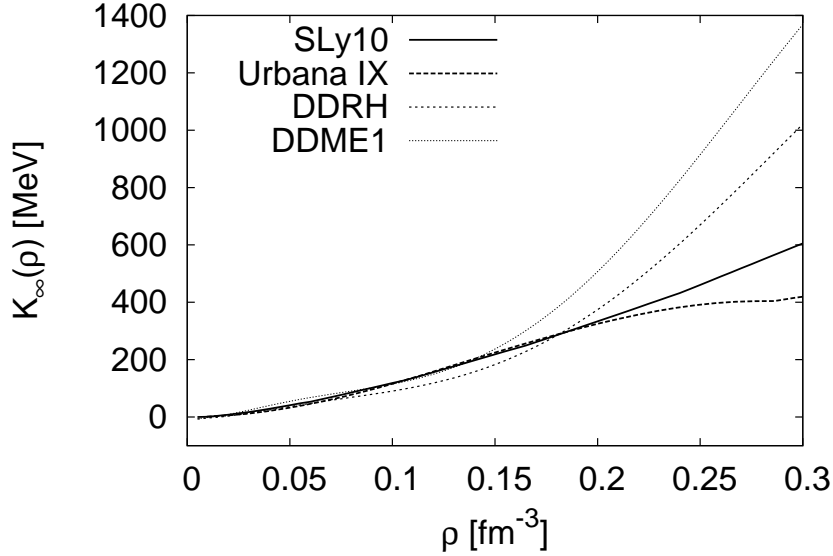
Figure 3.5: Comparison of the results for the incompressibility coefficient K_∞ of symmetric nuclear matter using different models. The results are compared for the SLy10 Skyrme parameterization, the Urbana IX model, DDRH model and DDME1 model.

expansion of the liquid drop model [Wei35] from Eq. (3.27):

$$
\begin{aligned}
a_s &= \frac{1}{2} \frac{\partial^2 \frac{E}{A}(\rho)}{\partial I^2}\Big|_{I=0} \\
&= \frac{1}{3} \frac{\hbar^2}{2m} \left(\frac{3\pi^2}{2} \right)^{\frac{2}{3}} \rho^{\frac{2}{3}} - t_0(2x_0 + 1)\rho \\
&\quad + \frac{1}{24} \left(\frac{3\pi^2}{2} \right)^{\frac{2}{3}} \Theta_{sym} \rho^{\frac{5}{3}} - \frac{1}{48} t_3(2x_3 + 1)\rho^{\sigma+1}.
\end{aligned}
\tag{3.31}
$$

Where I and Θ_{sym} are given by the expressions $I = (N - Z)/A$ and $\Theta_{sym} = 3t_1 x_1 - t_2(4 + 5x_2)$, respectively. The symmetry energy plays an important role of the understanding of many phenomena in nuclear physics and astrophysics. Results for the symmetry energy coefficient a_s are shown inFig. 3.7. So far no experimental information of the symmetry energy at high densities are available. The symmetry energy at normal matter density is usually tuned such that it reproduces the empirical value from the liquid drop model of about 30 MeV [LCK08]. As see in Fig. 3.7, all parameterizations reproduce the properties of the symmetry energy at the saturation point. In the high density region the three Skyrme parameterizations show a different behavior, the asymmetry energy grows for the SkI3, decreases for
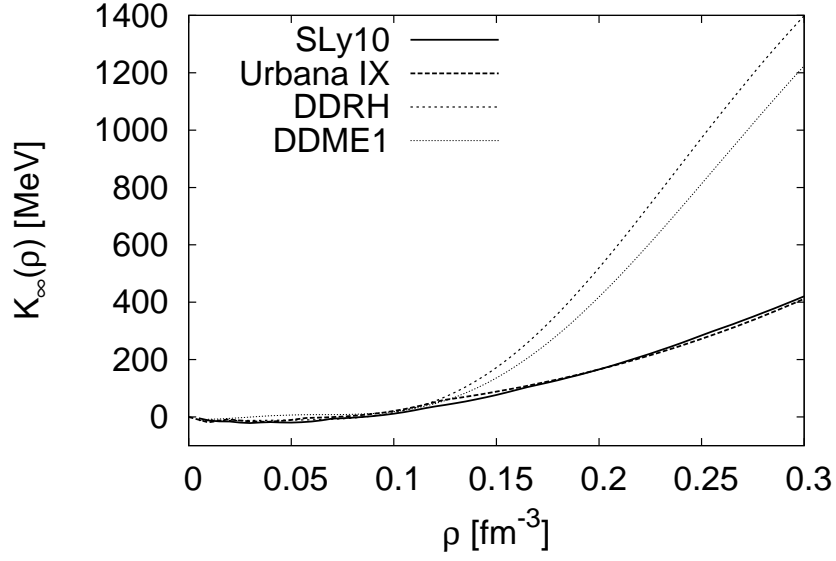
Figure 3.6: Comparison of the results for the incompressibility coefficient K_∞ of pure neutron matter using different models. The results are compared for the SLy10 Skyrme parameterization, the Urbana IX model, DDRH model and DDME1 model.
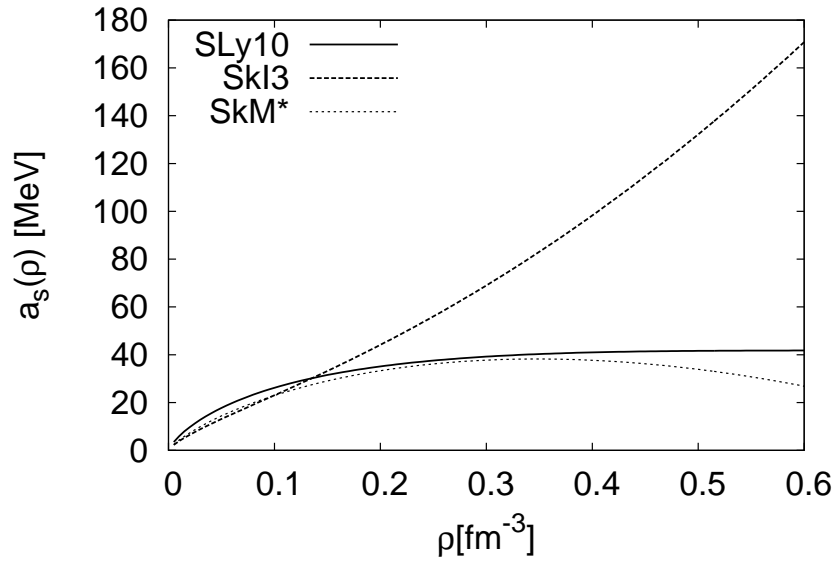
Figure 3.7: The density dependence of the symmetry energy coefficient for different sets of Skyrme parameterizations.

the SkM* and saturates for the SLy10 parameterization.

The single particle energy of a particle with momentum k in infinite nuclear matter is given by

$$\epsilon_q(k) = \hbar^2 \frac{k^2}{2m_q} + \Sigma_q^{MF}(k, \rho). \tag{3.32}$$

Absorbing the momentum-dependent part up to the second order in k into the kinetic energy term leads to an effective mass m_q^* and a momentum-independent effective potential U_q^{eff}

$$\epsilon_q(k) = \hbar^2 \frac{k^2}{2m_q^*(\rho)} + U_q^{eff}(\rho). \tag{3.33}$$

The effective mass can be obtained by collecting the $\rho\tau$-terms from the energy-density functional Eq. (3.17), the residual density dependent part can be related to the effective potential. For the effective mass in asymmetric nuclear matter we obtain

$$\frac{m_q}{m_q^*} = 1 + \frac{2m_N}{\hbar^2}(\frac{1}{8}[t_1(2 + x_1) + t_2(2 + x_2)]\rho \tag{3.34}$$

$$+ \frac{1}{8}[t_2(2x_2 + 1) - t_1(2x_1 + 1)]\rho_q).$$

The residual density dependent part, which we interpret as an effective potential, is then given by:

$$\begin{aligned}
U_q^{eff} = {} & \frac{1}{4}t_0[2(2 + x_0)\rho - 2(2x_0 + 1)\rho_q] \\
& + \frac{1}{24}t_3\rho^\alpha[2(2 + x_3)\rho - 2(2x_3 + 1)\rho_q] \\
& + \frac{1}{24}\alpha t_3\rho^{\alpha-1}[(2 + x_3)\rho^2 - (2x_3 + 1)(\rho_p^2 + \rho_n^2)] \\
& + \frac{1}{8}[t_1(2 + x1) + t_2(2 + x_2)]\tau \\
& + \frac{1}{8}[t_2(2x_2 + 1) - t_1(2x_1 + 1)]\tau_q.
\end{aligned} \tag{3.35}$$

In table 3.2 some properties of symmetric nuclear matter at the saturation point can be found for SLy10, SkM* and SkI3 Skyrme parameterizations.

Fig. 3.8 shows the effective mass in symmetric nuclear matter for the SLy10, SkI3 and SkM* Skyrme force . One clearly sees that the effective mass for all Skyrme forces drops with higher density. One interesting results of the effective masses is obtained when comparing the results for different Skyrme forces in asymmetric nuclear matter.

Model	SLy10	SkI3	SkM*
ρ_0 [fm^{-3}]	0.156	0.158	0.160
E/A [MeV]	-15.901	-15.96	-15.770
K_∞ [MeV]	-229.7	258.1	216.6
m^*/m	0.68	0.577	0.79
a_s [MeV]	31.98	34.8	30.03

Table 3.2: Properties of symmetric nuclear matter at saturation density for different Skyrme parameter sets. The values for SLy10 and SkM* parameter sets are taken from [CBH+98] and for SkI3 from [RF95].
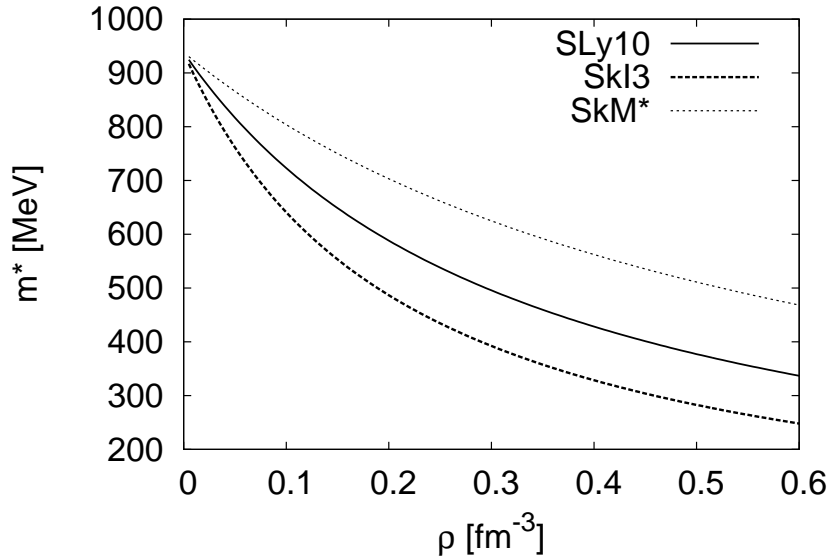
Figure 3.8: The effective mass for symmetric nuclear matter obtained with the Skyrme forces SLy230a, SkI3 and SkM*

Fig. 3.9 and Fig. 3.10 show results for the SLy10, SkM* and SkI3 Skyrme force in nuclear matter depending on the asymmetry coefficient, starting with pure neutron matter (Y=0). For the SkM* force one sees an increase of the neutron mass when going to very neutron rich systems, while the proton mass decreases. However the picture is different for the SLy10 and SkI3 force, here the proton mass increases and the neutron mass decreases for neutron rich systems. On the other hand side microscopic many-body theories, such as relativistic Dirac-Brückner-Hartree-Fock calculations, predict that $m_n^* > m_p^*$ [LCK08]. Unfortunately, so far almost nothing is known experimentally about the effective mass a the neutron-rich medium.
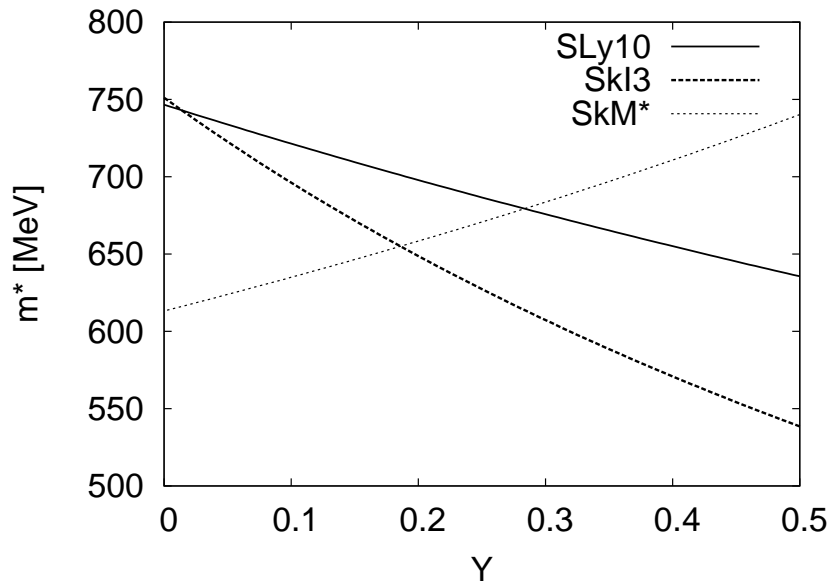
Figure 3.9: The proton effective mass at nuclear matter saturation density as a function of the asymmetry coefficient Y.
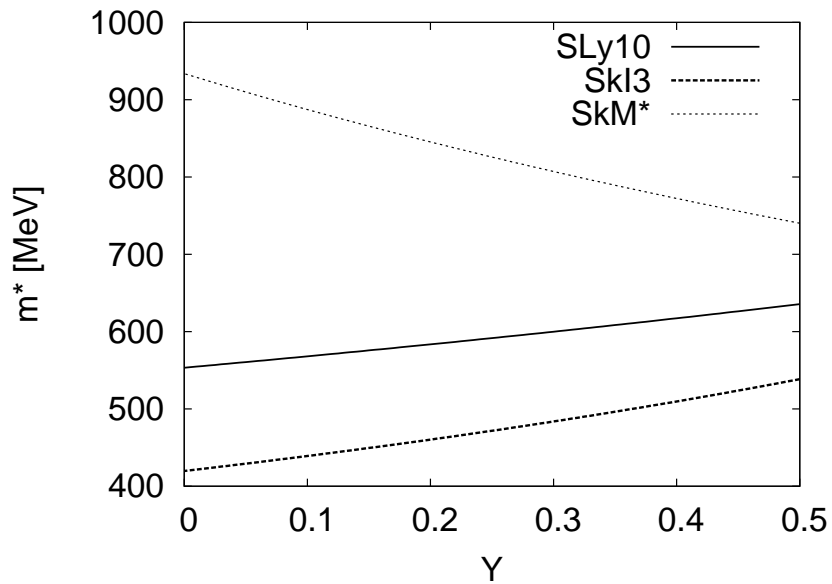
Figure 3.10: The neutron effective mass at nuclear matter saturation density as a function of the asymmetry coefficient Y.
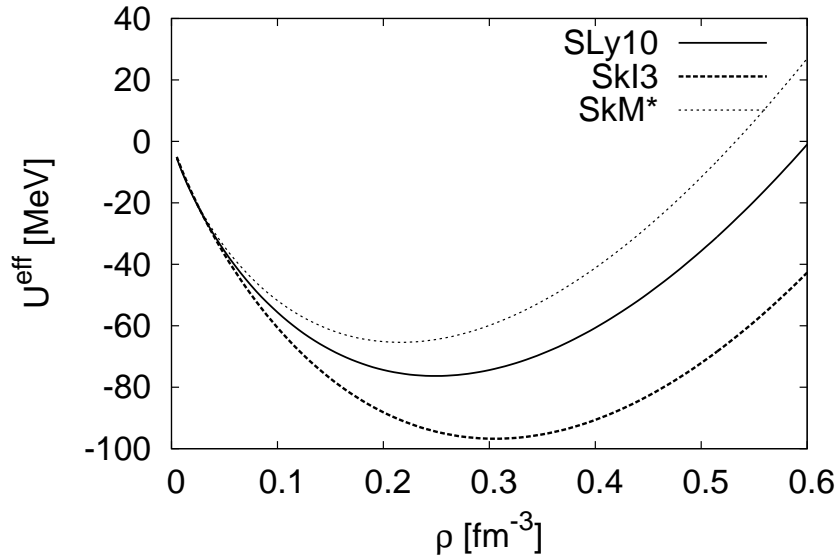
Figure 3.11: The effective potential for different sets of Skyrme parameters in symmetric nuclear matter depending on the density.

Results for the effective potential using different type of Skyrme parameterizations are found in Fig. 3.11, Fig. 3.12 and Fig. 3.13. In Fig. 3.11 results depending on the number density in symmetric nuclear matter are shown. Again, there is a good agreement on the qualitative level for all Skyrme parameterizations. The effective potentials for all here considered Skyrme parameterizations show a minimum which lies between $\rho =0.15$–0.3 fm^{-3}. For asymmetric nuclear matter also all parameterizations show the same behavior, as seen in Fig. 3.12 and Fig. 3.13 for protons and neutrons, respectively. Protons in neutron rich nuclear matter are stronger bound than neutrons.
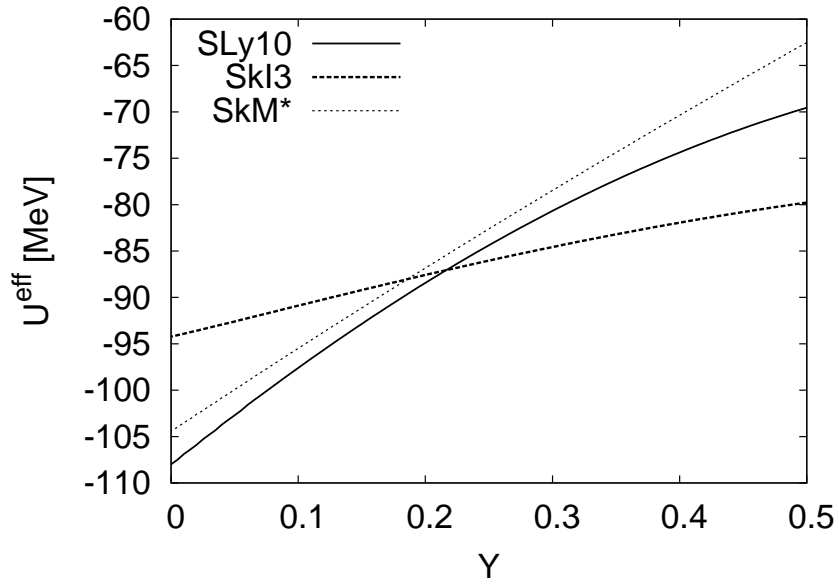
Figure 3.12: The proton effective potential at nuclear matter saturation as a function of the asymmetry coefficient Y.
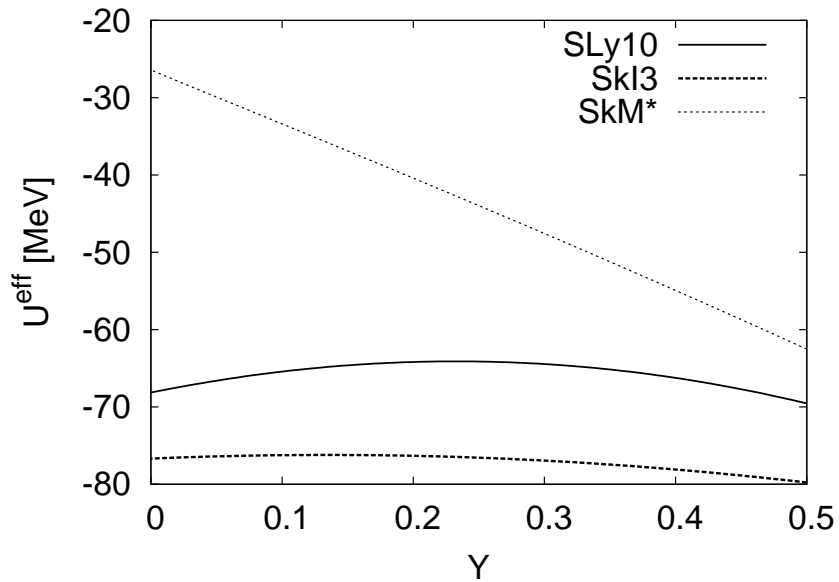
Figure 3.13: The neutron effective potential at nuclear matter saturation density as a function the asymmetry coefficient Y.

4 The Short-Range Interaction

In this chapter we determine the structure of the matrix elements $\mathcal{M}_{qq'}$ which we need for the calculation of the self-energies. An appropriate way to get information about the matrix elements is provided by Landau-Migdal theory. In the late fifties Landau developed his theory of Fermi liquids. He dealt with infinite systems such as liquid ^{3}He or nuclear matter. His theory is based on the idea that information on the interacting system can be obtained from the non-interacting one by an adiabatic switching of the interaction. He introduced the concept of quasi-particles, which correspond to particles in the non-interacting system. These quasi-particles in the correlated system behave like the particles in the non-interacting system and obey Fermi-Dirac statistics. Quasi-particles differ from real particles essentially by their mass. The interaction of quasi-particles, which in general depends on spin (in nuclear systems also on isospin) and momentum, can be expanded at the Fermi surface in terms of Legendre polynomials, the so called Landau-Migdal parameters. The Landau-Migdal parameters can be deduced from experiment. Landau used this approach to calculate the properties of excited Fermi liquids, such as the zero mode of liquid ^{3}He. In the late sixties Migdal applied Landaus's soundtheory to finite Fermi systems such as atomic nuclei [Mig75]. Here, one has to deal with two kinds of fermions, protons and neutrons, and a relative small number of particles. In atomic nuclei the quasi-particles correspond to single particle states of the nuclear shell model. The quasi-particle interaction is determined in the same way as in Landau's theory but is not only spin but also isospin dependent. In particular, the interaction is expanded in the same way at the Fermi surface in terms of Legendre polynomials and the parameters of the expansion, the Landau-Migdal parameters, are considered as universal quantities, characterizing the dynamical properties of a many-body system.

At the beginning of this chapter, we give a short introduction of the basic ideas of Landau-Midgal theory. For a more detailed introduction of the theory, see [Mig75, KST04, PN66, KST04]. Therafter, we determine the Landau-Migdal parameters from the Skyrme energy density functional and we discuss the results for different sets of parameters. We also dicuss the influence of the long range pion part. At the end we show results for the matrix element in nuclear and hypernuclear matter for different sets of Skyrme parameters.

4.1 The Landau-Migdal Interaction

The energy of an interacting system in the ground state can be expressed as a functional of the occupation probabilities $n_q(k)$ of the quasiparticle state $E_q = E_q(n(k))$. An Excitation of the system leads to a change $\delta n_q(k)$ of the occupation probability $n_q(k)$, where $q = p, n$ denotes the charge-flavor states of the baryons. This change in energy can be expressed as

$$\delta E = \sum_q \int \mathrm{d}^3 k \ \epsilon_q^0(k) \delta n_q(k) \tag{4.1}$$

$$+ \frac{1}{2} \sum_{qq'} \int \int \mathrm{d}^3 k \ \mathrm{d}^3 k' \ f^{qq'}(k, k') \delta n_q(k) \delta n_{q'}(k')$$

$$\sum_q \int \mathrm{d}^3 k \ \epsilon_q(k) \delta(k) = \sum_q \int \mathrm{d}^3 k \ [\epsilon_q^0(k) \delta n(k) \tag{4.2}$$

$$+ \frac{1}{2} \sum_{q'} \int \mathrm{d}^3 k' \ f^{qq'}(k, k') \delta n_q(k) \delta n_{q'}(k')],$$

where ϵ^0 is the energy of the non-interacting system in equilibrium. Eq. (4.2) shows that the single particle energy $\epsilon_q(k)$ and the quasiparticle interaction $f^{qq'}(k, k')$ can be obtained by first and second variation of the energy functional with respect to the occupation probability:

$$\epsilon_q(k) = \frac{\delta E}{\delta n_q(k)}, \quad f^{qq'}(k, k') = \frac{\delta^2 E}{\delta n_q(k) \delta n_{q'}(k')}. \tag{4.3}$$

In an isotropic system the quasi-particle interaction $f(k, k')$ only depends on the angle θ between the momenta k and k', thus the interaction can be expanded in terms of Legendre polynominal

$$f^{qq'}(k, k') = \sum_l f_l^{qq'} P_l(\cos \theta). \tag{4.4}$$

In nuclear matter the interaction can be related to observables such as the effective mass [Sjo76]

$$\frac{m_q^*}{m} = 1 + \frac{1}{3} F_1^q, \tag{4.5}$$

the isoscalar and isovector incompressibility [RD92]

$$K_s = \frac{9}{\rho} \sum_q \rho_q^2 (1 + F_0^q) / N_0^q, \tag{4.6}$$

$$K_v = \frac{9}{\rho_n - \rho_p} \left[\rho_n^2 (f_0^{nn} + \frac{1}{N_0^n}) - \rho_p^2 (f_0^{pp} + \frac{1}{N_0^p}) \right]. \tag{4.7}$$

The parameters F_0^q and F_1^q are given in terms of the interaction amplitudes at the Fermi-surface $f_l^{qq'} \equiv f_l^{qq'}(k_{F_q}, k_{F_{q'}})$ as

$$F_0^q = N_0^q \left[f_0^{qq} + \left(\frac{k_{F_{q'}}}{k_{F_q}} \right) f_0^{q'q} \right], \tag{4.8}$$

$$F_1^q = N_0^q \left[f_1^{qq} + \left(\frac{k_{F_{q'}}}{k_{F_q}} \right)^2 f_1^{q'q} \right], \tag{4.9}$$

here $q \neq q'$ (with $q, q' = p, n$), k_{F_q} is the Fermi-mommentum and N_0^q is the inverse density of state at the Fermi surface

$$N_0^q = \frac{m_q^* k_{F_q}}{\pi^2 \hbar^2}, \tag{4.10}$$

which takes the value $1/N \approx 300$ MeVfm^{-3} in symmetric nuclear matter. The dimensionless parameters F_l^q are called Landau-Migdal parameters and measure the strength of the interaction as compared to the kinetic energy.

4.2 Landau-Migdal Parameters from a Skyrme Interaction

As we saw in the previous section one can extract informations of the quasiparticle interaction from the energy density functional by doing the second variation with respect to the occupation numbers. The occupation probabilities are related to the particle density by

$$\rho = \frac{N}{V} = \frac{1}{V} \sum_k n(k), \tag{4.11}$$

where V is the volume and N the total number of particles in system. Therefore, the variation with respect to the occupation functions can be rewritten as:

$$\frac{\delta E}{\delta n(k)} = \frac{\delta E(\rho)}{\delta \rho} \tag{4.12}$$

For deriving the Landau parameters for a Skyrme interaction, we need the polarized energy functional $E(\rho_{p\uparrow}, \rho_{p\downarrow}, \rho_{n\uparrow}, \rho_{n\downarrow}, \rho_{\Lambda\uparrow}, \rho_{\Lambda\downarrow})$. The interaction amplitudes are given by the second variation with respect to the partial spin-flavor density

$$f^{qsq's'} = \frac{\delta^2 E}{\delta \rho_{qs} \delta \rho_{q's'}}, \tag{4.13}$$

where $q = p, n, \Lambda$. The interaction amplitudes in the spin singlet ($S = 0$) channel are obtained from

$$f^{qq'} = \frac{1}{4}[f^{q\uparrow q'\uparrow} + f^{q\downarrow q'\downarrow} + f^{q\uparrow q'\downarrow} + f^{q\downarrow q'\uparrow}] \qquad (4.14)$$

and the interaction amplitudes in the spin triplet ($S = 1$) channel are given by

$$g^{qq'} = \frac{1}{4}[f^{q\uparrow q'\uparrow} + f^{q\downarrow q'\downarrow} - f^{q\uparrow q'\downarrow} - f^{q\downarrow q'\uparrow}]. \qquad (4.15)$$

At this step we do not reproduce these somewhat lengthly calculations, the results can be found in an explicit form in Ref. [Mor05] and appendix B.

The interaction of the nucleons in nuclear matter then is given by

$$V^{qq'} = f^{qq'} + g'^{qq'}\vec{\sigma}_1\vec{\sigma}_2 \qquad (4.16)$$

For a Skyrme energy density functional only the $l = 0$ and $l = 1$ contributions are non vanishing. Anyhow, for our purpose only the $l = 0$ contributions play a role. A restriction to the lowest order $l = 0$ in Eq. (4.4) leads to a constant in momentum space, which corresponds to an δ-function in $\vec{r}$-space. The next order $l = 1$ is the derivative a δ-function, which leads to a momentum dependent contribution to the quasiparticle interaction. We note that most calculations are performed with the lowest order $l = 0$ contribution.

Fig. 4.1 and Fig. 4.2 show the Landau-Migdal parameters for nucleons in symmetric nuclear matter in the $S = 0$ and $S = 1$ channel using different Skyrme parameterizations. Since in case of symmetric nuclear $f_{pp} = f_{nn}$ and $g_{pp} = g_{nn}$, only the results for protons are shown. Except for the f_{pn} channel, the results show considerable variations. These variations reflecting the persisting uncertainties in the isospin and spin interaction. However, all parameters, except for g_{pn}, show similar properties at the qualitative level. For g_{pn} the SkM* parameterization predicts a constant value over the whole density region, while the SLy10 predicts a strong increase and the SkI3 an increase with saturation at high densities. This behavior is directly connected to the Skyrme parameters x_1, x_2 and x_3 (see chapter 3) , which are all zero for the SkM*. Entering the values in the explicit expression for g_{pn} in appendix B leads to a constant value.

4.3 Landau-Migdal Parameters for the Pion Contribution

The Landau-Migdal parameters obtained from the Skyrme energy density functional include short- and long-range interactions. However, the origin and nature of the
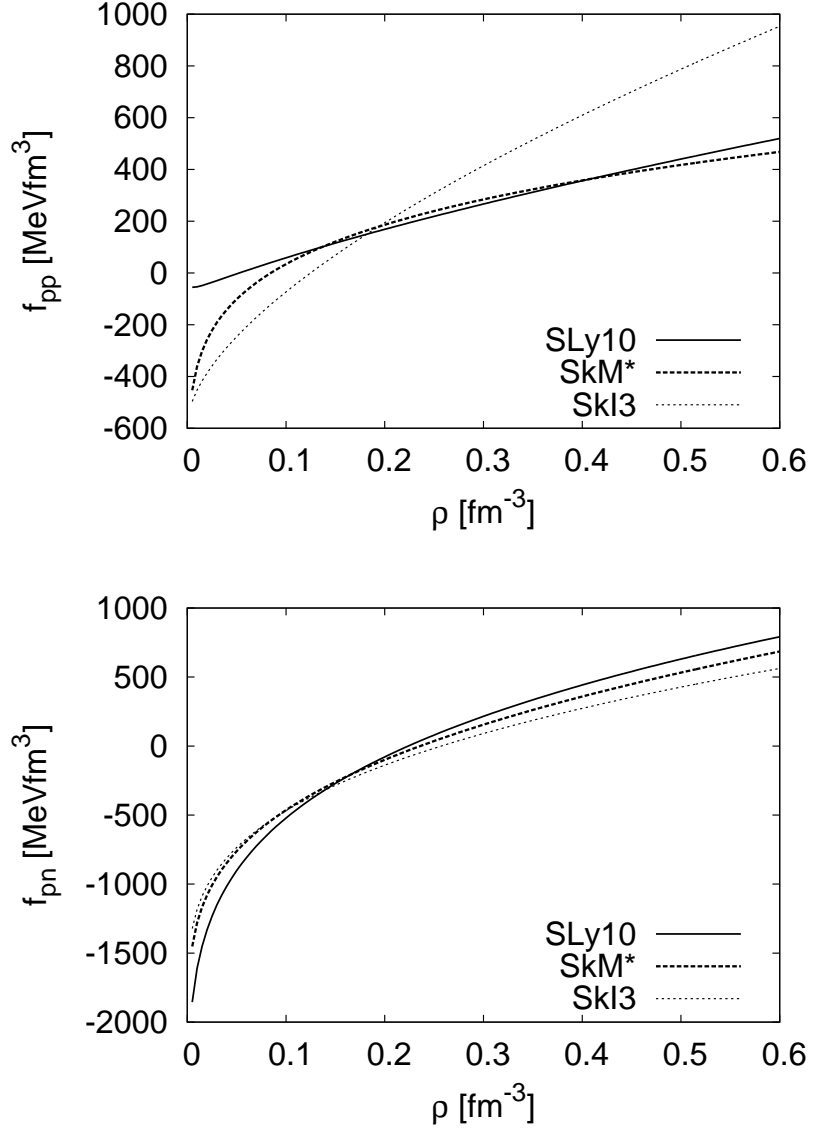
Figure 4.1: Landau-Migdal parameters in the singlet $(S = 0)$ channel obtained with the Skyrme parameterizations SLy10, SkM* and SkI3 in symmetric nuclear matter.
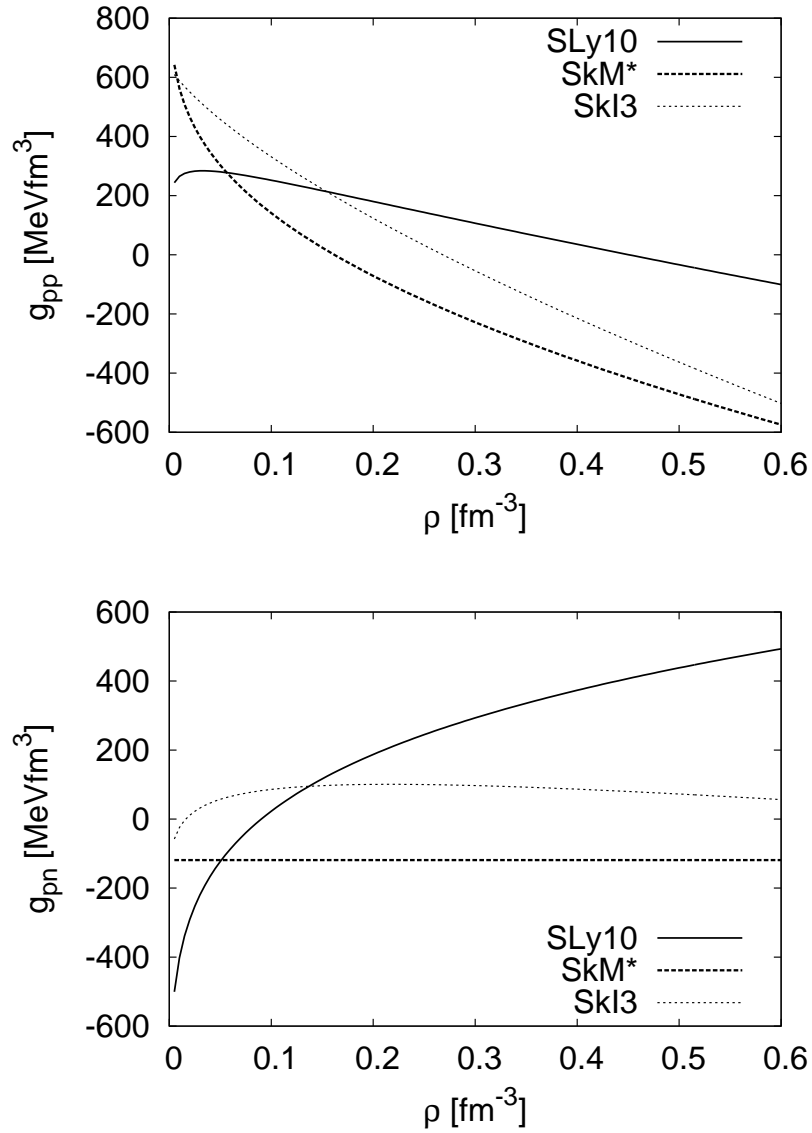
Figure 4.2: Landau-Migdal parameters in the triplet $(S = 1)$ channel obtained with the Skyrme parameterizations SLy10, SkM* and SkI3 in symmetric nuclear matter.

various pieces cannot be identified directly. Here we are interested mainly in the short-range parts. A simple but meaningful way to extract the short-range parts is to identify the long range components with the pion exchange. We define the short-range part of the interaction by subtracting the central part of the pion exchange NN interaction from the nucleon interaction, derived from the Skyrme energy density functional. We note that the Λ hyperons do not couple to the pions, so we do not subtract the pion contribution from the Λ interactions. We split the pion interaction into a central and a tensor interaction part

$$V_\pi(\vec{k}_1, \vec{k}_2) = -\frac{f_\pi^2}{m_\pi^2} D_\pi(\vec{k}_1, \vec{k}_2) \vec{\sigma}_1 \cdot \vec{k}_1 \vec{\sigma}_2 \cdot \vec{k}_2 \vec{\tau}_1 \cdot \vec{\tau}_2 \tag{4.17}$$

$$= V^C(\vec{k}_1, \vec{k}_2) + V^T(\vec{k}_1, \vec{k}_2) \tag{4.18}$$

where V_π^C is the central and V_π^T the tensor interaction part. Hence, we use the central interaction obtained from pion exchange and include anti-symmetrization explicitly by means of the spin and isospin exchange operators $P_{\sigma,\tau}$, respectively, thus leading to

$$V_\pi^C(\vec{k}_1, \vec{k}_2) = \frac{1}{3} f_\pi^2 D_\pi(\vec{k}_1, \vec{k}_2) \vec{\sigma}_1 \cdot \vec{\sigma}_2 \vec{\tau}_1 \cdot \vec{\tau}_2 (1 - P_\sigma P_\tau) \quad , \tag{4.19}$$

which can be arranged into

$$V_\pi^C(\vec{k}_1, \vec{k}_2) = \sum_{S,T=0,1} V_{ST}^{(\pi)}(\vec{k}_1, \vec{k}_2)(\vec{\sigma}_1 \cdot \vec{\sigma}_2)^S (\vec{\tau}_1 \cdot \vec{\tau}_2)^T. \tag{4.20}$$

Above, the momentum space pion propagator is denoted by

$$D_\pi(\vec{k}_1, \vec{k}_2) = \frac{1}{(p^2 + m^2)} F(p^2), \tag{4.21}$$

including a form factor which we choose to be of monopole shape with a cutoff $\Lambda = 800$ MeV/c. The 3-momentum transfer in the t-channel is $\vec{p} = \vec{k}_2 - \vec{k}_1$ while in the u-channel we have $\vec{p} = \vec{Q} = \vec{k}_2 + \vec{k}_1$. Numerically, we use $f_\pi \simeq 0.075$, which is the standard value for the pseudo-vector πNN coupling constant.

Hence, we cast the energy density functional into the form

$$E(\rho) = E_s(\rho) + E_\pi(\rho), \tag{4.22}$$

where $E_s \equiv E - E_\pi$ is the short-range contribution. The long range pionic part E_π is given by a sum over the various spin and isospin transfer contributions as defined in Eq. (4.20). Formally, E_π can be written as a sum over all spin-isospin channels

$$E_\pi(\rho) = \frac{1}{2} \sum_{qq'=p,n} \sum_{S,T=0,1} \int \frac{\mathrm{d}^3 k_1}{(2\pi)^3} \int \frac{\mathrm{d}^3 k_2}{(2\pi)^3} \Theta(k_{F_q} - k_1) \Theta(k_{F_{q'}} - k_2)$$

$$\times V_{ST}^{(\pi)}(\vec{k}_1, \vec{k}_2) \langle (\vec{\sigma}_1 \cdot \vec{\sigma}_2)^S (\vec{\tau}_1 \cdot \vec{\tau}_2)^T \rangle \tag{4.23}$$

although in spin-saturated nuclear matter only the $S = 0$ parts are non-vanishing. In symmetric nuclear matter the $T = 1$ components will not contribute. The brackets indicate traces over spin and expectation values on isospin and the step functions constrain the momentum integrals to the proton and neutron Fermi-spheres with Fermi-momenta k_{F_q} (with $q = p, n$), respectively. Second variation of the energy density in 4.23 with respect to particle densities leads to

$$
\frac{\partial^2 E_\pi(\rho)}{\partial \rho_q \partial \rho_{q'}} = \sum_{S,T=0,1} \sum_{q''} V_{ST}(k_{F_q}, k_{F_{q'}}) \langle (\vec{\sigma}_1 \cdot \vec{\sigma}_2)^S (\vec{\tau}_1 \cdot \vec{\tau}_2)^T \rangle \tag{4.24}
$$
$$
+ \quad \frac{1}{k_{F_{q'}}^2} \int \mathrm{d}k k^2 \Theta(k_{F_{q''}} - k) \frac{\partial}{\partial q}\bigg|_{k_{F_{q'}}} V_{ST} \langle (\vec{\sigma}_1 \cdot \vec{\sigma}_2)^S (\vec{\tau}_1 \cdot \vec{\tau}_2)^T \rangle .
$$

We can now identify the Landau-Migdal parameters:

$$
f^{(\pi)} = N_0^q V_{00} + f^{(r)}(k_{F_q}), \tag{4.25}
$$
$$
f'^{(\pi)} = N_0^q V_{10}, \tag{4.26}
$$
$$
g^{(\pi)} = N_0^q V_{01}, \tag{4.27}
$$
$$
g'^{(\pi)} = N_0^q V_{11}, \tag{4.28}
$$

where $f^r(k_{F_q})$ is an rearrangement term which appears for spin-saturated symmetric nuclear matter only in the $S = 0$, $T = 0$ channel.

Expanding the Landau-Migdal parameters in a Legendere series, which is common, leads to

$$
f_l^{(\pi)} = \int_{-1}^{1} \frac{2l + 1}{2} P_l(\cos\theta) f^{(\pi)}(\cos\theta) \mathrm{d}\cos\theta. \tag{4.29}
$$

The integration over the angle θ involves the Newman formula

$$
Q_l(t) = \frac{1}{2} \int_{-1}^{1} \frac{P_l(x)}{t - x} \mathrm{d}x, \tag{4.30}
$$

where the $Q_l(t)$ are Legendre functions of the 2nd kind [AS72]. The lowest order functions are given by

$$
Q_0(z) = \frac{1}{2} \ln\left(\frac{1+z}{1-z}\right), \tag{4.31}
$$
$$
Q_1(z) = \frac{z}{2} \ln\left(\frac{1+z}{1-z}\right) - 1,
$$

and those of higher order $l \geq 2$ can be obtained recursively [AS72].

Using equation (4.30) together with our expressions Eq. (4.25)–Eq. (4.28) for the Landau-Midgal parameters leads to

$$f_l^{(\pi)}(k_{F_q}) = -4\pi \frac{9}{4} N_0^q \frac{f_\pi^2}{2k_{F_q}^2} Q_l (1 + \frac{m_\pi^2}{2k_{F_q}^2}) + f_l^{(r)}(k_F), \tag{4.32}$$

$$f_l'^{(\pi)}(k_{F_q}) = 4\pi \frac{3}{4} N_0^q \frac{f_\pi^2}{2k_{F_q}^2} Q_l (1 + \frac{m_\pi^2}{2k_{F_q}^2}), \tag{4.33}$$

$$g_l^{(\pi)}(k_{F_q}) = 4\pi \frac{3}{4} N_0^q \frac{f_\pi^2}{2k_{F_q}^2} Q_l (1 + \frac{m_\pi^2}{2k_{F_q}^2}), \tag{4.34}$$

$$g_l'^{(\pi)}(k_{F_q}) = -4\pi \frac{1}{4} N_0^q \frac{f_\pi^2}{2k_{F_q}^2} Q_l (1 + \frac{m_\pi^2}{2k_{F_q}^2}) + \delta_{l0} 4\pi N_0^q f_\pi^2 \frac{1}{m_\pi^2}. \tag{4.35}$$

Note that there is an additional term for $l = 0$ in the $T = 1$, $S = 1$ channel which enters due to the central interaction term. For the additional rearrangement term in Eq. (4.25) we get

$$f^{(r)}(k_{F_q}) = N_0^q \frac{1}{k_{F_q}^2} \int \mathrm{d}k k^2 \Theta(k_{F_q} - k) \frac{\partial}{\partial q}\Big|_{k_{F_q}} V_0^{(\pi)}(q, k), \tag{4.36}$$

where $V_0^\pi(q, k)$ is the monopole component of the $S = 0$, $T = 0$ u-channel pion exchange interaction. To subtract the pion contribution from the nucleon interaction obtained from the Skyrme density functional, we define the Landau-Migdal parameters in the particle channel as

$$f_\pi^{qq'}(k_{F_q}) = \frac{1}{2N_0^q} \left(f_l^{(\pi)}(k_{F_q})(-)^T f_l'^{(\pi)}(k_{F_q}) \right) \tag{4.37}$$

$$g_\pi^{qq'}(k_{F_q}) = \frac{1}{2N_0^q} \left(g_l^{(\pi)}(k_{F_q})(-)^T g_l'^{(\pi)}(k_{F_q}) \right), \tag{4.38}$$

where $T = 0$ and $T = 1$ for $q = q'$ and $q \neq q'$, respectively. Finally, the short range interactions are given by the relations

$$f_s^{qq'} = f^{qq'} - f_\pi^{qq'}, \tag{4.39}$$

$$g_s^{qq'} = g^{qq'} - g_\pi^{qq'}, \tag{4.40}$$

$$\tag{4.41}$$

for the NN interaction.

In Fig. 4.3 and Fig. 4.4 the results for the Landau-Migdal parameters with and without subtraction of short-range part are shown. The results are obtained using the SLy10 Skyrme parameterization. While the subtraction leads to more attraction for g_{pp}, it leads to more repulsion in the other channels.
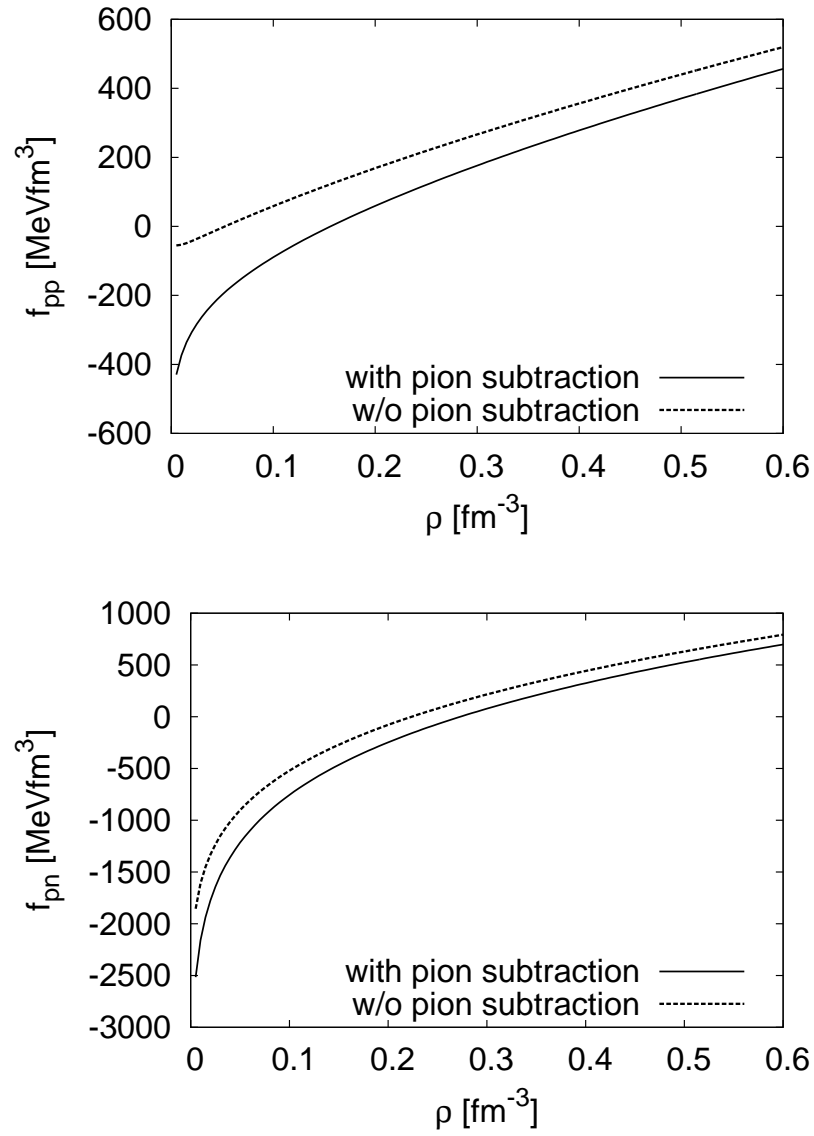
Figure 4.3: Landau-Migdal parameters with and without pion subtraction in the $S = 0$ channel obtained with the Skyrme parameterization SLy10.
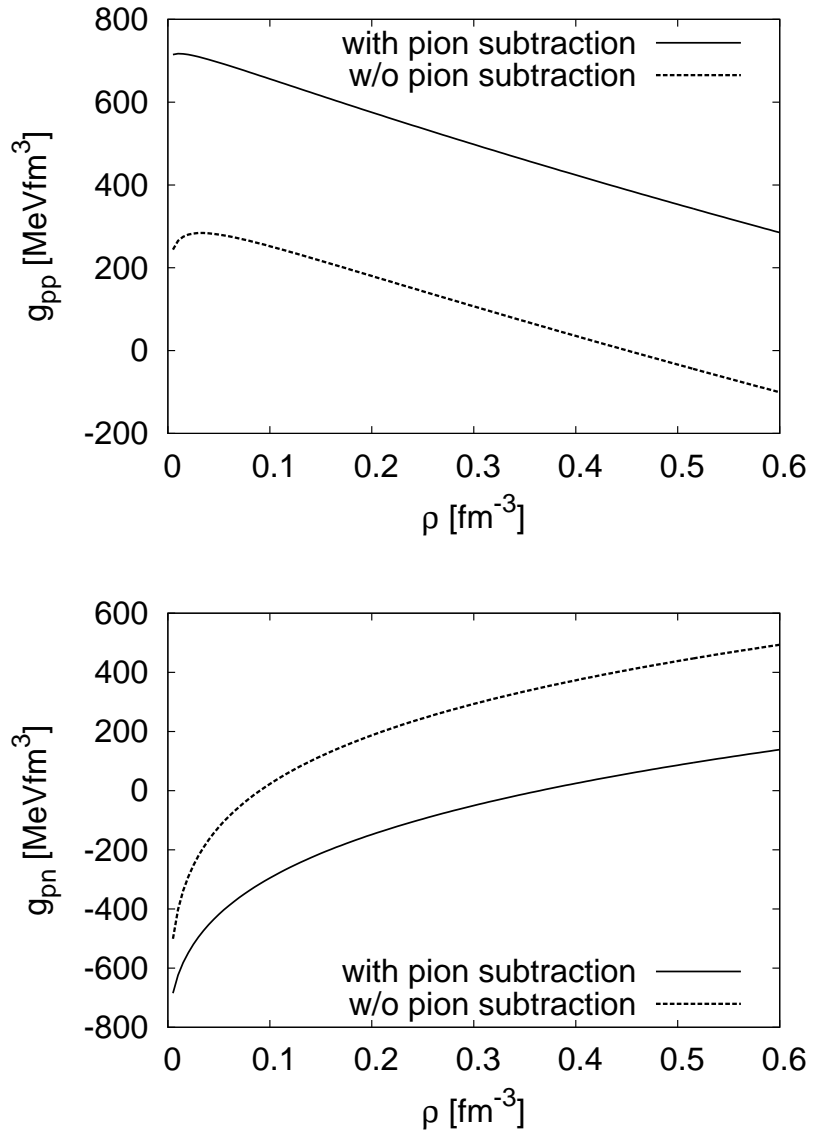
Figure 4.4: Landau-Migdal parameters with and without pion subtraction in the $S = 1$ channel obtained with the Skyrme parameterization SLy10.

4.4 The Matrix Element

As shown by Lehr et al. [LLLM02, LEL$^+$00] correlation in nuclear matter are dominated by phase space effects rather than by the off-shell momentum structure of the interactions. Lehr treated the interaction matrix element for nuclear matter $\mathcal{M}$ as a universal constant and adjusted it to the spectral function from Benhar et al. [BFF89]. The so obtained results for the nucleon width, spectral function and occupation number were in good agreement with other results using full many-body calculations, such as [BFF89] and [CdAS96]. In [KLM05] we applied the approach from Lehr to asymmetric nuclear matter. Comparing our results to the Tübingen group [HM04] we found that the universal character of short-range correlations holds also for asymmetric nuclear matter. In particular, we were able to describe the strong depletion of protons in neutron rich matter without using the tensor force explicitly. Thus, for including short-range effects the detailed modeling does not matter, but the overall strength of the interaction and a reliable description of the collisional phase space. Therefore, we will use the Landau-Migdal parameters, which match with an point-like interaction on the Fermi surface, to get information about the interaction matrix element. To obtain an average interaction matrix element, we sum over the weighted spin degrees of freedom

$$\mathcal{M}_{qq'} = \frac{1}{2}\sqrt{(f_{qq'}^s)^2 + 3(g_{qq'}^s)^2}. \tag{4.42}$$

We note that because of isospin symmetry, the matrix elements must fulfill the relation $\mathcal{M}_{pn} = \mathcal{M}_{np}$ in symmetric nuclear, while the in the general case of asymmetric nuclear matter we have $\mathcal{M}_{pp} \neq \mathcal{M}_{nn}$. In Fig. 4.5 the interaction matrix element for symmetric nuclear matter is shown. The upper figure shows the results for the isospin $T = 1$ channel and the lower picture for the isospin $T = 0$ channel. The interaction matrix element obtained from the SkM* and the SkI3 Skyrme energy functional show a similar behavior on a quantitative level. The matrix element $\mathcal{M}_{pp}$ starts at a strength of about 1000 MeVfm^3 and has a minimum at around twice nuclear matter saturation density, while the results obtained from the SLy10 Skyrme energy density functional shows a more stiff behavior. The picture changes for the interaction matrix $\mathcal{M}_{pn}$ in the isospin $T = 0$ channel. Here the matrix elements obtained from the SkM* and the SkI3 Skyrme energy functional show a more stiff behavior the the matrix element obtained with the SLy10 parameterization. The matrix elements start at around 1200 MeVfm^3 and have their minima at around 1.5 times nuclear matter saturation density. The overall behavior of all curves, starting with an high value reaching a minimum and rising again, can be explained by an interplay between the increase of the number of available states and the Pauli principle. At one hand, with rising density more states are blocked, at the other hand more interactions are possible. This leads to the very high value at very low

densities. We identify the long range part with pion contribution to the interaction, Fig. 4.5 shows the pion subtracted interaction matrix element. The influence of the pion subtraction is shown in Fig. 4.6. The results are obtained using the SLy10 Skyrme parameterization. For the isospin $T = 1$ channel, the subtraction of the pion contribution leads to an increase of the interaction matrix element in the region up to 1.5 times the nuclear matter saturation density. The minimum is shifted to higher densities. In the higher density region, the subtraction leads to a decrease of the interaction matrix element. The picture is different in the isospin $T = 0$ channel, here the subtraction leads to an increase of the interaction over the full range of density. The overall slope and the increasing strength can be understood in a microscopic picture. With increasing number of particles more states are blocked, therefore, is the matrix element higher for lower densities. The increase of strength when subtracting the long range part can be understood when having a closer look at the interaction potential of the nucleons. While the strong short range potential is repulsive, the long range part of the interaction is attractive. Therefore, both contributions average out in the density functional. Subtracting the long range contribution leads to the stronger repulsive short range interaction.

Fig. 4.7 shows the influence of asymmetry on the matrix element, starting with pure neutron matter and ending with symmetric nuclear matter. The results are taken at nuclear matter saturation density $\rho = 0.16$ fm^{-3}. From top to bottom the results are obtained using the SLy10, SkM* and SkI3 Skyrme energy density functional respectively. All investigated Skyrme parameterizations show the behavior on a qualitative level. Isospin symmetry demands that the pp interaction $\mathcal{M}_{pp}$ in symmetric nuclear matter is equal to the nn interaction $\mathcal{M}_{nn}$. Going to asymmetric nuclear matter this is no longer the case. With increasing number of neutrons, the interaction strength of the pp collision $\mathcal{M}_{pp}$ starts to rise, while the interaction strength of the nn interaction $\mathcal{M}_{nn}$ decreases. The interaction between neutrons and protons $\mathcal{M}_{pn}$ stays on a nearly constant value. However, there are differences between the Skyrme parameterizations on the quantitative level. We note that we can not make any predictions on the influence of the tensor force like in [HM04], since the tensor force is not included explicitly, but rather in a phenomenological way by the fits to nuclear properties.
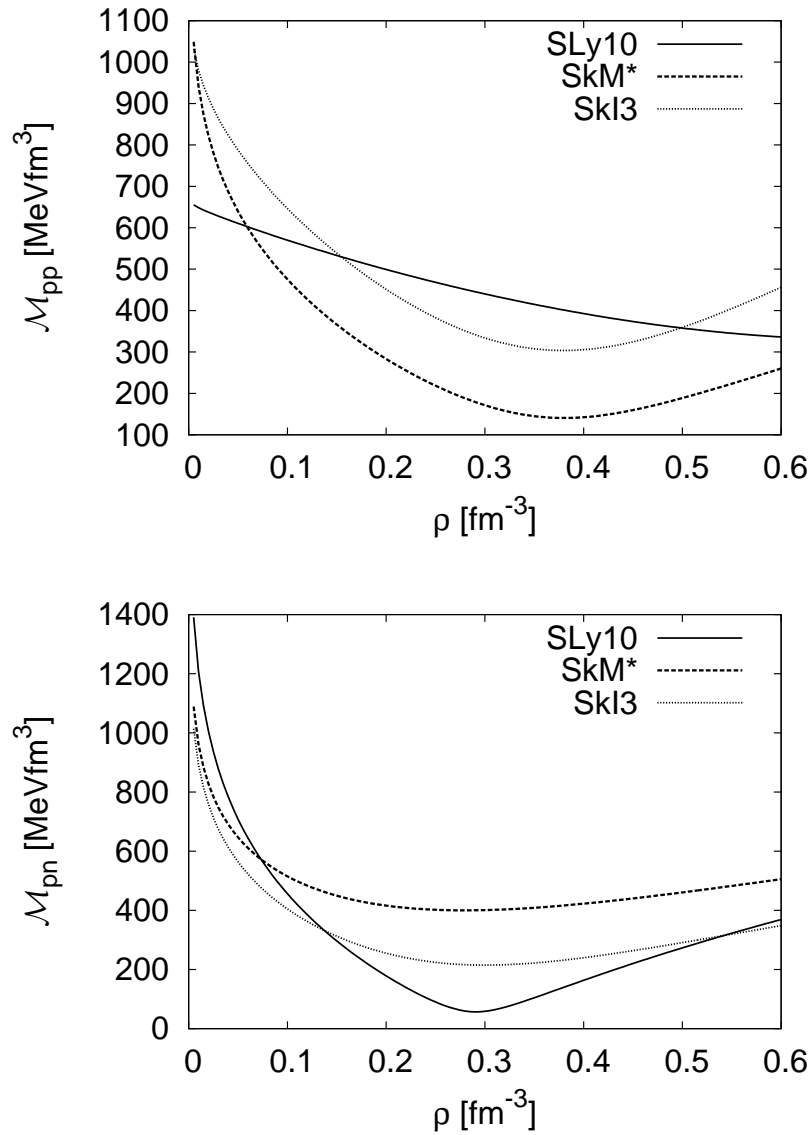
Figure 4.5: The pion subtracted interaction matrix elements in symmetric nuclear matter. The upper panel shows $\mathcal{M}_{pp}$ and the lower $\mathcal{M}_{pn}$. We note that in case of symmetric nuclear matter $\mathcal{M}_{pp} = \mathcal{M}_{nn}$.
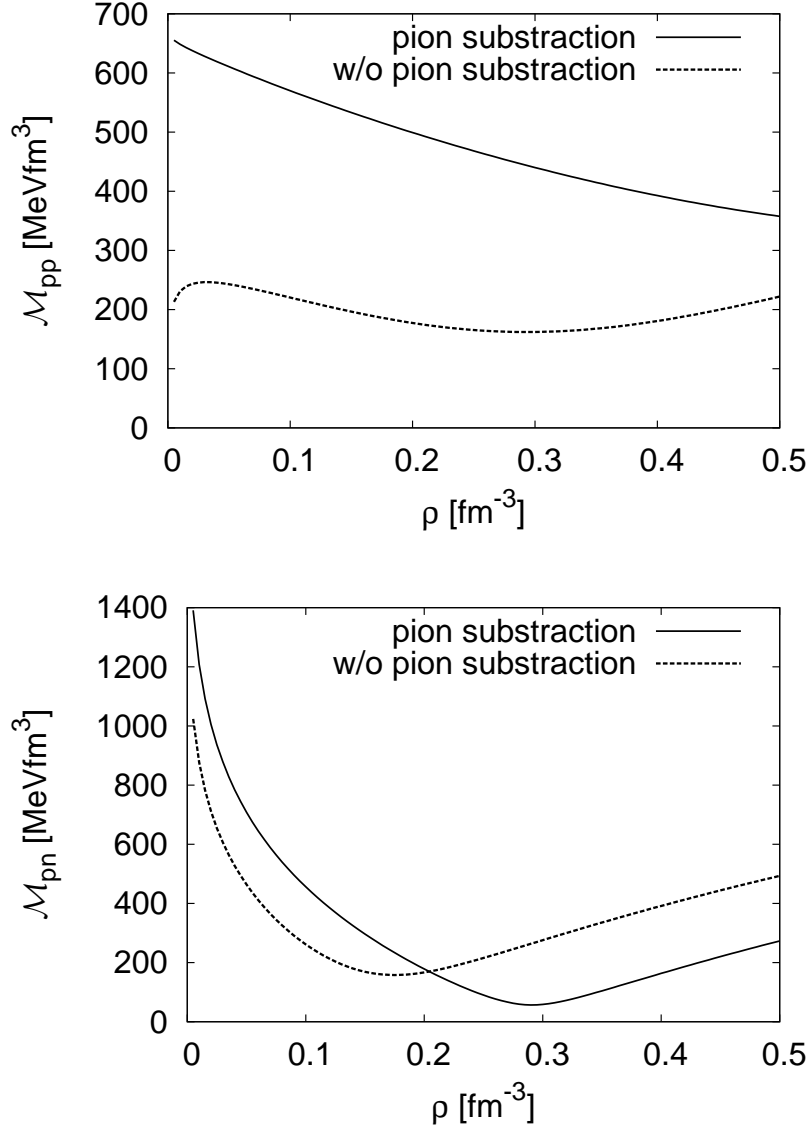
Figure 4.6: The influence of the subtraction of the pion contribution to the inter-
action matrix elements for the isospin $T = 1$ (upper panel) and the
isospin $T = 0$ (lower panel) channel. The results are obtained with the
SLy10 parameterization for the energy density functional.
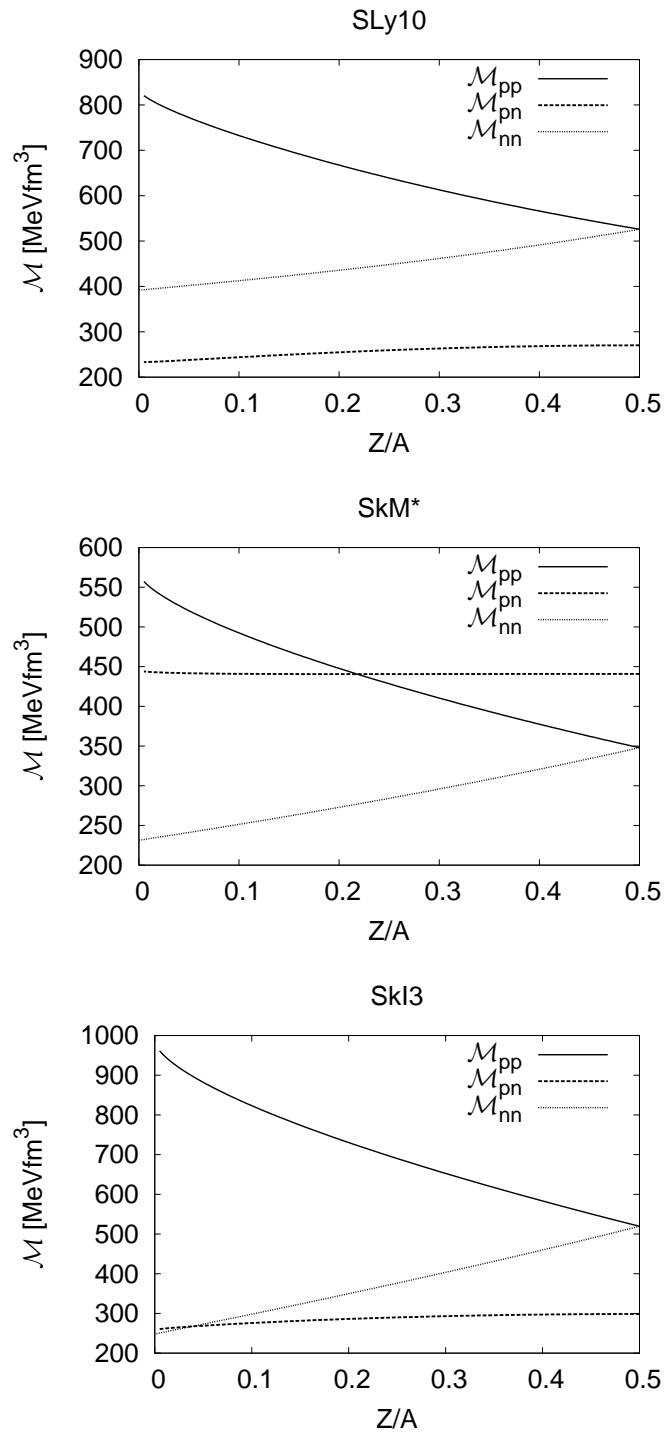
Figure 4.7: The influence of asymmetry to the interaction matrix element. The panel at the top shows results for the SLy10, the panel in the middle shows results for the SkM* and the panel at the bottom shows the results for the SkI3 Skyrme energy density functional, respectively.

5 Dynamical Correlations in Nuclear Matter

We now use the previous results and apply it to nuclear matter. At the beginning, we discuss the calculational details of our approach. After that, we examine the Skyrme parameterization influences the imaginary part of the self-energy and compare the results for neutron rich matter to the results of a recent Brueckner-Hartree-Fock (BHF) calculation from the Tübingen group [HM04]. Before we present results for the spectral function, we show how we calculated the real part of the self-energy. At the end, we introduce the momentum distribution and the spectroscopic factor. The influence of the pion contribution to the momentum distribution is shown and the results are compared to the results of Benhar et al. [BF00]. Finally, we compare the results for the spectroscopic factor to the results of [Leh03] and [BFF92].

5.1 Calculational Details

In the numerical calculations we use an iterative approach. Starting with an initial value for the width Γ, we calculate the spectral function $\mathcal{A}(k, \omega)$ using Eq. (2.78), thereby updating the imaginary part, i.e. the width Γ, and obtaining the dispersive real part leading to an energy shift. Afterwards, we use this result for the spectral function to calculate the self-energies using Eq. (2.76) and Eq. (2.77). We stop this procedure, if the changes in the obtained results are less than a lower limit ϵ, chosen typically as $\epsilon = 10^{-4}$. The chosen accuracy is typically achieved after 5 or 6iterations. In the language of Feynman diagrams this approach corresponds to the summation of the self-energies Eq. (2.77) and Eq. (2.76) to all orders.

In principle we saw in chapter 2.7 how to calculate the spectral function for a one component infinite system. Since we are interested in asymmetric nuclear matter, we have to modify Eq. (2.77) and Eq. (2.76) to incorporate the new degrees of freedom. The two-particle-one-hole (2p1h) and the one-particle-one-hole (1p2h) self-energies for a more component nuclear system are given by a summation of the additional

degrees of freedom

$$\Sigma_q^>(k,\omega) = -i\frac{2\hbar^2}{(2\pi)^8}\sum_{q'}\left\{\mid\mathcal{M}_{qq'}\mid^2\int \mathrm{d}^3k_2\mathrm{d}\omega_2\int \mathrm{d}^3k_3\mathrm{d}\omega_3\int \mathrm{d}^3k_4\mathrm{d}\omega_4\right.$$
$$\times\,\delta^3(k+k_2-k_3-k_4)\delta(\omega+\omega_2-\omega_3-\omega_4)\mathcal{A}_{q'}(k_2,\omega_2)f_{q'}(\omega_2)$$
$$\left.\times\,\mathcal{A}_{q'}(k_3,\omega_3)\left[1-f_{q'}(\omega_3)\right]\mathcal{A}_q(k_4,\omega_4)\left[1-f_q(\omega_4)\right]\right\}, \qquad (5.1)$$

$$\Sigma_q^<(k,\omega) = i\frac{2\hbar^2}{(2\pi)^8}\sum_{q'}\left\{\mid\mathcal{M}_{qq'}\mid^2\int \mathrm{d}^3k_2\mathrm{d}\omega_2\int \mathrm{d}^3k_3\mathrm{d}\omega_3\int \mathrm{d}^3k_4\mathrm{d}\omega_4\right.$$
$$\times\,\delta^3(k+k_2-k_3-k_4)\delta(\omega+\omega_2-\omega_3-\omega_4)\mathcal{A}_{q'}(k_2,\omega_2)\left[1-f_{q'}(\omega_2)\right]$$
$$\left.\times\,\mathcal{A}_{q'}(k_3,\omega_3)f_{q'}(\omega_3)\mathcal{A}_q(k_4,\omega_4)f_q(\omega_4).\right\}. \qquad (5.2)$$

Therefore, we have to sum over protons and neutrons in the case of asymmetric nuclear matter.

With the help of the delta-functions in Eq. (5.1) and Eq. (5.2) we can carry out the six integrations over ω_4, $\vec{k}_4$ and the integration over the azimuthal angles ϕ_1, ϕ_2 analytically [LLLM02], so that only six integrations are left

$$\Sigma_q^>(k,\omega) = -i\frac{2\hbar^2}{(2\pi)^6}\sum_{q'}\left\{\mid\mathcal{M}_{qq'}\mid^2\int \mathrm{d}\omega_2\int \mathrm{d}\omega_3\int \mathrm{d}k_3 k_3^2\int \mathrm{d}k_2 k_2^2\frac{d\cos\theta_2}{k_{tot}k_3}\right.$$
$$\times\,\mathcal{A}_{q'}(k_2,\omega_2)f_{q'}(k_2,\omega_2)\mathcal{A}_{q'}(k_3,\omega_3)(1-f_{q'}(k_3,\omega_3))$$
$$\left.\times\int \mathrm{d}k_4 d\int \omega_4 k_4\mathcal{A}_q(k_4,\omega_4)(1-f_q(k_4,\omega_4))\right\}, \qquad (5.3)$$

$$\Sigma_q^<(k,\omega) = i\frac{2\hbar^2}{(2\pi)^6}\sum_{q'}\left\{\mid\mathcal{M}_{qq'}\mid^2\int \mathrm{d}\omega_2\int \mathrm{d}\omega_3\int \mathrm{d}k_3 k_3^2\int \mathrm{d}k_2 k_2^2\frac{d\cos\theta_2}{k_{tot}k_3}\right.$$
$$\times\,\mathcal{A}_{q'}(k_2,\omega_2)(1-f_{q'}(k_2,\omega_2))\mathcal{A}_{q'}(k_3,\omega_3)f_{q'}(k_3,\omega_3)$$
$$\left.\times\int \mathrm{d}k_4 d\int \omega_4 k_4\mathcal{A}_q(k_4,\omega_4)f_q(k_4,\omega_4)\right\}. \qquad (5.4)$$

Here $k_{tot} =\mid \vec{k}+\vec{k}_2\mid$ is the total momentum and $\omega_4 = \omega+\omega_2-\omega_3$. The integrand in Eq. (5.3) and Eq. (5.4) contains the spectral function $\mathcal{A}(k,\omega)$ for each integration. Numerical problems might occur due to the fact that the spectral function is sharply peaked near the on-shell point. Therefore, we use a substitution to remove the peak

from the integrand in our numerical simulation

$$\int\limits_{k_{min}}^{k_{max}} \mathrm{d}k k \mathcal{A} = \int\limits_{k_{min}^2}^{k_{max}^2} \frac{\mathrm{d}k^2}{2} \mathcal{A} = \int\limits_{y(k_{min})}^{y(k_{max})} \mathrm{d}y. \tag{5.5}$$

Inspired by the denominator of the spectral function $\mathcal{A}(k, \omega)$ and using $\mathrm{d}\arctan(x)/\mathrm{d}x = (x^2 + 1)^{-1}$, we construct the function

$$\frac{y}{2} = \arctan\left[\frac{2}{\Gamma}\left(\hbar\omega - \frac{\hbar^2 k^2}{2m^*} - U^{eff} - \mathrm{Re}\Sigma\right)\right], \tag{5.6}$$

$$\frac{\mathrm{d}y}{\mathrm{d}k^2} = \frac{\hbar^2 \Gamma}{2m^*} \frac{1}{\frac{\Gamma^2}{4} + \left(\hbar\omega - \frac{\hbar^2 k^2}{2m^*} - U^{eff} - \mathrm{Re}\Sigma\right)} = \frac{\hbar^2}{2m^*} \mathcal{A}. \tag{5.7}$$

We note that Γ and $\mathrm{Re}\Sigma$ are taken at the on-shell point and the derivative is only taken with respect to the momentum k. Using Eq. (5.7) and Eq. (5.6) with the integral Eq. (5.5) yields

$$\int\limits_{k_{min}^2}^{k_{max}^2} \mathrm{d}k^2 \mathcal{A} = \int\limits_{y(k_{min})}^{y(k_{max})} \mathrm{d}y \frac{\mathrm{d}k^2}{\mathrm{d}y} \mathcal{A} = \frac{2m^*}{\hbar^2} \int\limits_{y(k_{min})}^{y(k_{max})} \mathrm{d}y, \tag{5.8}$$

which is easier to handle numerically than the original integral. We refer to [Fro06] for a more detailed dicussion. For the multidimensional integration we use the routine CUBPACK [CH03]. The numerical calculations were done on an energy and momentum grid (E, q) with -1.0 GeV $\leq E \leq 1.0$ GeV and $0 \leq q \leq 1.25$ GeV/c, where $E = \hbar\omega$ and $q = \hbar k$ using 120 steps in each direction. It turned out that using a narrower grid affects the results only at an insignificant level, but leads to higher numerical effort in the calculation. Therefore, using 120 steps in each direction is a choice of good balance between accuracy and numerical effort.

For technical reasons we introduced the form factor

$$F_q(\omega_2, \omega_3) = e^{(\omega_2 - \omega_3 - \omega_{Fq})^4/\Lambda^4}, \tag{5.9}$$

where we used $\Lambda = 0.5$ GeV. The influence of the form factor is shown in Fig. 5.1. Without the form factor the width is increasing with increasing energy. This behavior is unrealistic and leads, as we will see later, to mathematical problems when we calculate the real part of the self-energy. The form factor $F_q(\omega_2, \omega_3)$ leads to a decrease of the width in the high energy region and leaves the width unchanged near the Fermi surface.
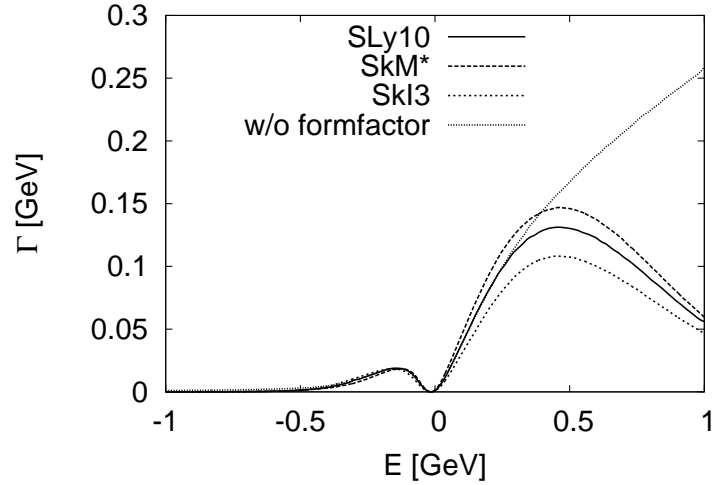
Figure 5.1: The width of the nucleons with momentum $q = 0.300$ GeV/c in symmetric nuclear matter at saturation density .

5.2 The Width

In the width, which corresponds to the imaginary part of the self-energy (see Eq. (2.79)), the influence of correlations is reflected most clearly and directly. If we add a particle with momentum q and energy E to or remove such a particle from the many-body ground state the life time τ of that state is given by the inverse of the width Γ [DVN05, KB62]

$$\tau \sim 1/\Gamma. \tag{5.10}$$

Therefore, the width is directly proportional to the correlations taking place, for a lager width we have more correlations in a many-body system. The boundary condition for the Green's functions Eq. (2.35) implies [KB62] that

$$\Sigma^<(\vec{k}, \omega) = e^{-\beta(\hbar\omega - \mu)} \Sigma^>(\vec{k}, \omega), \tag{5.11}$$

where $\beta = 1/kT$. In a fermion system at zero temperature the $\Sigma^<$ vanishes for $\omega > \mu$ and can be interperted as the life time of a hole state, while $\Sigma^>$ vanishes for $\omega < \mu$ and can be interperted as the life time of a particle state. Therefore, the width Γ below the Fermi energy ϵ_f is given by the one-particle-two-hole self-energy (1p2h) $\Sigma^<$ and by two-particle-one-hole (2p1h) self-energy $\Sigma^>$. At the Fermi-edge it vanishes, which means that particles close to the Fermi-surface have an infinitely long life-time as required for a stable ground state.

Results for the nucleon width for different Skyrme parameterizations in nuclear matter at the saturation density $\rho = 0.16$ are shown in Fig. 5.1 for symmetric nuclear matter and in Fig. 5.2 for neutron rich nuclear matter with an asymmetry coefficient $Y = 0.25$. For symmetric nuclear matter the width Γ agrees for all Skyrme parameterizations in the global energy dependence and shows a strong increase of the width for high energies. While the width for $E < \epsilon_f$ agrees very well for all Skyrme parameter set the width shows variations for energies above the Fermi edge $E > \epsilon_f$. These variations are due to differences in the interaction strength, which we observed in chapter 4.

For neutron rich matter the results obtained with different Skyrme parameterizations show a slightly different behavior. Comparing the proton width to the neutron width, one sees a shift of the Fermi edge. Since there are less proton states occupied the proton Fermi energy is smaller than in symmetric nuclear matter. For the neutrons the situation is reversed, more neutron states are occupied and the Fermi edge lies higher than in the symmetric case. All Skyrme parameterizations, which we examined in this work, shows this splitting into a neutron and proton Fermi sphere with good agreement. Qualitatively the total slope of the width agrees for all parameterizations. Quantitatively there is a deviation reflecting again the fact that we obtained different interaction matrix elements for the parameterizations. However similar differences are observed in Brueckner-Hartree-Fock (BHF) calculations when using different NN-potentials. In Fig. 5.3 we compare our results for the SLy10 Skyrme parameterization in neutron rich matter with $Y = 0.25$ to the results of recent BHF calculation using the Bonn and Nijmegen NN-potentail [HM04]. Our results agree qualitatively in the global energy dependence, but in detail differences are seen on the quantitative level. However, the results of the [HM04] show also differences when using different NN-potentials, as seen in Fig. 5.3.
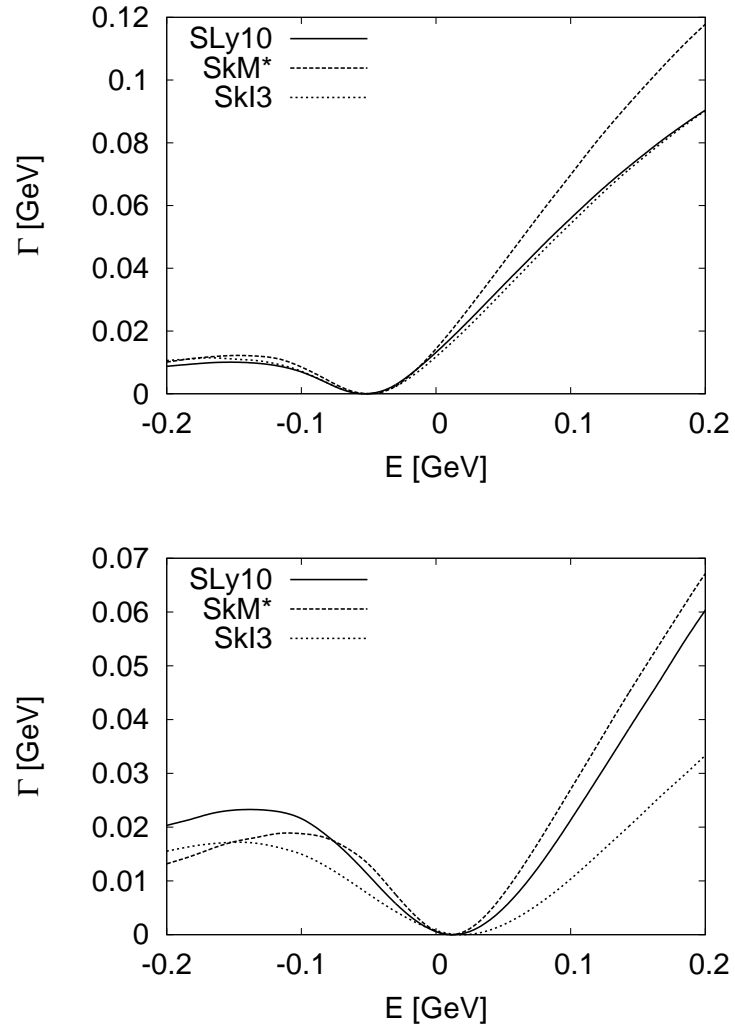
Figure 5.2: The width for protons (upper graph) and neutron (lower graph) in neutron rich matter $Y = 0.25$ for different Skyrme parameterizations at nuclear matter saturation density $\rho = 0.16$ fm^{-3}. The picture refers to a momentum of q=0.300 GeV/c.
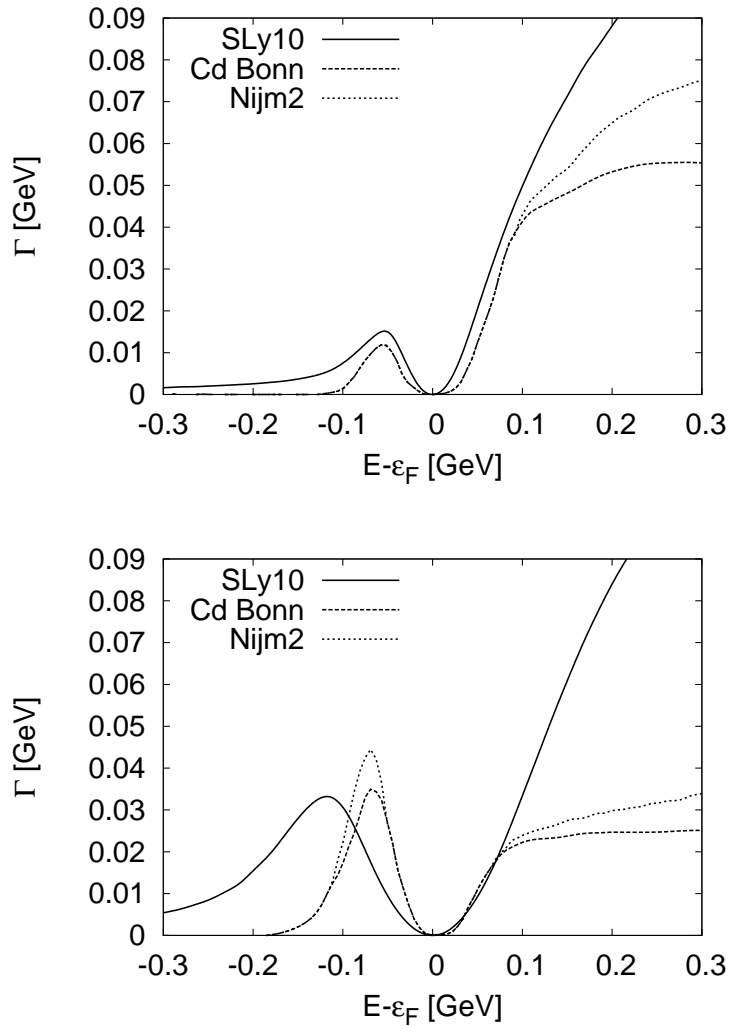
Figure 5.3: The width for protons (upper graph) and neutron (lower graph) in neutron rich matter with asymmetry coefficient $Y = 0.25$ for $q = 0.4q_{F_q}$ at a density $\rho = 0.17$ fm^{-3}. The results of our calculation, using the SLy10 Skyrme parameterization, are compared to the results of [HM04], using the Bonn and Nijmegen NN-potential.

5.3 Real Part of the Self-Energy

As shown by Lehr et al. [LLLM02], neglecting the real part of the collisional self-energy violates the analyticity of the spectral function, which leads to the wrong behavior of the momentum distribution and contradicts the conservation of the quantum mechanical probability. We have seen in chapter 2.7 that the real part of the self-energy is given by

$$\text{Re}\Sigma^{(r)}(k,\omega) = \Sigma_{MF}(k) + \Sigma_{dis}(k,\omega), \tag{5.12}$$

where $\Sigma_{dis}(k,\omega)$ is calculated from the collisional part of the self-energy using the dispersion relation. Since the dispersion integral in general determines the real part, except for a constant which comes from complex integration [BD67], we impose the constraint

$$\Sigma^{(r)}(k,\epsilon_{on}) \overset{!}{=} \Sigma_{MF}(k) \tag{5.13}$$

at the energy shell $\epsilon_{on} = \hbar^2 k^2/(2m^*) + U^{eff}$. This condition is fullfilled for the subtracted dispersion relation

$$\text{Re}\Sigma_{dis}(k,\omega) = \mathcal{P}\int \frac{d\omega'}{2\pi}\Gamma(k,\omega')\left\{\frac{1}{\omega-\omega'} - \frac{1}{\epsilon_{on}-\omega'}\right\} \tag{5.14}$$

$$= (\epsilon_{on}-\omega)\,\mathcal{P}\int \frac{d\omega'}{2\pi}\frac{\Gamma(k,\omega')}{(\epsilon_{on}-\omega')(\omega-\omega')}.$$

For the calculation of the real part we have to solve integrals of the form

$$I(\omega) = \mathcal{P}\int \frac{d\omega'}{2\pi}\frac{f(\omega')}{\omega-\omega'}. \tag{5.15}$$

The integrand in the last line of Eq. (5.15) is not analytic at the point ω, this is actually the reason why we have to take the principal value. To remove the singularity at the point ω, we use

$$\mathcal{P}\int \frac{d\omega'}{2\pi}\frac{1}{\omega'-\omega} = 0, \tag{5.16}$$

allowing to add and subtract the term $\mathcal{P}\int \frac{d\omega'}{2\pi}\frac{f(\omega)}{\omega'-\omega}$ to and from Eq. (5.15), respectively:

$$I(\omega) = \mathcal{P}\int \frac{d\omega'}{2\pi}\frac{f(\omega')}{\omega-\omega'} + \mathcal{P}\int \frac{d\omega'}{2\pi}\frac{f(\omega)}{\omega'-\omega} - \mathcal{P}\int \frac{d\omega'}{2\pi}\frac{f(\omega)}{\omega'-\omega}$$

$$= \mathcal{P}\int \frac{d\omega'}{2\pi}\frac{f(\omega')-f(\omega)}{\omega-\omega'} - f(\omega)\mathcal{P}\int \frac{d\omega'}{2\pi}\frac{1}{\omega'-\omega}$$

$$= \mathcal{P}\int \frac{d\omega'}{2\pi}\frac{f(\omega')-f(\omega)}{\omega-\omega'}. \tag{5.17}$$
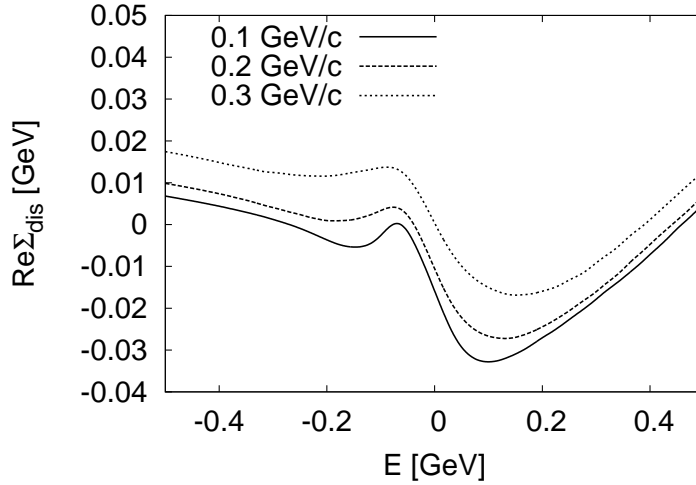
Figure 5.4: The real part of the self-energy obtained by the dispersion relation in symmetric nuclear matter for different momenta, calculated with the SLy10 Skyrme parameterization.

The integrand of the integral in the last line of Eq. (5.17) is now analytic, since

$$\lim_{\omega' \to \omega} \frac{f(\omega') - f(\omega)}{\omega - \omega'} = -\frac{\mathrm{d}f(x)}{\mathrm{d}x}. \tag{5.18}$$

Therefore, we can replace the Cauchy principal value $\mathcal{P}$ Eq. (5.17) by an ordinary integration

$$I(\omega) = \int \frac{\mathrm{d}\omega'}{2\pi} \frac{f(\omega') - f(\omega)}{\omega - \omega'}. \tag{5.19}$$

We note that the formfactor Eq. (5.9) ensures that the integral is ultraviolet convergent.

Fig. 5.4 shows the results for the real part of the self-energy, which is obtained by the dispersion relation . Compared to the width, the real dispersive part is much smaller. One clearly sees that the real part fulfills initial assumption and the dispersive part of the real self-energy $\mathrm{Re}\Sigma_{dis}(k,\omega)$ vanishes at the on-shell point.

5.4 The Spectral Function

The peak of the spectral function $\mathcal{A}$ is mainly influenced by the first term in the nominator of Eq. (2.78), hence the spectral function is peaked around the root of

the on-shell energy

$$\epsilon_{on} = \frac{\hbar^2 k^2}{2m} + \Sigma_{MF}(k) + \text{Re}\Sigma(k, \epsilon_{on}). \qquad (5.20)$$

We note that in our approach the real part is defined such that $\text{Re}\Sigma(k, \epsilon_{on}) = 0$ (see Eq. (5.13)). Therefore, it follows that the position of the peak is mainly affected by the mean-field

$$\epsilon_{on} = \frac{\hbar^2 k^2}{2m} + \Sigma_{MF}(k). \qquad (5.21)$$

This can be observed in Fig. 5.5 and Fig. 5.6, where the spectral functions for nucleon in symmetric and asymmetric nuclear matter are shown. Fig. 5.5 shows the spectral function $\mathcal{A}$ for momenta $q = 0.1$ GeV/c (upper panel) and $q = 0.3$ GeV/c (lower panel) in symmetric matter using different parameterizations for the Skyrme energy functional. All results obtained using the different Skyrme parameters agree very well. For both momenta the quasi-particle peak can be clearly seen, for the momentum $q = 0.1$ GeV/c inside the Fermi sea and for $q = 0.3$ GeV/c outside the Fermi sea. This is easy to understand, since $\epsilon_{on} < \epsilon_F$ for $q < q_F$ and since $\epsilon_{on} < \epsilon_F$ for $q < q_F$. Comparing the width of the quasiparticle peaks shows that the peak for $q = 0.1$ GeV/c is broader than the peak for $q = 0.3$ GeV/c. The width, which determines the profile of the quasiparticle peak, becomes very small close to the Fermi edge, hence the quasiparticle peak becomes very sharp. For $q = 0.3$ GeV/c the quasiparticle peak is closer to the Fermi edge than for $q = 0.1$ GeV/c, therefore, it is even sharper.

In Fig. 5.6 results for the proton and neutron spectral function in neutron rich nuclear matter ($Y = 0.25$) are shown. Both types of particles have the momentum $q = 0.3$ GeV/c. Since in neutron rich matter the Fermi sphere is greater for neutrons than for protons, the Fermi energy for neutrons is higher. This leads to the observation that the protons leave the Fermi sea earlier than the neutrons, as can be seen in Fig. 5.6. Both types of particles carry the same momentum, but while the neutrons are still in the Fermi sea, the protons have already left it. For different Skyrme parameterizations we obtain similar results. While for the protons we have good agreement, the results for the neutrons show slight differences. For the SkI3 Skyrme parameterization the Fermi energy is shifted to a higher energy. Because of its sharp structure, this is better seen for the spectral function than for the width. These differences reflect the uncertainties of the Skyrme parameters fitted to different data and they are comparable to the differences observed in BHF calculations when using different NN-potentials (see Fig. 5.3).
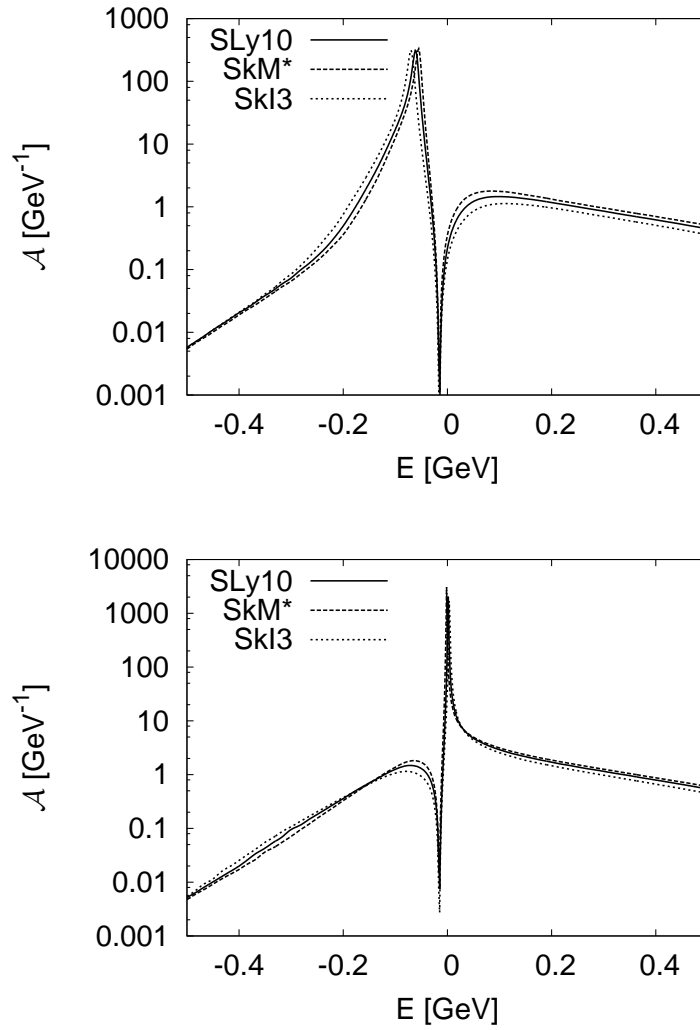
Figure 5.5: The nucleon spectral function in symmetric nuclear matter at saturation density. The upper panel refers to a momentum of $k = 0.100$ GeV/c and the lower panel to a momentum of $k = 0.300$ GeV/c.
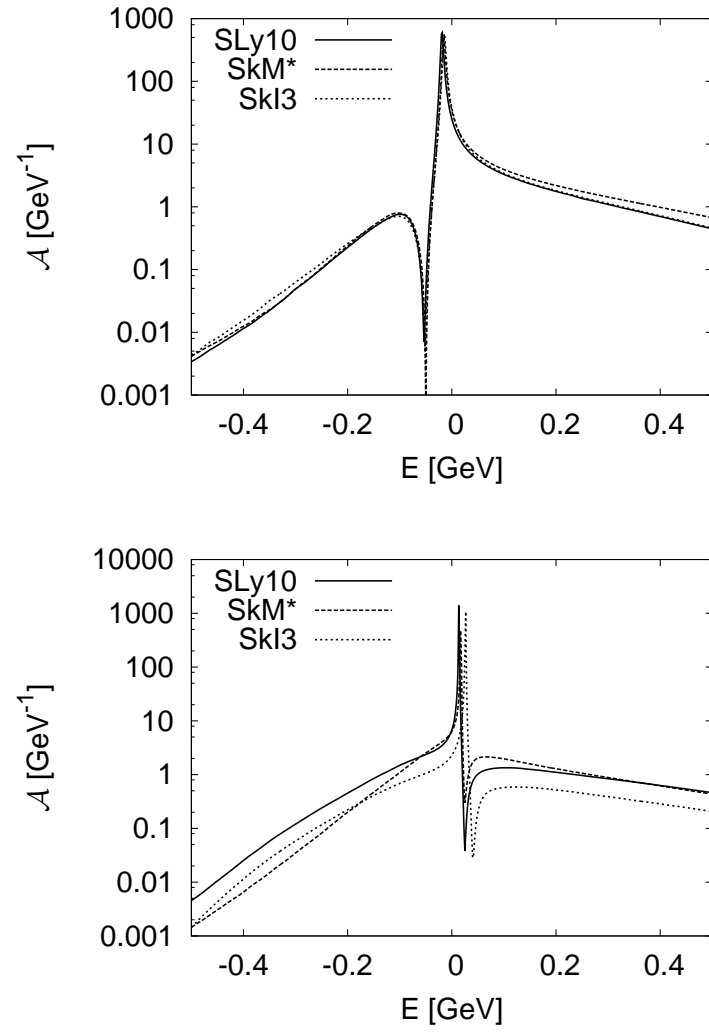
Figure 5.6: The spectral function for protons (upper panel) and neutrons (lower panel) for momentum $q = 0.3$ GeV in asymmetric nuclear matter ($Y = 0.25$).

5.5 The Momentum Distribution and the Spectroscopic Factor

The influence of correlations can very clearly bee seen by the examination of the nucleon momentum distribution. For a Fermi gas of pure quasiparticles the momentum distribution is a step function $n_q(k)^0 = \theta(k_{F_q}^2 - k^2)$. In a correlated Fermi gas the momentum distribution can be generated from the hole part of the spectral function [DVN05]

$$n_q(k) = \int\limits_{-\infty}^{\epsilon_{F_q}} \frac{dE}{2\pi} \mathcal{A}_q(E, k), \tag{5.22}$$

where ϵ_{F_q} is the Fermi energy.

In Fig. 5.7 we compare the momentum distribution of the nucleon in nuclear matter at saturation density for different Skyrme parameterization. One sees the depletion of the Fermi-sphere of about 10%. This fraction of spectral strength is shifted into the high momentum tail, as can be seen in the lower panel of Fig. 5.7. The results for the SLy10 and SkM* Skyrme parameterization, where the pion contribution is subtracted, are in good agreement with the result of a full many-body calculation taken from [BF00]. The importance of the substraction of the pion contribution is also shown in Fig. 5.7. The result, where we did not subtract the pion contribution, leads to less depletion in the Fermi sphere. As we saw in chapter 4, the subtraction of the pion contribution leads to an increase of the interaction matrix element. Therefore, subtracting the long range contribution in our approach seems to be essential.

Results for the momentum distribution in neutron rich matter at saturation density are shown in 5.8. In asymmetric nuclear matter the structure of the momentum distribution follows closely the same pattern as found already in symmetric nuclear matter. Also here, the sates in the Fermi sea are shifted into the high energy tail. However, there are seen differences when comparing the results for protons and neutrons. In asymmetric nuclear matter the Fermi edges for neurons and protons are different due to higher number of neutrons in the medium. Beyond that, one sees a higher depletion of the Fermi sea for protons than for neutrons. This has two reasons, at the one hand more states in the phase space are Pauli blocked for the protons, at the other hand this effect is increased by the higher interaction matrix element for protons than for neutrons in neutron rich matter (see Fig. 4.7). This observation is in agreement with our previous work [KLM05] and with BHF calculations of theTübingen group [HM04]. Hassaneen et al. claimed that the depletion of the protons is mainly due to the tensor interaction. Since our approach does not contain an explicit tensor interaction, we cannot make any prediction about that.
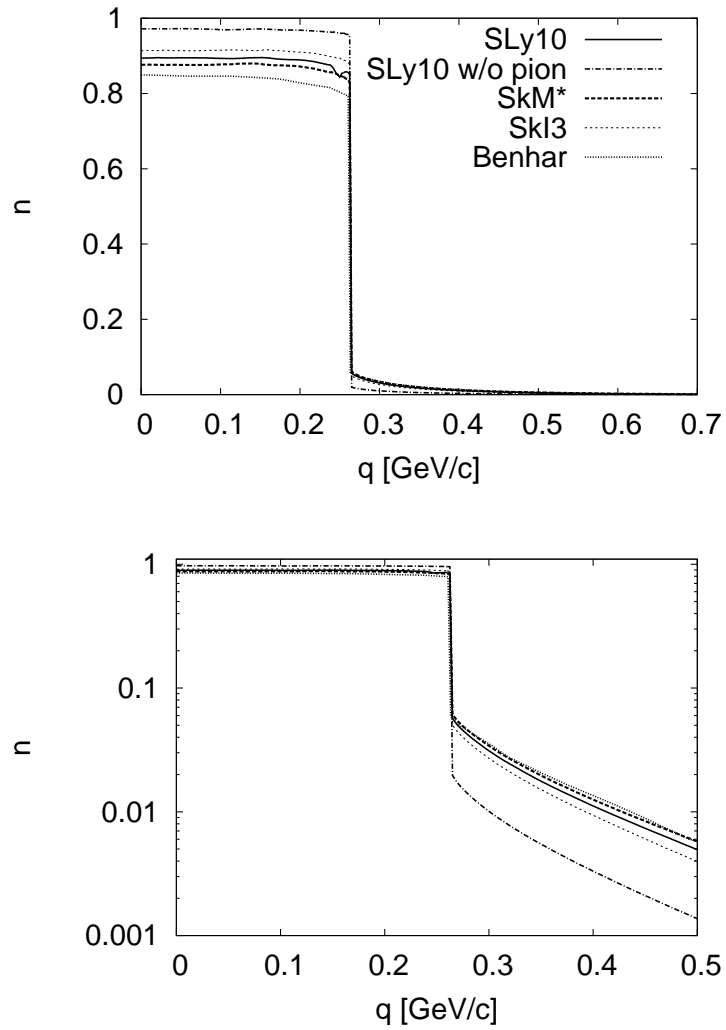
Figure 5.7: The momentum distribution of symmetric nuclear matter. The picture shows calculations using the Skyrme parameterization SLy230a and SkM*. The results are compared with [BF00]. The dashed-dotted line refers to a calculation, where the pion contribution was not subtracted.
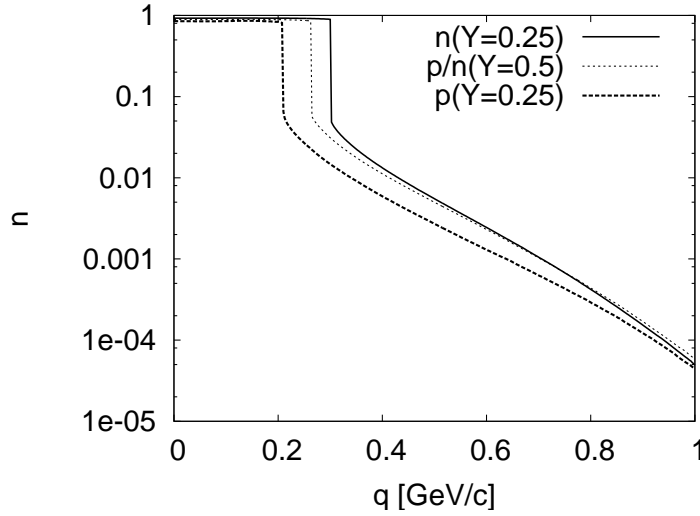
Figure 5.8: The momentum distribution for protons and neutrons in neutron rich nuclear matter at saturation density obtained using the SLy10 Skyrme parameterization . The results are compared with the momentum distribution for nucleons in symmetric nuclear matter.

It can be shown that the discontinuity of the momentum distribution is directly related to the quasi particle strength [DVN05]. As we saw in the previous section, the spectral function is peaked around the on-shell energy ϵ_{on}. If we expand the real part of the self-energy around the on-shell point, we obtain for the first term in the nominator of the spectral function $\mathcal{A}$ Eq. (2.78)

$$(E - \epsilon_{on} - \text{Re}\Sigma(k,E)) \simeq (E - \epsilon_{on}) \left(1 - \left. \frac{\partial \text{Re}\Sigma(k,E)}{\partial E} \right|_{E=\epsilon_{on}} \right) \qquad (5.23)$$

We define the quasiparticle strength, or spectroscopic factor $Z_F(k)$, as

$$Z_F(k) = \left(1 - \left. \frac{\partial \text{Re}\Sigma(k,E)}{\partial E} \right|_{E=\epsilon_{on}} \right)^{-1}. \qquad (5.24)$$

The quasiparticle strength tells us how much strength is left in the quasiparticle state. The lower the quasiparticle strength the more particles are correlated and strength is shifted into many-body configurations. It can be shown that the discontinuity of the momentum distribution is given by the particle strength Z_F at the Fermi surface [DVN05]

$$\lim_{\eta \to 0} \left[n(k_f - \eta) - n(k_f + \eta) \right] = Z_F, \qquad (5.25)$$

which is called Migdal-Luttinger theorem [Mig57], [Lut60].

In the upper panel of Fig. 5.9 results for the quasiparticle strength in symmetric nuclear matter are shown. The results are compared to results of [Leh03] and [BFF92] and agree very well besides for small variations. One clearly sees that the quasiparticle strength only differers from unity near the Fermi edge. At the Fermi-momentum $q = q_F$ the strength reaches a minimum. This observation confirms the assumption of our approach, where we assumed a local interaction in nuclear matter taking place basically at the Fermi surface. However, the results of [BFF92] predict a smaller value for the quasiparticle strength at the Fermi edge than our model. This fact is directly connected with the momentum distribution in Fig. 5.7, where the results of Benhar showed a higher depletion of the Fermi sea.

Results for protons and neutrons in neutron rich nuclear matter are shown in the lower panel of Fig. 5.9 in comparison to symmetric nuclear matter. We observe less correlations for the neutrons in neutron rich nuclear matter than in symmetric nuclear matter. For the protons we observe a small increase of the correlations. Again, this effect is directly connected with the momentum distribution in neutron rich matter. As we observed in Fig. 5.8, the protons show a higher depletion in the Fermi sea in neutron rich nuclear matter than in symmetric nuclear matter. For neutrons the situation is reversed: neutrons in neutron rich nuclear matter are not so strongly correlated than in symmetric nuclear matter. This fact can be explained, as we pointed out before, by the change in the phase space and the higher interaction matrix element for protons than for neutrons in neutron rich nuclear matter.
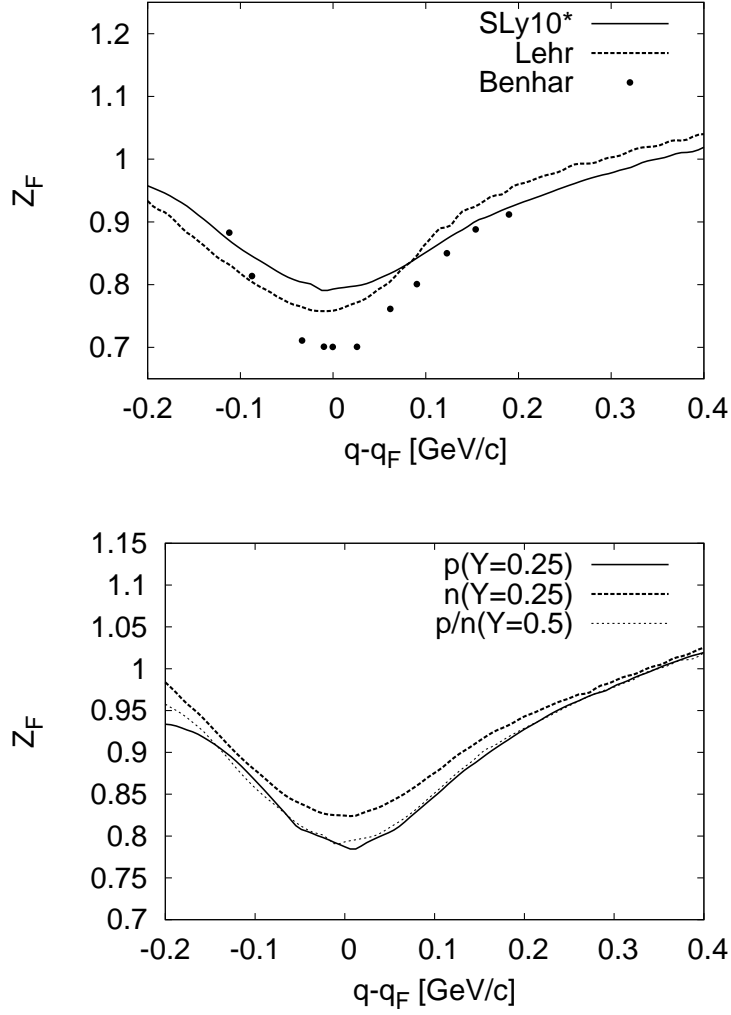
Figure 5.9: The quasiparticle strength for protons and neutrons in symmetric (upper panel) and neutron rich (lower panel) nuclear matter. The dashed line in the upper panel line refers to results from [Leh03] and the dots in the upper panel refer to results from Benhar [BFF92].

6 Dynamical Correlations in Hypernuclear Matter

In this chapter we investigate correlations in hypernuclear matter. So far results for dynamical correlations of a single Λ-hyperon in nuclear matter have been reported by [HJPRM96] and [RD04], but no systematical investigation of dynamical correlations in hypernuclear matter has been done. At the beginning of this chapter we show how to extend our approach from chapter 5 to the strange strange sector. Since the Λ-hyperons interact with the nucleons, it is not sufficient to just add the Λ-hyperons as independent particles, rather the self-consistent calculation affects all parts of the self-energies of all baryons. At the end we show results for hypernuclear matter and β-equilibrated nuclear matter.

6.1 The Mean-Field Contribution

The first extension of the Skyrme approach to the hypernuclear sector was done by Rayet [Ray81]. This approach was essentially phenomenological due to the fact of poor amount of hypernuclear data. With the first measurements of the Λ hypernuclear energy levels in medium and heavy systems at BNL [P$^+$91], reasonable Λ-nucleon Skyrme parameterizations appeared [YBZ88, MDG88, FLAP89]. Lanskoy and Yamamoto [YBZ88] determined the parameters by using data from Λ hypernuclear spectra of nuclear mass numbers up to $^{208}_{\Lambda}$Pb by the (π^+, K^+) reaction at KEK [HHH$^+$96]. The interaction of their parameterization was motived by G-matrix calculations performed with the Jülich and Nijmegen potentials. Finally, Lanskoy extended the Skyrme interaction to the $\Lambda\Lambda$ sector [Lan98] using data from double-Λ hypernuclei. We adopt the notation from Ref. [Mor05] and name the set numbered I-V from [LY97] for the NΛ interactions LYI-LYV and the sets numbered 1-6 from [YBZ88] are named YBZ1-YBZ6.

In Table 6.1 and table 6.2 a selection of Skyrme parameters for for the NΛ-interaction [LY97, YBZ88] and $\Lambda\Lambda$-interaction [Lan98] can be found.

Model	LY-I	LY-IV	YBZ-1	YBZ-5	YBZ-6
u_0	-476.0	-542.5	-349.0	-315.3	-372.2
u_1	42.0	56.0	67.61	23.14	100.4
u_2	23.0	8.0	37.39	-23.14	79.60
u_3	1514.1	1387.9	2000.0	2000.0	2000.0
y_0	-0.0452	-0.1534	-0.108	-0.109	-0.107
y_3	-0.280	0.1074	0.0	0.0	0.0
β	1/3	1/3	1	1	1

Table 6.1: Skyrme parameters for the NΛ interaction [LY97, YBZ88], u_0 is given in MeV fm^3, u_1 and u_2 are given in MeV fm^5, u_3 is in given Mev fm$^{3+3\beta}$, all other parameters are dimensionless.

Model	SLL1	SLL2	SLL3
λ_0	-312.6	-437.7	831.8
λ_1	57.5	240.7	922.9

Table 6.2: Skyrme parameters for the $\Lambda\Lambda$ interaction [Lan98], λ_0 is given in MeV fm^3 and u_1 is given in MeV fm^5.

The Skyrme approach can be generalized by using the following ansatz for the NΛ and $\Lambda\Lambda$ interaction

$$
\begin{aligned}
v_{N\Lambda}(r_N - r_\Lambda) &= u_0(1 + y_0 P_\sigma)\delta(r_N - r_\Lambda) + \frac{1}{2}u_1[k'2\delta(r_N - r_\Lambda) \\
&\quad + \delta(r_N - r_\Lambda)k^2] + u_2 k'\delta(r_N - r_\Lambda)k \\
&\quad + \frac{3}{8}u_3(1 + y_3 P_\sigma)\rho_N^\beta\left(\frac{r_N + r_\Lambda}{2}\right)\delta(r_N - r_\Lambda)
\end{aligned}
\tag{6.1}
$$

$$
\begin{aligned}
v_{\Lambda\Lambda}(r_1 - r_2) &= \lambda_0\delta(r_1 - r_2) + \frac{1}{2}\lambda_1[k'2\delta(r_1 - r_2) + \delta(r_1 - r_2)k^2] \\
&\quad + \lambda_2 k'\delta(r_1 - r_2)k + \frac{3}{8}\lambda_3\rho_\Lambda\rho_N^\gamma,
\end{aligned}
\tag{6.2}
$$

where we neglected spin orbit terms, since they play no role in infinite matter. For the expectation value of the energy we obtain

$$
E = \langle\phi|H|\phi\rangle = \int \mathcal{H}(\vec{r})d^3r,
\tag{6.3}
$$

where the Hamiltonian is given by

$$
H = \sum_{I=N,\Lambda} T_I + \frac{1}{2}\sum_{I,J=N,\Lambda} V_{IJ}.
\tag{6.4}
$$

Due to the additional NΛ and ΛΛ interactions in the Hamiltonian Eq. (6.4), we obtain additional terms for the energy density $\mathcal{H}$ Eq. (3.13)

$$\mathcal{H} = \mathcal{H}_{NN} + \mathcal{H}_{N\Lambda} + \mathcal{H}_{\Lambda\Lambda}. \tag{6.5}$$

Here, the NΛ and ΛΛ energy densities are given by

$$\mathcal{H}_{N\Lambda} = u_0(1 + \frac{y_0}{2})\rho_N\rho_\Lambda + \frac{3}{8}u_3\rho_N^{\beta+1}\rho_\Lambda(1 + \frac{y_3}{2}) \tag{6.6}$$

$$+ \frac{1}{8}[u_1(2 + y1) + u_2(2 + y_2)](\rho_N\tau_\Lambda + \rho_\Lambda\tau_N),$$

$$\mathcal{H}_{\Lambda\Lambda} = \frac{\hbar^2}{2m_\Lambda} + \frac{\lambda_0}{4}\rho_\Lambda^2 + \frac{1}{8}(\lambda_1 + 3\lambda_2)\rho_\Lambda\tau_\Lambda + \frac{\lambda_3}{4}\rho_\Lambda^2\rho_N^\gamma. \tag{6.7}$$

We note that $\rho_N = \rho_n + \rho_p$ and $\tau_N = \tau_p + \tau_n$ are the total nucleon and total nucleon kinetic density, respectively. From the energy densities Eq. (6.6) and Eq. (6.7) directly follows the equation of state (see Eq. (3.26)).

In Fig. 6.1 the equation of state for hypernuclear matter is shown. The results are obtained by using the SLy10 Skyrme parameterization together with the LYI and SLL2 Skyrme parameterization for the NΛ and ΛΛ interaction, respectively. In the upper panel the energy per particle is shown without considering the particle masses, while in the lower panel the particle masses are considered. The number density of protons and neutrons are assumed to be equal. Interestingly, the local minimum of the energy per particle is shifted to higher densities when mixing in more Λ particles, as seen in the upper panel. The absolute minimum of the energy per particle is achieved for $Y_\Lambda \simeq 0.15$. However, since the mass of the Λ-hyperon is about 170 MeV higher than the masses of the nucleons, matter under normal conditions contains no strange particles and normal nuclear matter remains to defining the ground state of baryonic matter. This can bee seen in the lower panel, where the masses of the particles are taken into account. Here, the absolute minimum is found a nuclear matter density and $Y_\Lambda = 0$, which matches with our common experience. But for nuclear matter at extreme high densities, as found i.e. in neutrons stars or heavy ion collisions, strange particles are found. We will discuss that point later in connection with the particle fraction in β-equilibrated nuclear matter.

The effective Λ-hyperon mass m_Λ^* and the effective Λ-hyperon potential U_Λ^{eff} can be extracted from Eq. (6.6) and Eq. (6.7), respectively:

$$\frac{m_\Lambda}{m_\Lambda^*} = 1 + \frac{2m_\Lambda}{\hbar^2}\left(\frac{1}{8}[\lambda_1 + \lambda_3]\rho_\Lambda + \frac{1}{8}[u_1(2 + y_1) + u_2(2 + y_2)]\rho_\Lambda\right), \tag{6.8}$$

$$U_\Lambda^{eff} = \frac{\lambda_0}{2}\rho_\Lambda + \frac{\lambda_3}{2}\rho_\Lambda\rho_N^\gamma\frac{1}{8}(\lambda_1 + 3\lambda_2)\tau_\Lambda + u_0(1 + \frac{y_0}{2})\rho_N \tag{6.9}$$

$$+ \frac{3}{8}u_3(1 + \frac{y_3}{2})\rho_N^{\beta+1} + \frac{1}{8}[u_1(2 + y1) + u_2(2 + y_2)]\tau_N.$$

In presence of Λ-hyperons also the effective masses and the effective potentials for the nucleon are modified

$$\frac{m_N}{m^*_{q(\Lambda)}} = \frac{m_N}{m^*_q} + \frac{2m_N}{\hbar^2}(\frac{1}{8}[u_1(2+y_1) + u_2(2+y_2)]\rho_\Lambda) \tag{6.10}$$

$$U^{eff}_{q(\Lambda)} = U^{eff}_q + \frac{\lambda_3}{4}\gamma\rho_\Lambda^2\rho_N^{\gamma-1} + u_0\left(1 + \frac{y_0}{2}\right)\rho_\Lambda \tag{6.11}$$
$$+ \frac{3}{8}u_3(\beta+1)\left(1 + \frac{y_3}{2}\right)\rho_N^\beta\rho_\Lambda\frac{1}{8}[u_1(2+y_1) + u_2(2+y_2)\tau_\Lambda.$$

In Fig. 6.2 and Fig. 6.3 the effective mass and the effective potential in hyper nuclear matter are shown, respectively. The results are compared using the SLy10, LY1 and SLL2 and SkI3, YBZ6 and SLL2 Skyrme parameterization for the NN, NΛ and $\Lambda\Lambda$ interaction, respectively. The effective mass increases for the nucleons nearly linearly with increasing strangeness, as seen in upper panel of Fig. 6.2. The situation of the Λ-hyperons is different, here the behavior depends on the chosen Skyrme parameterization. While for the SLy10+LYI+SLL2 Skyrme parameterization sets the mass decreases with increasing strangeness fraction, the Λ-hyperon behave opposite for the SkI3+YBZ6+SLL2 parameter sets, with increasing strangeness the mass increases nearly linearly. In Fig. 6.3 we show results for the effective potential. The upper panel we see that nucleons in hypernuclear matter are less bound, while the Λ-hyperon is stronger bound, as seen in the lower panel.
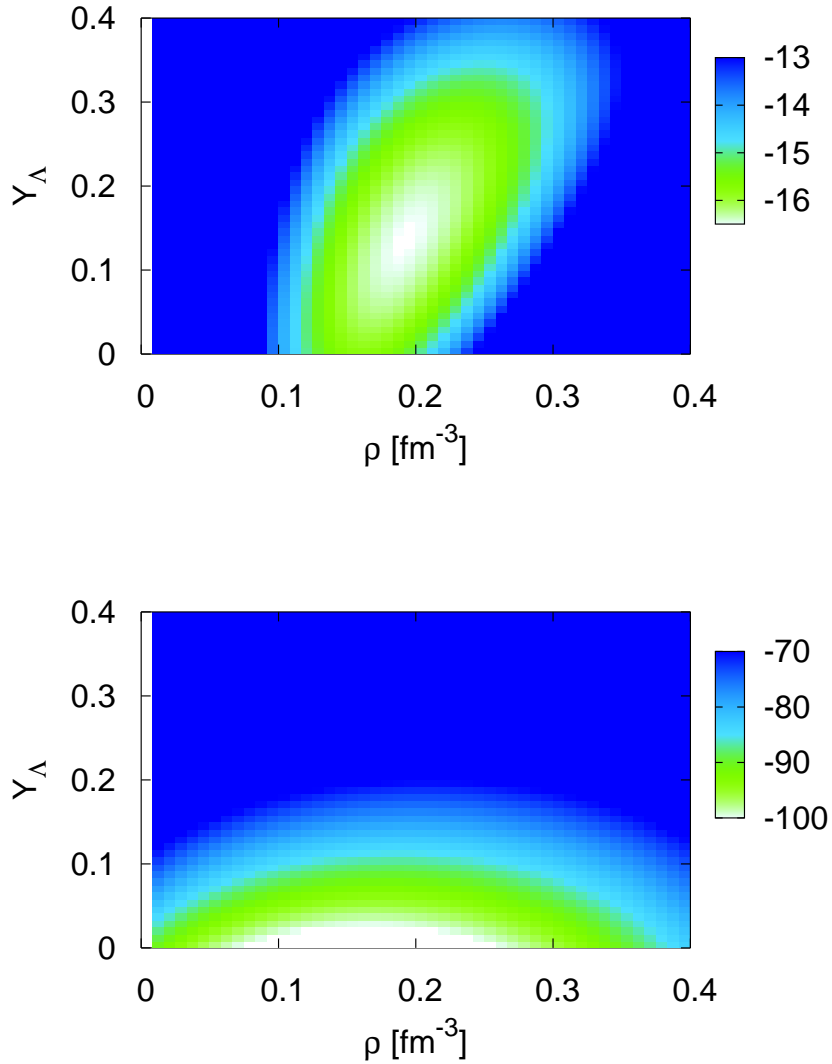
Figure 6.1: The equation of state for hypernuclear matter obtained with the SLy10, SLY1 and SLL2 Skyrme parameterization.In the lower picture we accounted for the baryon masses and subtracted $(m_\Lambda + m_N)/2$ for convenience.
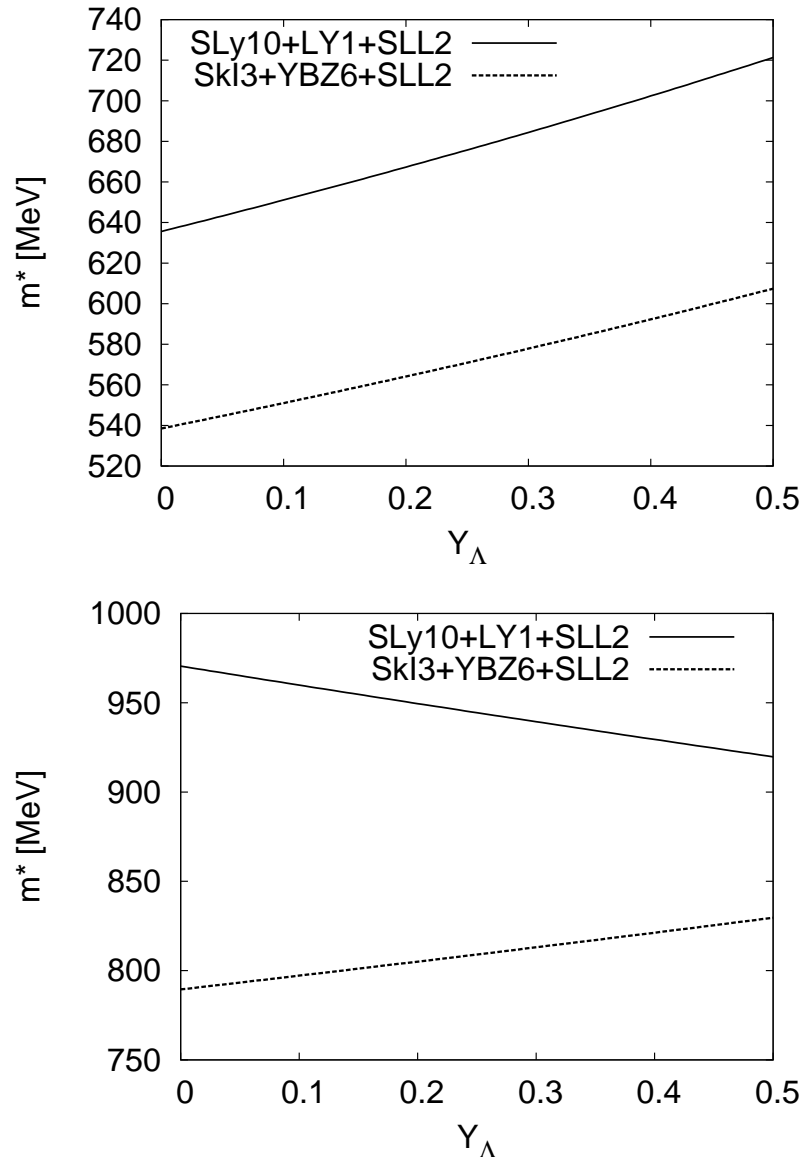
Figure 6.2: The effective mass of the nucleons (upper panel) and Λ hyperons (lower panel) in hypernuclear matter at nuclear saturation density as a function of the strangeness fraction $Y_\Lambda = \frac{\rho_\Lambda}{\rho}$.
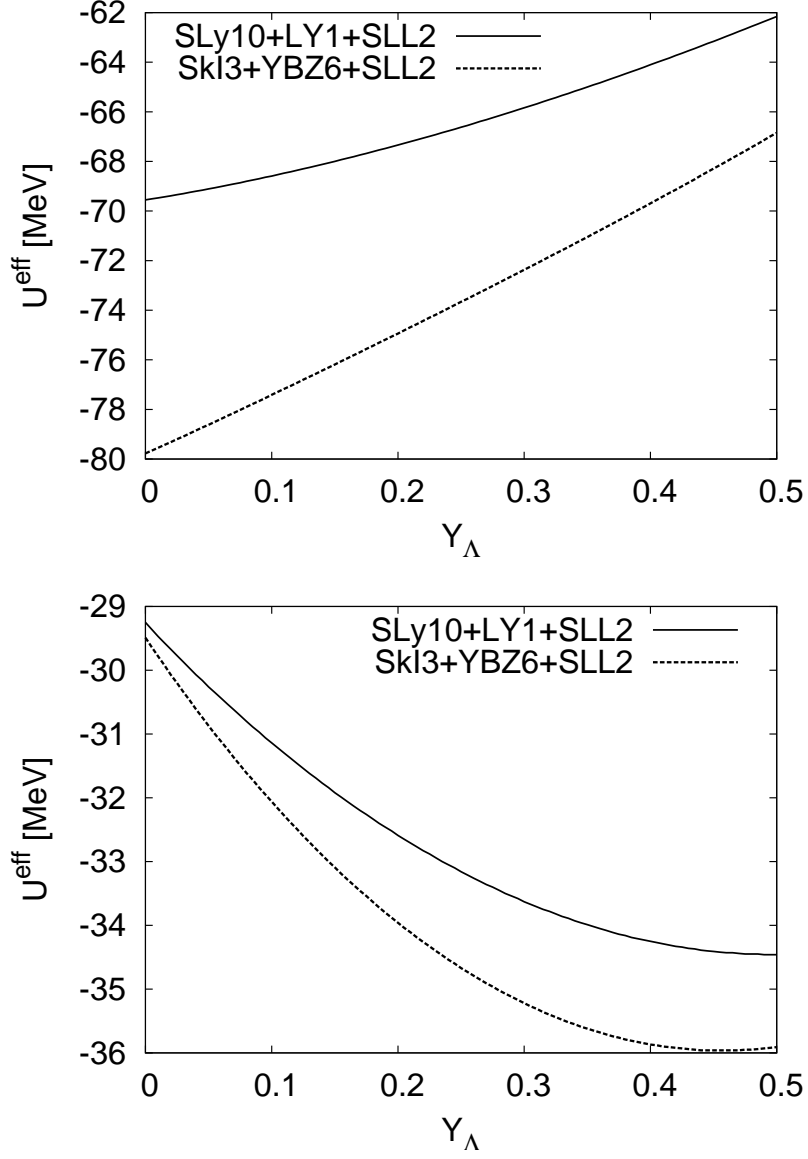
Figure 6.3: The effective potential of the nucleons (upper panel) and Λ hyperons (lower panel) in hypernuclear matter at nuclear saturation density as a function of the strangeness fraction $Y_\Lambda = \frac{\rho_\Lambda}{\rho}$.

6.2 The Short-Range Interaction

According to our discussion in chapter 4 the ΛN and the NN interaction can be written down as

$$V^{N\Lambda} = f^{N\Lambda} + g'^{N\Lambda}\vec{\sigma_1}\vec{\sigma_2} \tag{6.12}$$

and

$$V^{\Lambda\Lambda} = f^{\Lambda\Lambda} + g'^{\Lambda\Lambda}\vec{\sigma_1}\vec{\sigma_2}, \tag{6.13}$$

respectively. The Landau parameters $f^{N\Lambda}$, $g'^{N\Lambda}$, $f^{\Lambda\Lambda}$ and $g'^{\Lambda\Lambda}$ are given by the second variation with respect to the partial spin-flavor densities from the energy density functional $E(\rho_{p\uparrow}, \rho_{p\downarrow}, \rho_{n\uparrow}, \rho_{n\downarrow}, \rho_{\Lambda\uparrow}, \rho_{\Lambda\downarrow})$ [Mor05]. Since the Λ-hyperons do not couple to the pions, we do not need to subtract the pion contribution and can directly average over the weighted spin degrees of freedom to obtain the corresponding interaction matrix elements

$$\mathcal{M}_{N\Lambda} = \frac{1}{2}\sqrt{(f^s_{N\Lambda})^2 + 3(g^s_{N\Lambda})^2} \tag{6.14}$$

and

$$\mathcal{M}_{\Lambda\Lambda} = \frac{1}{2}\sqrt{(f^s_{\Lambda\Lambda})^2 + 3(g^s_{\Lambda\Lambda})^2}. \tag{6.15}$$

In Fig. 6.4 results for the NN interaction matrix element in hypernuclear matter are shown. The results are presented as a function of the strangeness fraction $Y_\Lambda = \rho_\Lambda/\rho$ at nuclear matter saturation density. We extracted the NN interaction matrix element from the SLy10 Skyrme energy density functional. Even though this is not fully consistent with the later use of ΛN [LY97] and $\Lambda\Lambda$ [Lan98] energy density functional. The values given by Lanskoy and Yamato assumed that the nucleon sector is parameterized with the SkM* or SIII interactions. However, Mornas [Mor05] preferred the set SLy10+LYI+SLL2 and SkI3+YBZ6+SLL2 for his calculation of the transition to a ferromagnetic state in neutron stars. At this point we refer to the discussion of the particle fraction in β-equilibrated nuclear matter in section 6.4. As we mentioned before, we adopted the notation from [Mor05] and name the parameter sets for the ΛN Skyrme energy density functional I-IV from [LY97] LYI-LYIV, the parameter sets 1-6 from [YBZ88] YBZ1-6 and the parameter sets for $\Lambda\Lambda$ Skyrme energy functional in [Lan98] SLL1-3. The number of protons and neutrons are again assumed to be equal. Fig. 6.4 shows that with rising number of Λ-hyperons, the NN interaction matrix elements $\mathcal{M}_{nn}$ and $\mathcal{M}_{np}$ increase. This result is not surprising,
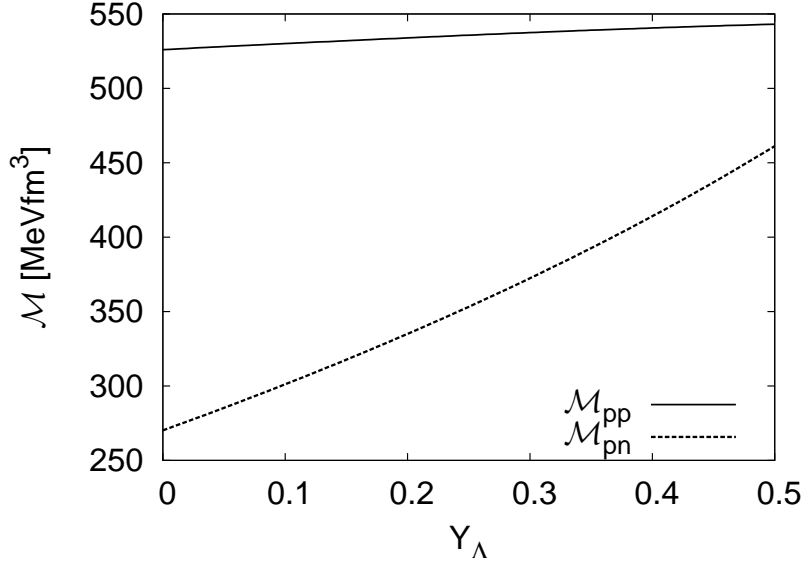
Figure 6.4: The nucleon interaction matrix element at nuclear matter saturation density $\rho = 0.16$ fm^{-3} as a function of the strangeness fraction Y_Λ using the SLy10 Skyrme parameter set.

since the strangeness fraction enters by decreasing the number of nucleon with increasing number of Λ-hyperons. As seen in Fig. 4.5, the decrease of the number of nucleons leads to a higher interaction NN matrix element.

The ΛN and the $\Lambda\Lambda$ interaction matrix elements at nuclear matter saturation density as a function of the strangeness fraction Y_Λ are shown in Fig. 6.5 and Fig. 6.6 respectively. In the naive quark picture, using SU(3) arguments, the Λ-N and $\Lambda\Lambda$ interaction strength should evolve according to the ratio of strange to non-strange quarks in the baryons. This would predict a value of 2/3 for the Λ-N and 1/3 for the $\Lambda\Lambda$ interaction vertex. However, naive quark counting models can not explain all experimental facts, such as the decrease of the spin-orbit splitting in Λ nuclei. Therefore, it is is not surprising that our results differ from the naive quark counting. Comparing the ΛN interaction matrix element in Fig. 6.5 with the NN interaction matrix element in Fig. 6.4 shows that the reduction of the interaction strength, depending on the parameter set taken, is between $8 - 17\%$ for the parameter sets LYI-LYIV (upper panel) and even lower for the parameter sets YBZ1, YBZ5, YBZ6 (lower panel). Keil et al. [KHL00] determined values around 50% for the meson reduction factor for their density dependent hadron field theory model. While the coupling of the Λ-N interaction seems to be underestimated, the $\Lambda\Lambda$ interaction seems to be overestimated, see Fig. 6.6, and is larger than the Λ-N interaction. Especially this strong overestimation of the $\Lambda\Lambda$ interaction matrix element reflects
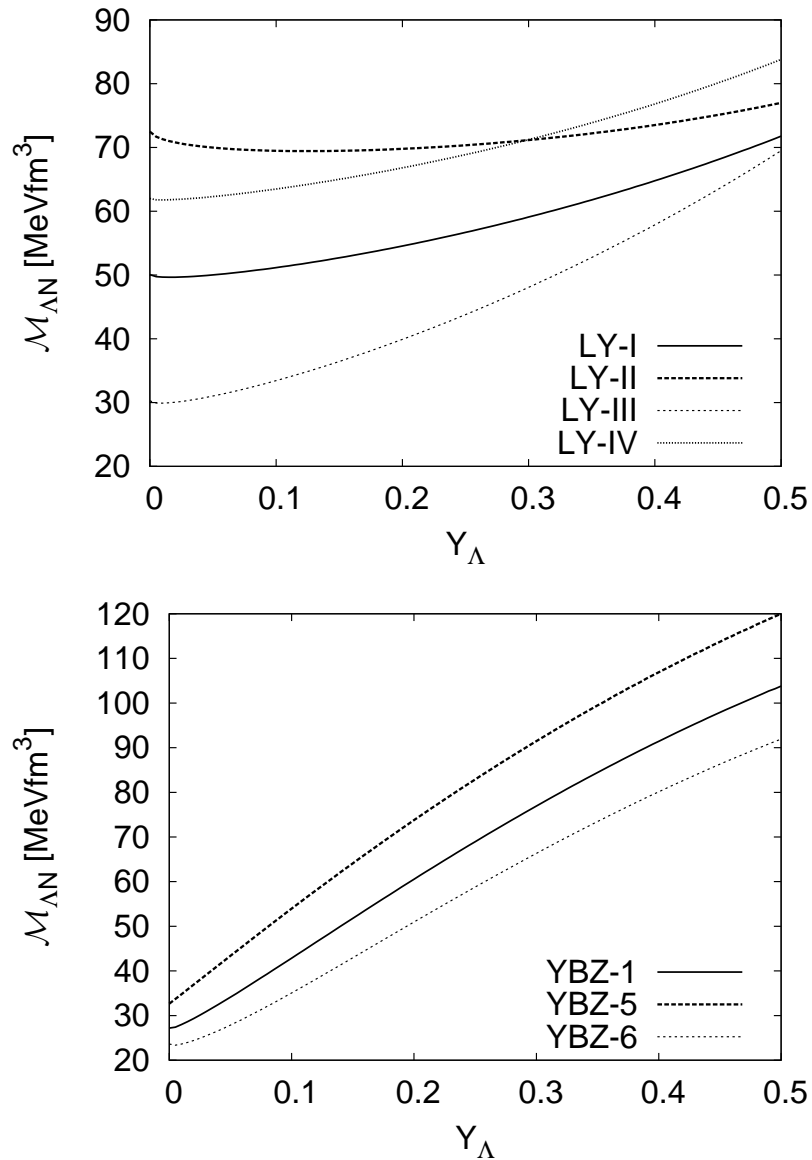
Figure 6.5: The ΛN interaction matrix element at nuclear matter saturation density $\rho = 0.16$ fm^{-3} as a function of the strangeness fraction Y_Λ using the Skyrme parameters sets from [LY97] (upper panel) and [YBZ88] (lower pnael).
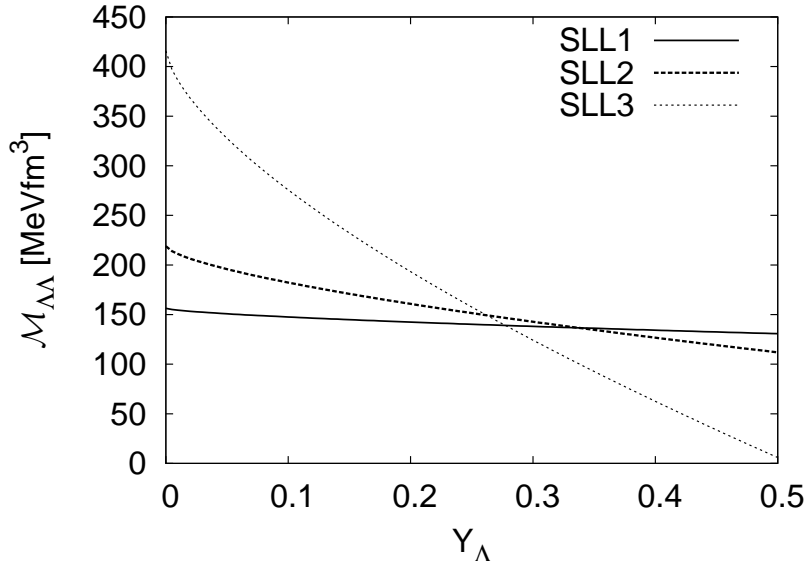
Figure 6.6: The $\Lambda\Lambda$ interaction matrix element at nuclear matter saturation density $\rho = 0.16$ fm^{-3} as a function of the strangeness fraction Y_Λ using the Skyrme parameters sets from [Lan98].

the the limited amount of experimental data for interaction of the Λ-hyperon in the medium. The only experimental information on the $\Lambda\Lambda$ interaction is limited to the ground states of the double-Λ hypernuclei. On theoretical site soft-core hyperon-nucleon potentials [RSY99] give information on the free interactions. But so far not much is known about the hyperon interactions in the medium.

6.3 Dynamical Self-Energies in Hypernuclear Matter

The influence of strangeness to the nuclear medium are best observed when keeping the total baryon density constant by varying only the strangeness fraction $Y_\Lambda = \rho_\Lambda/\rho$. Since we use different Skyrme parameterizations, we a look at the differences between the different parameterizations. For the following considerations we investigate dynamical correlations in a medium with variable strangeness content on top of a background of symmetric proton-neutron matter. Hence, the total density is $\rho = \rho_n + \rho_p + \rho_\Lambda$ with $\rho_n = \rho_p = \rho_N$ and $\rho_\Lambda = \rho - 2\rho_N$. The self-consistency affects all parts of the self-energies of all baryons. Therefore, the self-energies of the nucleons will also be change in the presence of Λ-hyperons and it is not enough to treat the nucleons and the strange sector independently.
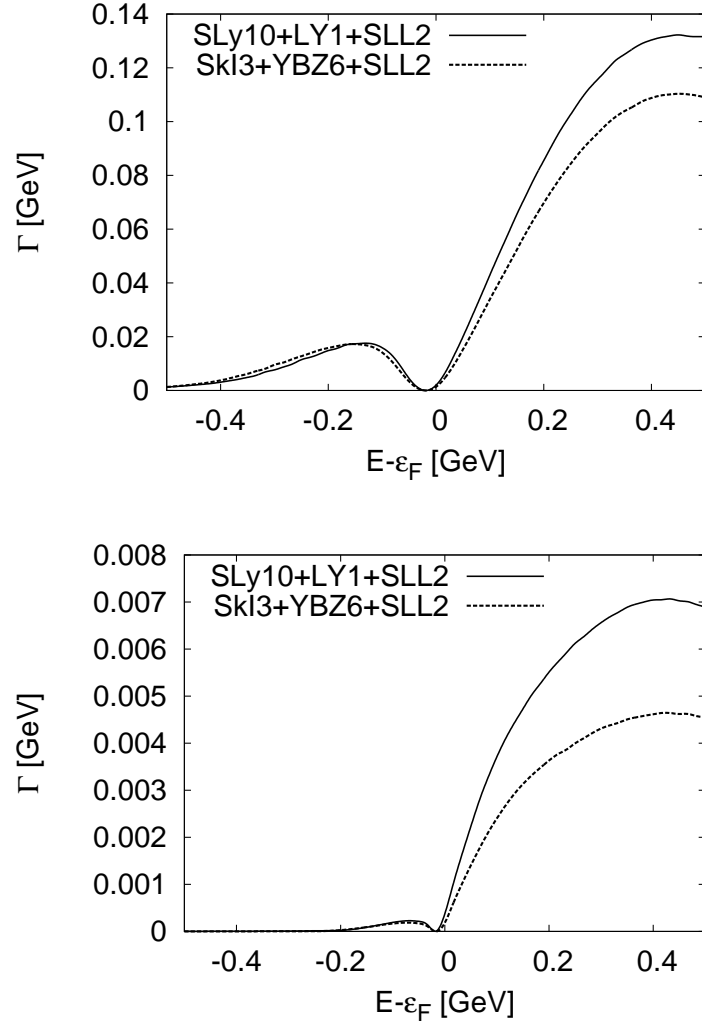
Figure 6.7: Comparison for the width of nucleons (upper panel) and the Λ-hyperon (lower panel) SLy10+LYI+SLL2 and SkI3+YBZ6+SLL2 for momentum $q = 0.3$ GeV/c at saturation point density. The strangeness fraction is assumed to be $Y_\Lambda = 0.1$ by keeping the number of protons equal to the number of neutrons.

In Fig. 6.7 results for the width of nucleons and Λ-hyperons in hypernuclear matter are shown using SLy10+LYI+SLL2 and SkI3+YBZ6+SLL2 Skyrme parameterization. The results are shown for $Y_\Lambda = 0.1$ at saturation density and a momentum $q = 0.3$ GeV/c. The Results for the nucleons are shown in the upper panel and for the Λ-hyperons are shown in the lower panel. In principle we see that the results resemble those in nuclear matter. Except that the Λ hyperons couple less strong to the other particles which leads to an decrease of the width. Comparing the widths shows that the width for nucleons is about 10 times larger as the width for the Λ-hyperons. This result is not surprising, since the imaginary part of the self-energy in our approach scales with the interaction matrix element and we found that the interaction matrix element for the Λ-hyperons the is around 10 times smaller than for the nucleons. For the different Skyrme parameterizations we observe slight differences in the high energy region. These differences mainly caused by the uncertainties of the ΛN interaction. We have shown in chapter 4 that the YBZ6 Skyrme parameterization leads to a smaller matrix element for the ΛN interaction than using the LYI Skyrme parameterization. This fact is directly reflected in the lower panel of Fig. 6.8, where we observe a lower width for the SkI3+YBZ6+SLL2 parameterization than for the SLy10+LYI+SLL2 parameterization.

The weak coupling of the Λ-hyperons can also be seen very clearly in the spectral function and the momentum distribution. In Fig. 6.8 the spectral function of nucleons and Λ-hyperons are shown using the SLy10+LYI+SLL2 (upper panel) and SkI3+YBZ6+SLL2 (lower panel). The results are shown for a momentum $q = 0.3$ GeV/c, a strangeness fraction $Y_\Lambda = 0.1$ and at saturation density $\rho = 0.16$ fm^{-3}. One clearly sees the quasiparticle peaks for nucleons and Λ-hyperons above the Fermi energy. The nucleon spectral function resembles in principle the feature already seen in nuclear matter, while the spectral function of the Λ-hyperons shows a sharper structure. This observation agrees perfectly well with the sharp spectral structure seen in hypernuclear spectra e.g. [Hot01]. The momentum distribution of nucleons and Λ-hyperons is shown in Fig. 6.9 for a strangeness fraction $Y_\Lambda = 0.1$. For both particles we observe a high energy tail and a depletion of the Fermi sea. Due to the weaker coupling, we observe that less states are shifted from the Fermi sea to higher momentum for the Λ-hyperons and the high momentum tail is less pronounced.

In Fig. 6.10 we compare results for different strangeness fractions for nucleons and Λ-hyperons in the upper and lower panel, respectively. We observe that the width below the Fermi-energy directly scales with the number of particles for nucleons and Λ-hyperons, since with rising strangeness fraction, the width decreases for the nucleons and rises for the Λ-hyperons. The width below the Fermi energy is given by the one-particle-two-hole (1p2h) self-energy $\Sigma^<$, which scales with the particle number [KB62]. For energies $E > \epsilon_F$ the width is, except for a small variation at very high energies, constant for the nucleons, while the Λ-hyperons saturate at a high strangeness fraction.
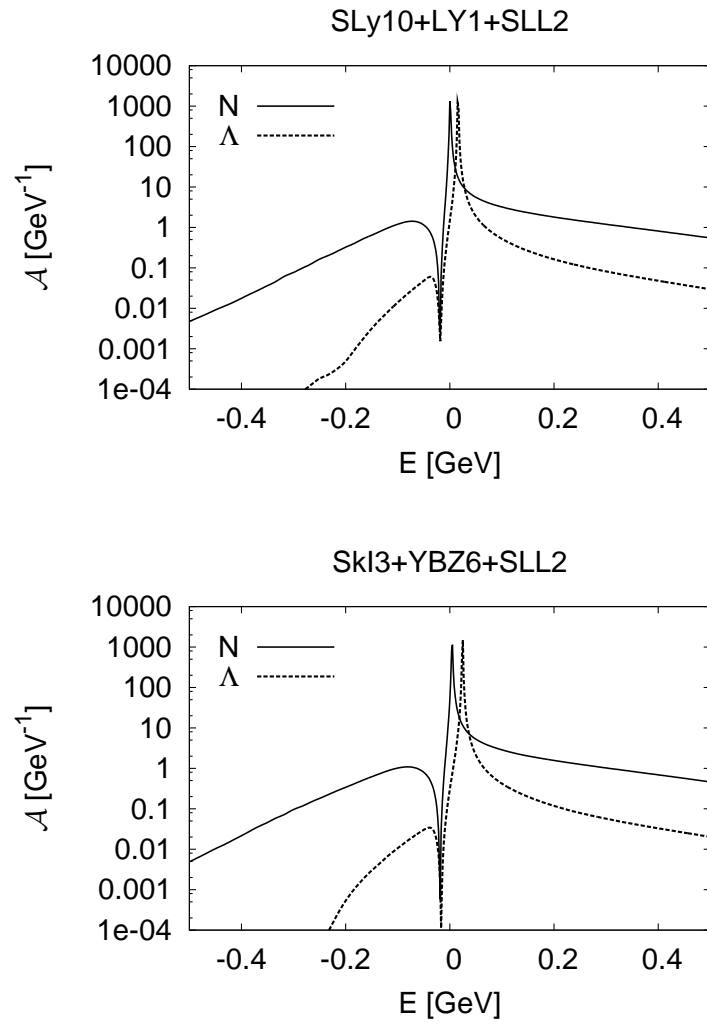
Figure 6.8: The spectral function of nucleons and Λ-hyperons in hypernuclear matter with strangeness fraction $Y_\Lambda = 0.1$ at saturation point density.
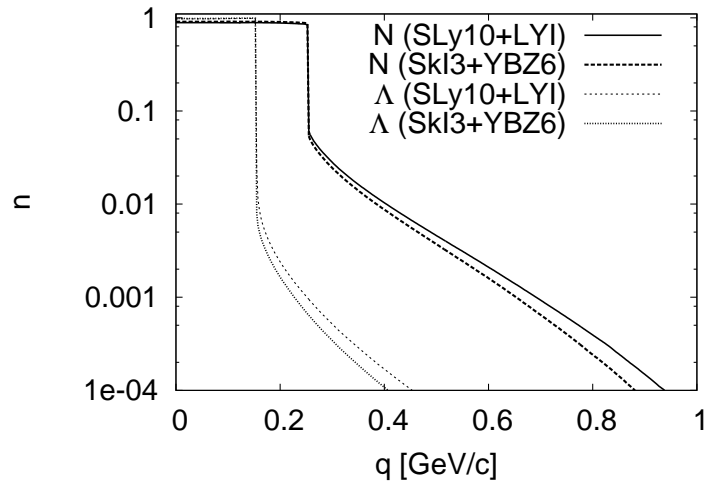
Figure 6.9: The momentum distribution of nucleons and Λ-hyperons in hypernuclear matter with strangeness fraction $Y_\Lambda = 0.1$ at saturation point density.
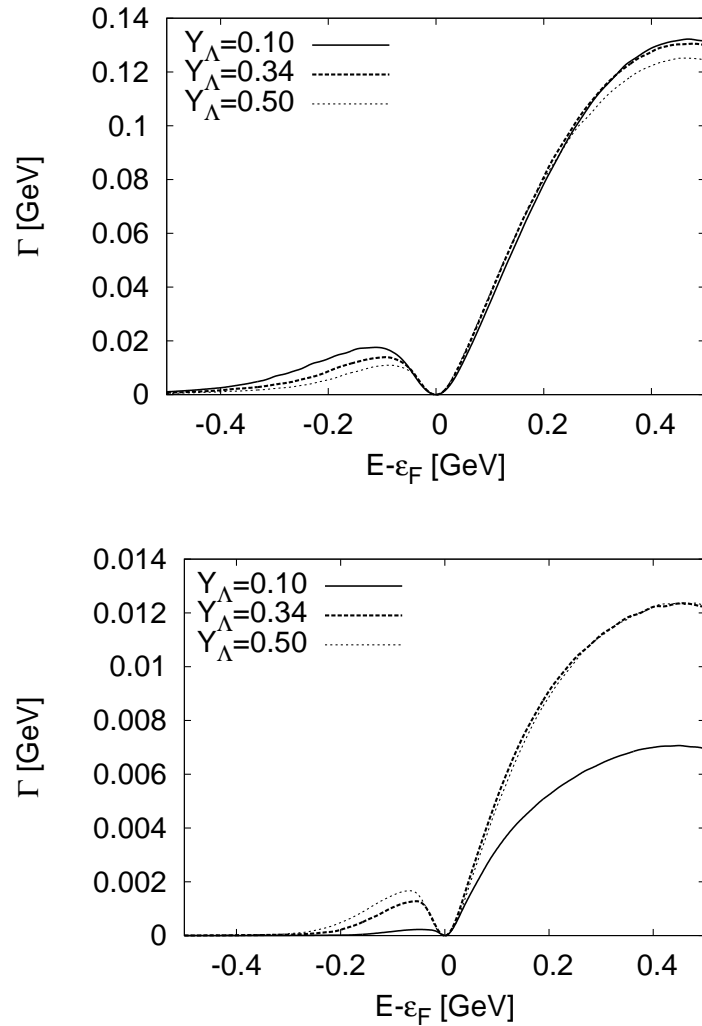
Figure 6.10: Results for width of the nucleons (upper panel) and Λ-hyperons (lower panel) at momentum $q = 0.3$ GeV/c for different strangeness fractions at saturation point density. The results are obtained using the SLy10+LYI+SLL2 parameter set.

6.4 Hypernuclear Matter in β-Equilibrium

6.4.1 The Particle Fractions

β-equilibrated nuclear matter is a medium containing hadrons and leptons, coupled by the weak interaction. Restricting the investigations to $np\Lambda$-matter, all processes are allowed which conserve charge and baryon number. These processes can be used to fix the particle fractions. In $np\Lambda$ matter the particles are subject to the processes

$$p + e^- \longleftrightarrow n + \nu_e \tag{6.16}$$

$$p + e^- \longleftrightarrow \Lambda + \nu_e \tag{6.17}$$

From the equilibrium conditions we can determine the chemical potentials by

$$\mu_p + m_p + \mu_e = \mu_n + m_n + \mu_\nu, \tag{6.18}$$

$$\mu_p + m_p + \mu_e = \mu_\Lambda + m_\Lambda + \mu_\nu. \tag{6.19}$$

We note that the electron is relativistic so that the chemical potential is given by the expression $\mu_e = \sqrt{k_{fe}^2 + m_e^2}$. Eq. (6.18) and Eq. (6.19) are solved imposing electric charge conservation $n_e = n_p$. Furthermore, we assume that the neutrinos are not trapped but leave instantly, implying $\mu_\nu = 0$. This assumption is true in cold neutron star matter. We note that in this simple model the other hyperons and the muons are missing. The muons appear around the saturation density and their effect is not very important in the present case, where we neglected the Σ^--hyperons (see [Mor05] for details). Mornas estimated the error by using models of Balberg et al. [BG97] and Bandyopadhyay [BB00]. Mornas also calculated the properties of neutron stars formed by hypernuclear matter using the Tolman-Oppenheimer-Volkoff (TOV) equation. The SLy10+LYI+SLL2 and the SkI3+YBZ6+SLL2 parameterization were found to describe the hypernuclear mater in β-equilibrium the best. These sets mainly describe the features observed in microscopic models such as Brueckner-Hartree-Fock or relativistic mean-field calculations, not only qualitatively but also quantitatively. Results from [Mor05] solving the TOV equation are given in table 6.3. The chosen parameter sets reach masses for the neutron stars greater than 1.4 times the mass of the sun and the central density reached with the maximum mass is slightly larger than the density at which the velocity of sound reaches the velocity of light, so causality is not violated. Therefore we will use the SLy10+LYI+SLL2 and SkI3+YBZ6+SLL2 parameter sets as a model for hypernuclear matter in β-equilibrium.

Fig. 6.11 shows the results for the particle fractions when solving Eq. (6.18) and Eq. (6.19). The particle fraction in β-equilibriated hypernuclear matter is a complicated cut through the phase diagram of pure $pn\Lambda$-matter; the path is defined

parameter set	SLy10+LYI+SLL2	SkI3+YBZ6+SLL2
$\rho_S(c_s^2 = c^2)$	$16.032\rho_0$	$13.077\rho_0$
$\rho_C(1.4M_\odot)$	$9.39\rho_0$	$2.39\rho_0$
R(1.4 $M_\odot$)	9.0 km	13.19 km
ρ_{max}	$12.38\rho_0$	$6.79\rho_0$
M_{max}	$1.425M_{sun}$	$1.642M_{sun}$
R(M_{max})	8.11 km	11.02 km

Table 6.3: Results taken from [Mor05] for neutron star matter. $\rho_S(c_s^2 = c^2)$ denotes the density when the velocity of sound reaches the velocity of light and $\rho_C(1.4M_{sun})$ the central density of neutron star with 1.4 times the mass of the sun. The density of the saturation point in nuclear matter is given by ρ_0.

by the equilibrium conditions. The results are obtained using SLy10+LYI+SLL2 and SkI3+YBZ6+SLL2. It can bee seen that the hyperons appear at about 2.7 times saturation density for the SLy10+LYI+SLL2 and around two times saturation density for SkI3+YBZ6+SLL2 and the hyperons are less abundant for the SLy10+LYI+SLL2 than for the SkI3+YBZ6+SLL2 parameter set. This fact can be understood, if remind that using the SkI3 Skyrme parameterization leads to a stiffer equation of state than using the SLy10 Skyrme parameterization (see chapter 3). A stiffer equation of state reaches the required energy for hyperon formation at lower densities. For the SLy10+LYI+SLL2 parameter set we have a high excess of neutrons up to three times saturation density, while the fraction of the neutrons is dropping fast for densities higher than the saturation density using the SkI3+YBZ6+SLL2.

6.4.2 The Width and the Spectral Function

The spectral functions in β-equilibrated hypernuclear matter resemble in principle the features of the spectral function in hypernuclear matter with a certain strangeness fraction. In Fig. 6.12 the spectral functions for protons, neutrons and Λ-hyperons are shown. The upper panel shows the SLy10+LY1+SLL2 Skyrme results at density ρ=0.48 fm^{-3} and the lower panel the results using the SkI3+YBZ6+SLL2 Skyrme parameterization at density ρ=0.40 fm^{-3}. The chosen densities are just at or slightly above the threshold densities for hyperon formation. One clearly sees the quasiparticle peaks of particles at different positions and all spectral function show a wide spectral distribution. All particles carry the momentum $q = 0.3$. The quasiparticle peak for the neutrons is still located in the Fermi sea, while the protons and Λ-hyperons can be found above the Fermi edge.
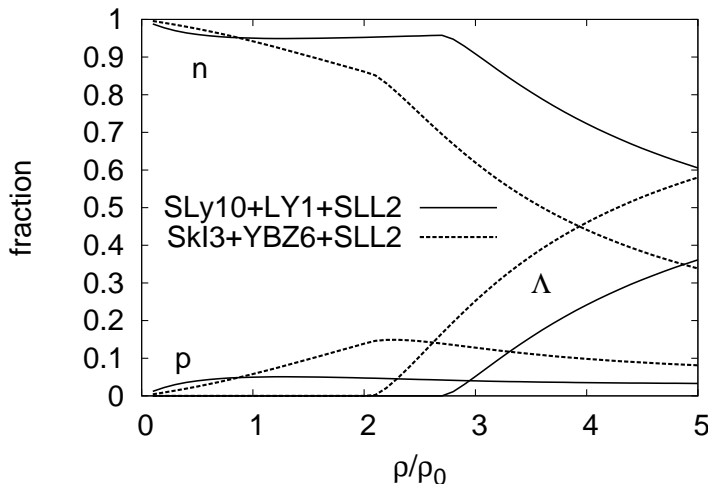
Figure 6.11: The particle fractions in β-equilibrium reproduced from [Mor05].

However, we see differences to hypernuclear matter with a fixed strangeness fraction when we examine the width. In Fig. 6.13, Fig. 6.14 and Fig. 6.15 results for protons, neutrons and Λ-hyperons in β-equilibrated hypernuclear matter at $\rho = 0.48$ fm^{-3} are shown, respectively. The particles carry the momentum $q = 0.3$ GeV/c. Results are shown for the SLy10+LY1+SLL2 and SkI3+YBZ6+SLL2 Skyrme parameterizations. Comparing the results for protons in β-equilibrated hypernuclear matter to the results in (asymmetric) nuclear matter (see Fig. 5.2), shows that the protons resemble the global energy behavior qualitatively and also quantitatively with small variations. The differences of the SLy10+LY1+SLL2 and the SkI3+YBZ6+SLL2 Skyrme parameterizations can be explained by the different fractions of protons in β-equilibrated hypernuclear matter using the different parameterizations (see Fig. 6.11). For a density $\rho = 0.48$ fm^{-3} the SLy10+LY1+SLL2 parameterization predicts less protons than the SkI3+YBZ6+SLL2 parameterizations, which is connected to the higher symmetry energy coefficient of the SkI3 Skyrme parameterization (see Fig. 3.7). Hence, the width for the protons is lower for the SLy10+LY1+SLL2 since the one-particle-two-hole (1p2h) self-energy scales with the number of particles [KB62].

For neutrons the results of the width seem to be surprising since we find a suppression for the densities shown here. Comparing the results for protons, neutrons and Λ-hyperons shows that the neutron width is of the same size as the width for Λ-hyperons rather than the width for the protons. Also, there are differences between the two models at the quantitative level, the particle width for the neutrons and the Λ-hyperons are both smaller, when using the SLy10+LY1+SLL2 than the
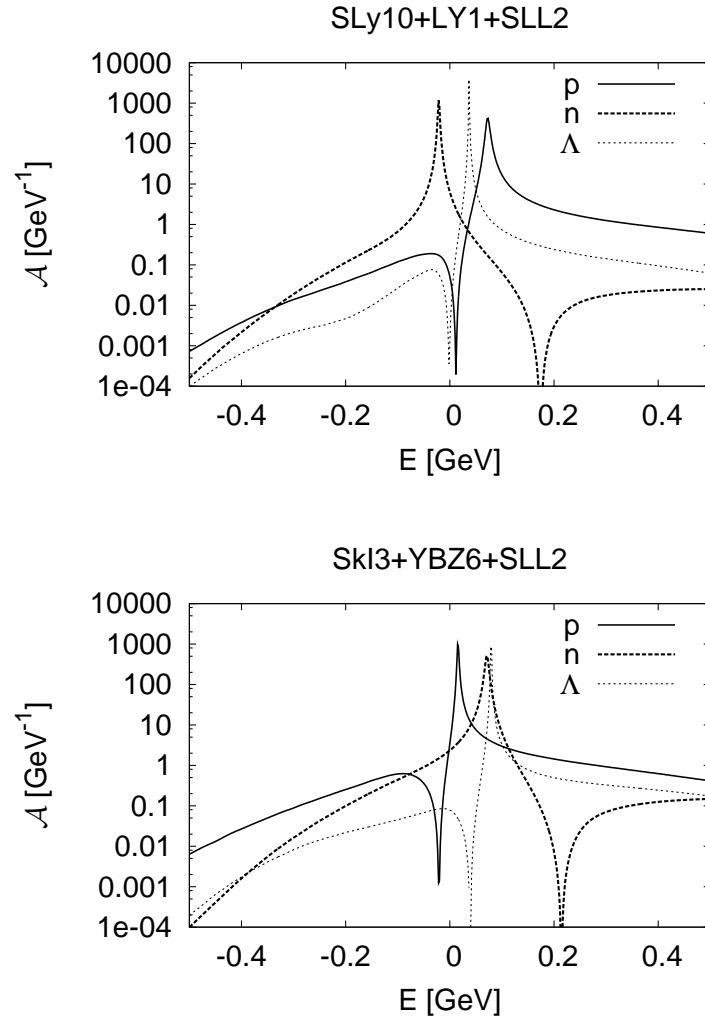
Figure 6.12: The spectral function for proton, neutrons and Λ-hyperons with a momentum $q = 0.3$ GeV/c in β-equilibrated hypernuclear. The upper panel shows results using the SLy10+LY1+SLL2 Skyrme parameterization at density a $\rho = 0.48$ fm^{-3} and the lower panel results using the SkI3+YBZ6+SLL2 Skyrme parameterization at density $\rho = 0.40$ fm^{-3}.

SkI3+YBZ6+SLL2 Skyrme parameterization. The suppression of the neutron width can be explained by the high excess of neutrons in β-equilibrated hypernuclear matter. Due to the high neutron number, many states are Pauli blocked. This effect is comparable to the saturation for nuclear matter at high densities seen by Frömel et al. [FLM03]. Since the two models predict different fractions of particles, the differences of the two models can also be explained by the higher excess of neutrons for SLy10+LY1+SLL2 at $\rho = 0.48$ fm^{-3} and Pauli blocking.
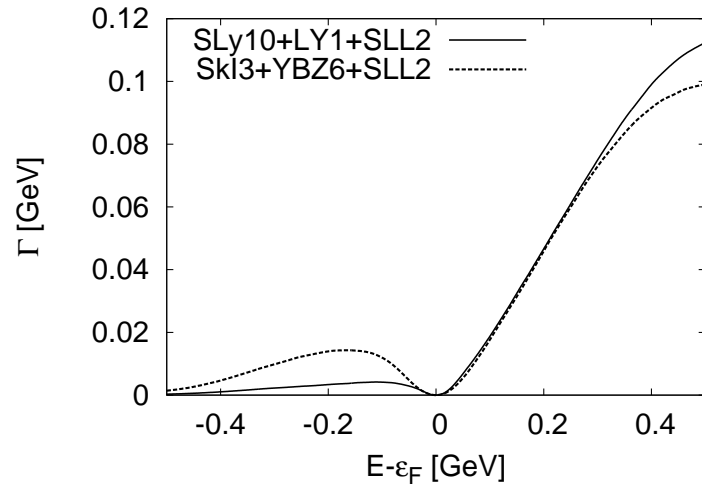
Figure 6.13: The width for protons in β-equilibrated hypernuclear matter at the $\rho = 0.48$ fm^{-3}. The momentum of the protons is $q = 0.3$ GeV/c
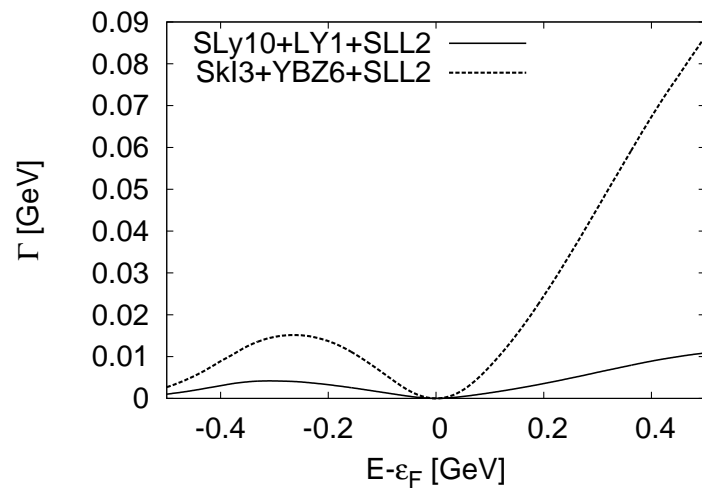
Figure 6.14: The width for neutrons in β-equilibrated hypernuclear matter at the $\rho = 0.48$ fm^{-3}. The momentum of the neutrons is $q = 0.3$ GeV/c
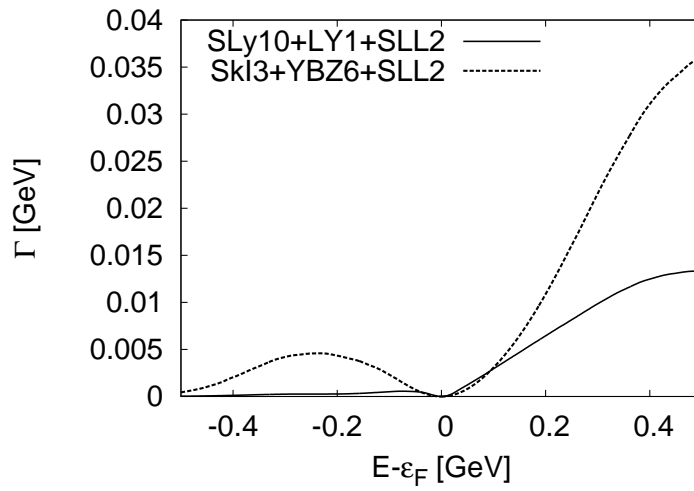
Figure 6.15: The width for Λ-hyperons in β-equilibrated hypernuclear matter at the $\rho = 0.48$ fm^{-3}. The momentum of the Λ-hyperons is $q = 0.3$ GeV/c

6.4.3 The Quasiparticle Strength

Since the quasiparticle strength provides a good measure for particle correlations, we now compare it for the SLy10+LYI+SLL2 and SkI3+YBZ6+SLL2 Skyrme parameter set. In β-equilibrated hypernuclear matter the features of the quasiparticle strength in nuclear matter are recovered and the quasiparticle strength deviates from unity only close to the Fermi edge, where it shows a minimum. The quasiparticle strength for protons, neutrons and Λ-hyperons at the Fermi edge are shown in Fig. 6.16 for the SLy10+LYI+SLL2 and the SkI3+YBZ6+SLL2 Skyrme parameterization in the upper and lower panel, respectively.

The proton quasiparticle strength shows an increase for SLy10+LYI+SLL2 parameter set in the low density region. For densities higher than 0.2 fm³ it is slightly decreasing and stays constant for densities above 0.4 fm³. For the SkI3+YBZ6+SLL2 parameterization the proton quasiparticle strength shows a slight decrease before staying constant above 0.4 fm³. For the neutrons we have for both parameterizations an increase of the quasiparticle strength before decreasing. Finally, the quasi-particle strength of Λ-hyperons is equal to unity before the threshold of Λ-hyperons formation. After the threshold is reached, the Λ quasiparticle strength differs slightly from unity.

Since the quasiparticle strength is inverse proportional to the number of correlations, we can interprete this results by the interplay between the number of particles and Pauli-blocking in β-equilibrated nuclear matter, which we can clearly see for the quasiparticle strength of neutrons obtained using the SkI3+YBZ6+SLL2. In the lower panel of Fig. 6.16 we see that the correlations for low energies is decreasing, i.e. the quasiparticle strength is increasing. This is realted to the high abundance of neutrons in Fig. 6.11, with higher density more states are Pauli blocked. But as we also see in Fig. 6.11, decreases the fraction of neutrons with increasing density and we see an increase of the neutrons correlations, i.e. the quasiparticle strength is decreasing, in the lower panel of Fig. 6.16. In the same manner the results for the protons and the Λ-hyperons can be interpreted.

Because of the weak coupling of the Λ-hyperons, the dependence of the correlations on the number of particles is not as strong as for the nucleons and the quasiparticle strength does not deviate much from unity. However, in summary we conclude that correlations in our approach are connected rather directley to the abundance of the particles and the available phase space e.g. constrained by Pauli blocking.
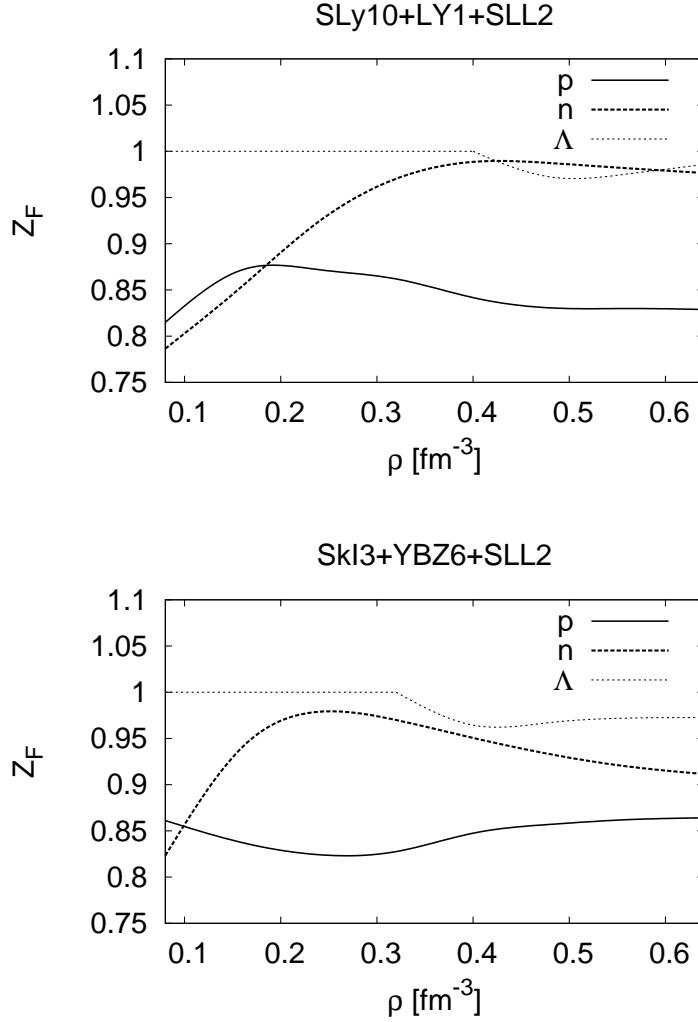
Figure 6.16: The quasiparticle strength for $q = q_F$ of protons, neutrons and Λ-hyperons in β-equilibrated hypernuclear matter as a function of the baryon density. The upper panel shows the results of the SLy10+LY1+SLL2 Skyrme parameterization and the lower for the SkI3+YBZ6+SLL2 parameterization.

7 Summary

In this work we examined dynamical correlations in infinite nuclear and hypernuclear matter. We used a self-consistent approach to calculate the dynamical self-energy and the spectral function. The self-energy is approximated by the one-particle-two-hole (1p2h) and two-particle-one-hole (2p1h) polarization self-energy by neglecting higher order terms. For a realistic treatment of the nuclear mean-field incorporating an accurate description of finite nuclei, we used modern Skyrme parameterizations for the energy density functional. As shown by [LEL$^+$00, LLLM02], dynamical correlations are more influenced by the strength of the interaction and the available phase space rather by the details of the interaction. Therefore, we assumed an energy- and momentum-independent interaction matrix element to approximate the polarization self-energies.

A general introduction to the Green's function method and their impact to the many-body problem was given in chapter 2. After the basic definitions of the Green's function and its connection to the spectral function, we showed how to expand the Green's function in terms of the interaction and introduced the self-energy. Further, we discussed the contributions to the self-energy. Finally, we showed how the spectral function can be calculated from the self-energy.

In chapter 3 we gave an introduction to the Skyrme parameterization and showed results using different Skyrme parameterizations. Comparing the SLy10, SkI3 and the SkM* Skyrme parameter sets, shows that all parameter sets reproduce the properties of infinite nuclear matter, such as the saturation point density, the binding energy, the incompressibility coefficient and the asymmetry coefficient, very well. Also, the qualitative behavior of the equation of state is in good agreement except for variations in the high density region for all Skyrme parameterizations. The SLy10 parameterization shows also a good agreement for the equation of state with results from the Urbana group [APR98] for symmetric nuclear and pure neutron matter. Qualitatively, also the effective potential for all Skyrme parameterizations agrees well, while the picture for the effective mass is different. Increasing strangeness fraction the SLy10 and the SkI3 parameterizations shows a decrease of the proton effective mass, while the neutron effective mass increases. For the SkM* parameterization the situation is reversed, here, the proton effective mass is increasing with increasing strangeness fraction and the neutron effective mass is decreasing. Unfortunately, so far almost nothing is experimentally known about the effective mass in

neutron rich matter.

We examined the short-range interaction in chapter 4. To get information of the interaction matrix elements, we used Fermi liquid theory and extracted the Landau-Migdal parameters from the Skyrme energy-density functional. An average interaction matrix was obtained by a weighted sum of the Landau-Migdal parameters over the spin degrees of freedom. To account only for the short-rang part of the nucleon-nucleon interaction, we identified the long-range contribution with pion exchange. Therefore, we calculated the Landau-Migdal parameters for the pion exchange contribution and subtracted it from the Landau-Migdal parameters obtained from the Skyrme parameterization. The subtraction of the pion contribution leads to an increase of the nucleon-nucleon interaction matrix elements. A comparison for the nucleon-nucleon matrix element obtained with the SLy10, SkI3 and SkM* Skyrme parameterization showed a good agreement with slight differences of the strength for all parameterizations. Qualitatively, the interaction matrix element decreases with increasing density. This fact can be explained by increase of the Pauli blocked states at higher densities.

At the beginning of chapter 5 we discussed the numerical and mathematical details of our approach. Thereafter, we showed results for the width, the spectral function, the momentum distribution and the quasi-particle strength in symmetric and neutron rich infinite nuclear matter using different Skyrme parameterizations. The comparison of the results for the width obtained with the SLy10, SkI3 and the SkM* Skyrme parameter sets shows that they are in good agreement. All parameter sets resemble the overall energy behavior of the particle width, known from many-body calculations. Differences of the parameter sets are seen in the high energy region. They are caused by the differences of the interaction strength when using different Skyrme parameter sets. In neutron rich matter the results for the different Skyrme parameter sets show similar deviations. However, the differences for protons seem to be less pronounced than for neutrons. A comparison of our results for the SLy10 parameterization with a recent Brueckner-Hartree-Fock (BHF) calculation of Hassaneen al. [HM04] showed a good agreement on a qualitative level. Quantitatively, there are differences when comparing the results of the two calculations, but using different nucleon-nucleon potential in the BHF calculation leads also to differences in the obtained results. Also, the spectral function shows a behavior known from other many-body calculations, a sharp quasi-particle peak with a wide spectral distribution. The location of the quasi-particle peak is mainly given by the mean-field contribution of the self-energy, while the collisional part is responsible for the spectral distribution. The comparison of different Skyrme parameterizations shows that the results for the different parameterization agree very well in symmetric and asymmetric nuclear matter.

The momentum distribution of the nucleons in symmetric nuclear matter shows

a reduction of the occupancy inside the Fermi sea and this fraction is shifted to higher momenta. This observation is well known from many-body theory [DVN05]. When we use a pion subtracted interaction matrix element, our results show good agreement with the results of full many-body calculations. While the results, where we did not subtract the pion contribution put less strength in the high momentum states. We conclude that subtracting the pion contribution from the interaction is essential for our approach, making contact to a full-scale many-body calculation.

Hassaneen et al. [HM04] observed less depletion of the Fermi sea in the momentum distribution for neutrons than for that of the protons in neutron rich matter. They claimed that this observation can be explained by an additional tensor interaction. In our approach we are, however, able to describe this feature without a explicit use of a tensor interaction.

Finally, we introduced the quasi-particle strength, which tells us how many states are still left in the quasi-particle state and not shifted into many-body configurations. The obtained results for the quasi-particle strength seems to confirm the assumption of our approach, since we observe that the quasi-particle strength is much different from unity only close to the Fermi edge. This means that the many-body system is only strong correlated close to the Fermi edge. This observation seems to confirm our assumption of a local interaction at the Fermi-edge, as which the Landau-Migdal parameters can be seen. Compared to the results of [Leh03] and [BFF92], our calculations show a good qualitative agreement, while at the quantitative level our results show slightly less reduction of the quasi-particle strength than the results of [BFF92]. In asymmetric nuclear matter we observe less correlations for neutrons than for protons. This fact is directly related to our observation of the momentum distribution in asymmetric nuclear matter, where the neutrons show less depletion in the Fermi sea than the protons. For completeness, it is worthwhile to mention that in finite nuclei the local width of particle states above the threshold includes additional contributions from the decay into the (A-1)+N-continuum with an asymptotically escaping nucleon.

In chapter 6 we examined dynamical correlations in hypernuclear matter and in nuclear matter in β-equilibrium. At the beginning of the chapter we showed how to extend our approach to the strange sector. Using an extension for the Skyrme parameterization, we showed results for the equation of state, the effective mass and the effective potential. Interestingly, the energy per particle shows a local minimum at a strangeness fraction Y_Λ of about $Y_\Lambda \simeq 0.15$. However, the higher mass of the Λ-hyperons is responsible for the absence of Λ-hyperons in nuclear matter under normal conditions. For the mean-field properties we choose the SLy10+LYI+SLL2 and the SkI3+YBZ6+SLL2 Skyrme parameter sets for the NN, NΛ and $\Lambda\Lambda$ inter-action. For nucleons we observe an increase of the effective mass with increasing strangeness fraction. The situation for the Λ-hyperons is different and the behavior

depends on the chosen Skyrme parameterization. While for the SLy10+LYI+SLL2 Skyrme parameterization sets the mass decreases with increasing strangeness fraction, the opposite is true for the SkI3+YBZ6+SLL2 parameter sets,i.e. with increasing strangeness the mass increases nearly linearly. Since the Λ-hyperons do not couple to the pions, the interaction matrix element of the ΛN and $\Lambda\Lambda$ interaction matrix element is directely obtained by a weighted sum from the Landau-Migdal parameters of the Skyrme energy density functional. On a qualitative level the NN and the ΛN interaction matrix elements are increasing with increasing strangeness fraction Y_Λ, while the $\Lambda\Lambda$ interaction matrix element is decreasing. The ΛN and the $\Lambda\Lambda$ interaction matrix elements depends quantitatively very much on the chosen parameter sets. The matrix element for ΛN is between $8 - 17\%$ of NN interaction matrix element the for the parameter sets LYI-LYIV (upper panel) and even lower for the parameter sets YBZ1, YBZ5, YBZ6. While the coupling of the Λ-N interaction seems to be underestimated, the $\Lambda\Lambda$ interaction seems to be overestimated and is larger than the Λ-N interaction. Especially this overestimation of the $\Lambda\Lambda$ interaction matrix element reflects the limited amount of experimental data for interaction of the Λ-hyperon in the medium. Having more experimental data would help to improve the Skyrme density functional in the hypernuclear sector.

We kept the total baryon number fixed by varying the strangeness fraction to examine the influence of dynamical correlations in hypernuclear matter. Qualitatively, the results for the width, the spectral function and the momentum distribution of the nucleons and Λ-hyperons are similar to those found in nuclear matter. Quantitatively, the Λ-hyperons are less correlated since the interaction strength is reduced, while the correlations of the nucleons are of the same order as in nuclear matter. Thus Λ-hyperons show a smaller width, a sharper structure of the spectral function and a less pronounced high energy tail of the momentum distribution than the nucleons. This observation agrees perfectly well with the sharp spectral structure seen in hypernuclear spectra e.g. [Hot01].

The situation in β-equilibriated nuclear matter is different. To observe the role of correlations we, calculated the particle fractions using the SLy10+LYI+SLL2 and the SkI3+YBZ6+SLL2 Skyrme parameter sets for the NN, NΛ and the $\Lambda\Lambda$ interaction, which were found by Mornas [Mor05] to describe the properties of neutron stars the best. The particle fraction shows a strong dependence on the Skyrme parameterization used. For SLy10+LYI+SLL2 the Λ-hyperons appear at higher densities and are less abundant than for SkI3+YBZ6+SLL2. Also the excess of neutrons is higher using SLy10+LYI+SLL2 than SkI3+YBZ6+SLL2. This observation is directly related to properties of the equation of state: a stiffer equation of state reaches the required energy for hyperon formation at lower density. The particle width and the spectral function resemble qualitative the same properties as in nuclear matter. It is, however, surprising that the width of the neutrons is about the same size as the hyperons rather the protons. This can be explained by the high excess of neutrons in

β-equilibrated nuclear matter, as already seen in neutron rich matter, Pauli-blocking leads to a decrease of the neutrons. This observation is confirmed when we examine the quasiparticle strength at the Fermi-edge as a function of the density. This shows that the correlations in our approach are connected directly to the abundance of the particles and the available phase space rather than the details of the interaction.

In future it will be of interest to also include the other hyperons, especially the Σ-hyperons, to our approach and observe the results at finite temperature T. Also a examination of the equation of state including dynamical correlation might be of helpfull for the better understanding of neutron stars.

A Feynman Diagrams

For convenience we give here a summary of Feynman rules according to Ref. [FW71].

A.1 Feynman Diagrams in Coordinate Space

1. Draw all topologically distinct connected diagrams with n interaction lines V ans $2n + 1$ directed Green's functions G_0.

2. Label each vertex with a four-dimensional space-time point $x_i = (\vec{r}_i, t_i)$.

3. Each solid line represents a Green's function $G_0(x_1, x_2)$ running from x_2 to x_1.

$$x_2 \bullet \xrightarrow{\quad G_0(x_1, x_2) \quad} \bullet\, x_1$$

$$\text{(A.1)}$$

This corresponds according to Eq. (2.6) to a propagation of a particle for $t_1 > t_2$ and a propagation of a hole for $t_1 < t_2$.

$$x_2 \bullet \xrightarrow{\quad G_0^>(x_1, x_2) \quad} \bullet\, x_1 \qquad\qquad x_2 \bullet \xleftarrow{\quad G_0^<(x_1, x_2) \quad} \bullet\, x_1$$

$$t_1 > t_2 \qquad\qquad\qquad t_1 < t_2$$

$$\text{(A.2)}$$

4. Each wavy line represents an interaction $U(x_1, y_1) = V(\vec{r}_1, \vec{r}_2)\delta(t_1 - t_2)$.

$$x_1 \bullet\!\!\sim\!\!\sim\!\!\sim\!\!\sim\!\!\sim\!\!\bullet\; x_2 \qquad \overset{U(x_1, x_2)}{}$$

$$(A.3)$$

5. Integrate all internal variables over space and time.

6. There is a spin matrix product along each continuous fermion line, including the potentials at each vertex.

7. Affix a sign factor $(-1)^F$ to each term, where F is the number of closed fermion loops in the diagram.

8. To compute $G(x_1, x_2)$ assign a factor $(i\hbar)^n$ to each nth-order term.[1]

9. A Green's function with equal time variables must be interpreted as $G_0(\vec{r}_1, t_1, \vec{r}_2, t_1^+)$.

A.2 Feynman Diagrams in Momentum Space

1. Draw all topologically distinct connected diagrams with n interaction lines V ans $2n + 1$ directed Green's functions.

2. Assign a direction to each interaction line, whereas hole lines point in the opposite direction than particle lines. Associate a directed four-momentum with each line and conserve four-momentum at each vertex.

3. Each particle line corresponds to a factor $G_0^>(\vec{k}, \omega)$ and each hole line to a factor $G_0^>(\vec{k}, \omega)$.

$$
\begin{array}{cc}
\xrightarrow{\;\;k\;\;} & \xleftarrow{\;\;k\;\;} \\[4pt]
G_0^>(\vec{k}, \omega) & G_0^<(\vec{k}, \omega)
\end{array}
$$
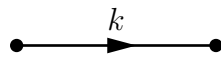
$$(A.4)$$

---

[1] Different from Ref. [FW71], see Eq. (2.41).

4. Each interaction corresponds to a factor $U(k) = V(\vec{k})$.

5. Perform a spin summation along each continuous particle (hole) line including the potential at each vertex.

6. Integrate over the n independent internal four-momenta

7. Affix a factor $(i\hbar)^n (2\pi)^{-4n} (-1)^F$ where F is the number of closed fermion loops.

8. Any single-particle line that forms a closed loop or that is linked by the same interaction line is interpreted as $e^{i\omega\eta} G_0(\vec{k}, \omega)$, where $\eta \to 0^+$ at the end of the calculation.

B Landau-Migdal Parameters

Explit expressions for the Landau-Migdal parameters taken from [Mor05].

Spin $S = 0$ channel:

$$f_{nn} = \frac{1}{2}t_0(1 - x_0) + \frac{1}{12}t_3\rho_N^\alpha + \frac{1}{3}\alpha t_3\rho_N^{\alpha-1}\left[(1 + \frac{x_3}{2})\rho_N - (\frac{1}{2} + x_3)\rho_n\right] \tag{B.1}$$

$$+ \frac{1}{12}\alpha(\alpha - 1)t_3\rho_N^{\alpha-2}\left[(1 + \frac{x_3}{2})\rho_N^2 - (\frac{1}{2} + x_3)(\rho_n^2 + \rho_p^2)\right]$$

$$+ \frac{1}{4}\left[t_1(1 - x_1) + 3t_2(1 + x_2)\right]k_{F_n}^2 + \frac{3}{8}u_3(1 + \frac{y_3}{2})\beta(\beta + 1)\rho_N^{\beta-1}\rho_\Lambda + \frac{1}{4}\lambda_3\gamma(\gamma - 1)\rho_N^{\gamma-2}\rho_\Lambda^2$$

$$f_{np} = t_0(1 + \frac{x_0}{2}) + \frac{1}{6}t_3\rho_N^\alpha(1 + \frac{x_3}{2}) + \frac{1}{4}\alpha t_3\rho_N^\alpha \tag{B.2}$$

$$+ \frac{1}{12}\alpha(\alpha - 1)t_3\rho_N^{\alpha-2}\left[(1 + \frac{x_3}{2})\rho_N^2 - (\frac{1}{2} + x_3)(\rho_n^2 + \rho_p^2)\right]$$

$$+ \frac{1}{4}\left[t_1(1 + \frac{x_1}{2}) + t_2(1 + \frac{x_2}{2})\right](k_{F_p}^2 + k_{F_n}^2)$$

$$+ \frac{3}{8}u_3(1 + \frac{y_3}{2}\beta(\beta + 1)\rho_N^{\beta-1}\rho_\Lambda + \frac{1}{4}\lambda_3\gamma(\gamma - 1)\rho_N^{\gamma-2}\rho_\Lambda^2$$

$$f_{pp} = \frac{1}{2}t_0(1 - x_0) + \frac{1}{12}t_3\rho_N^\alpha + \frac{1}{3}\alpha t_3\rho_N^{\alpha-1}\left[(1 + \frac{x_3}{2})\rho_N - (\frac{1}{2} + x_3)\rho_p\right] \tag{B.3}$$

$$+ \frac{1}{12}\alpha(\alpha - 1)t_3\rho_N^{\alpha-2}\left[(1 + \frac{x_3}{2})\rho_N^2 - (\frac{1}{2} + x_3)(\rho_n^2 + \rho_p^2)\right]$$

$$+ \frac{1}{4}\left[t_1(1 - x_1) + 3t_2(1 + x_2)\right]k_{F_p}^2 + \frac{3}{8}u_3(1 + \frac{y_3}{2})\beta(\beta + 1)\rho_N^{\beta-1}\rho_\Lambda + \frac{1}{4}\lambda_3\gamma(\gamma - 1)\rho_N^{\gamma-2}\rho_\Lambda^2$$

$$f_{n\Lambda} = \frac{1}{2}u_0(2 + y_0) + \frac{3}{16}u_3(2 + y_3)(1 + \beta)\rho_N^\beta \tag{B.4}$$

$$+ \frac{1}{8}\left[u_1(2 + y_1) + u_2(2 + y_2)\right](k_{F_\Lambda}^2 + k_{F_n}^2) + \frac{1}{2}\lambda_3\gamma\rho_N^{\gamma-1}\rho_\Lambda$$

$$f_{p\Lambda} = \frac{1}{2}u_0(2 + y_0) + \frac{3}{16}u_3(2 + y_3)(1 + \beta)\rho_N^\beta \tag{B.5}$$

$$+ \frac{1}{8}\left[u_1(2 + y_1) + u_2(2 + y_2)\right](k_{F_\Lambda}^2 + k_{F_p}^2) + \frac{1}{2}\lambda_3\gamma\rho_N^{\gamma-1}\rho_\Lambda$$

$$f_{\Lambda\Lambda} = \frac{1}{2}\lambda_0 + \frac{1}{2}\lambda_3\rho_N^\gamma + \frac{1}{4}[\lambda_1 + 3\lambda_2]k_{F_\Lambda}^2 \tag{B.6}$$

Spin S=1 channel:

$$g_{nn} = \frac{1}{2}(x_0 - 1) + \frac{1}{12}t_3\rho_N^\alpha(x_3 - 1) + \frac{1}{4}[t_1(x_1 - 1) + t_2(1 + x_2)]k_{F_n}^2 \qquad \text{(B.7)}$$

$$g_{np} = \frac{1}{2}t_0x_0 + \frac{1}{12}t_3x_3\rho_N^\alpha + \frac{1}{8}[t_1x_1 + t_2x_2](k_{F_n}^2 + k_{F_p}^2) \qquad \text{(B.8)}$$

$$g_{pp} = \frac{1}{2}(x_0 - 1) + \frac{1}{12}t_3\rho_N^\alpha(x_3 - 1) + \frac{1}{4}[t_1(x_1 - 1) + t_2(1 + x_2)]k_{F_p}^2 \qquad \text{(B.9)}$$

$$g_{n\Lambda} = \frac{1}{2}u_0y_0 + \frac{3}{16}u_3y_3\rho_N^\beta + \frac{1}{8}[u_1y_1 + u_2y_2]((k_{F_\Lambda}^2 + k_{F_n}^2) \qquad \text{(B.10)}$$

$$g_{p\Lambda} = \frac{1}{2}u_0y_0 + \frac{3}{16}u_3y_3\rho_N^\beta + \frac{1}{8}[u_1y_1 + u_2y_2]((k_{F_\Lambda}^2 + k_{F_p}^2) \qquad \text{(B.11)}$$

$$g_{\Lambda\Lambda} = -\frac{1}{2}\lambda_0 - \frac{1}{2}\lambda_3\rho_N^\gamma + \frac{1}{4}[-\lambda_1 + \lambda_2]k_{F_\Lambda}^2 \qquad \text{(B.12)}$$

List of Figures

List of Tables

Bibliography

[A+08]   C. Amsler et al., *Review of particle physics*, Phys. Lett. **B667** (2008), 1.

[APR98]   A. Akmal, V. R. Pandharipande, and D. G. Ravenhall, *The equation of state for nucleon matter and neutron star structure*, Phys. Rev. **C58** (1998), 1804–1828.

[AS72]   Milton Abramowitz and Irene A. Stegun, *Handbook of Mathematical Functions*, Dover Publications, New York **9th edition** (1972).

[BB00]   Sarmistha Banik and Debades Bandyopadhyay, *Nuclear symmetry energy in presence of hyperons in the nonrelativistic Thomas-Fermi approximation*, J. Phys. **G26** (2000), 1495–1506.

[BD67]   J.D. Bjorken and S.D. Drell, *Relativistische Quantenfeldtheorie*, B.I.-Hochschultaschenbuch **Band 101** (1967).

[BF00]   Omar Benhar and Adelchi Fabrocini, *Two-Nucleon Spectral Function in Infinite Nuclear Matter*, Phys. Rev. **C62** (2000), 034304.

[BFF89]   O. Benhar, A. Fabrocini, and S. Fantoni, *THE NUCLEON SPECTRAL FUNCTION IN NUCLEAR MATTER*, Nucl. Phys. **A505** (1989), 267–299.

[BFF92]   _____, *Nuclear matter Green functions in correlated-basis theory*, Nucl. Phys. **A550** (1992), 201.

[BFvGQ75] M. Beiner, H. Flocard, Nyguyen van Giai, and P. Quentin, *Nuclear ground state properties and selfconsistent calculations with the Skyrme interactions: 1. Spherical description*, Nucl. Phys. **A238** (1975), 29–69.

[BG97]   Shmuel Balberg and Avraham Gal, *An effective equation of state for dense matter with strangeness*, Nucl. Phys. **A625** (1997), 435–472.

[BM90]   Wim Botermans and Rudi Malfliet, *Quantum transport theory of nuclear matter*, Phys. Rept. **198** (1990), 115–194.

[Boz04]   P. Bozek, *Short-range correlations in asymmetric nuclear matter*, Phys. Lett. **B586** (2004), 239–243.

[BQB⁺82]   J. Bartel, P. Quentin, M. Brack, C. Guet, and H. B. Hakansson, *Towards a better parametrisation of Skyrme-like effective forces: A Critical study of the SkM force*, Nucl. Phys. **A386** (1982), 79–100.

[CBH⁺98]   E. Chabanat, P. Bonche, P. Haensel, J. Meyer, and R. Schaeffer, *A Skyrme parametrization from subnuclear to neutron star densities. 2. Nuclei far from stablities*, Nucl. Phys. **A635** (1998), 231–256.

[CdAPS91]   Claudio Ciofi degli Atti, E. Pace, and G. Salme, *Y scaling analysis of quasielastic electron scattering and nucleon momentum distributions in few body systems, complex nuclei and nuclear matter*, Phys. Rev. **C43** (1991), 1155–1176.

[CdAS96]   Claudio Ciofi degli Atti and S. Simula, *Realistic model of the nucleon spectral function in few and many nucleon systems*, Phys. Rev. **C53** (1996), 1689.

[CH03]   R. Cools and A. Haegemans, *CUBPACK: a package for automatic cubature; framework description*, ACM Trans. Math. Sotfw. **29** (2003), 287.

[CMB⁺97]   E. Chabanat, J. Meyer, P. Bonche, R. Schaeffer, and P. Haensel, *A skyrme parametrization from subnuclear to neutron star densities*, Nucl. Phys. **A627** (1997), 710–746.

[DB04]   W. H. Dickhoff and C. Barbieri, *Self-consistent green's function method for nuclei and nuclear matter*, Prog. Part. Nucl. Phys. **52** (2004), 377–496.

[DG80]   J. Dechargé and D. Gogny, *Hartree-Fock-Bogolyubov calculations with the D1 effective interaction on spherical nuclei*, Phys. Rev. **C21** (1980), no. 4, 1568–1593.

[DH90]   A. E. L Dieperink and P. K. A Huberts, *On high resolution (e,e,p) reactions*, Ann. Rev. Nucl. Part. Sci. **40** (1990), 239–284.

[DVN05]   Willem H. Dickhoff and Dimitri Van Neck, *Many-Body Theory Exposed!*, World Scientific, New Jersey (2005).

[dWH90]   P. K. A. de Witt Huberts, *Proton spectral functions and momentum distributions in nuclei from high resolution (e, e-prime p) experiments*, J. Phys. **G16** (1990), 507–544.

[Fed09]   A. Fedoseew, *private communication*.

[FLAP89]   F. Fernandez, T. Lopez-Arias, and C. Prieto, *Skyrme Hartree-Fock calculation of Lambda hypernuclear states from (π⁺,K⁺) reactions*, Z. Phys. **A334** (1989), 349–354.

124

[FLM03]   Frank Froemel, Horst Lenske, and Ulrich Mosel, *Short-range correlations in nuclear matter at finite temperatures and high densities*, Nucl. Phys. **A723** (2003), 544–556.

[Foc30]   V. Fock, *Näherungsmethode zur Lösung des quantenmechanischen Mehrkörperproblems*, Z. Phys. **61** (1930), 126.

[Fro06]   Frank Froemel, *Short-range correlations in quark and nuclear matter*, Dissertation, Universität Gießen (2006).

[FW71]   Alexander Fetter and John Dirk Walecka, *Quantum theory of many-particle systems*, McGraw-Hill, New York (1971).

[Gle96]   Norman K. Glendenning, *Compact Stars*, Springer, New York (1996).

[GR86]   E.K.U. Gross and E. Runge, *Vielteilchentheorie*, Teubner, Stuttgart (1986).

[Har28]   D. R. Hartree, *The wave mechanics of an atom with a non-coulomb central field. part i. theory and methods*, Proc. Camb. Philos. Soc. **24** (1928), 89.

[HHH$^+$96]   T. Hasegawa, O. Hashimoto, S. Homma, T. Miyachi, T. Nagae, M. Sekimoto, T. Shibata, H. Sakaguchi, T. Takahashi, K. Aoki, H. Noumi, H. Bhang, M. Youn, Y. Gavrilov, S. Ajimura, T. Kishimoto, A. Ohkusu, K. Maeda, R. Sawafta, and R. P. Redwine, *Spectroscopic study of $^{10}_{\Lambda}B$, $^{12}_{\Lambda}C$, $^{28}_{\Lambda}Si$, $^{89}_{\Lambda}Y$, $^{139}_{\Lambda}La$, and $^{208}_{\Lambda}Pb$ by the (π^+,K^+) reaction*, Phys. Rev. **C53** (1996), no. 3, 1210–1220.

[HJPRM96]   M. Hjorth-Jensen, A. Polls, A. Ramos, and H. Muther, *Self-energy of Lambda in finite nuclei*, Nucl. Phys. **A605** (1996), 458–474.

[HM04]   Kh. S. A. Hassaneen and H. Muther, *Correlations and spectral functions in asymmetric nuclear matter*, Phys. Rev. **C70** (2004), 054308.

[Hot01]   H. and Hotchi, *Spectroscopy of medium-heavy Lambda hypernuclei via the (π^+,K^+)reaction*, Phys. Rev. **C64** (2001), 044302.

[HPY07]   P. Haensel, A.Y. Potekhin, and D.G. Yakovlev, *Neutron Stars 1*, Springer (2007).

[KB62]   L.P. Kadanoff and G. Baym, *Quantum statistical mechanics*, Benjamin, New York (1962).

[KHL00]   C. M. Keil, F. Hofmann, and H. Lenske, *Density dependent hadron field theory for hypernuclei*, Phys. Rev. **C61** (2000), 064309.

[KLM05]   P. Konrad, H. Lenske, and U. Mosel, *Short range correlations and spectral functions in asymmetric nuclear matter*, Nucl. Phys. **A756** (2005), 192–212.

[Kon04]   Patrick Konrad, *Kurzreichweitige Korrelationen in asymmetrischer Kernmaterie*, Diploma Thesis, University Giessen (2004).

[KST04]   S. Kamerdzhiev, J. Speth, and G. Tertychny, *Extended theory of finite fermi systems (collective vibrations in closed shell nuclei)*, Phys. Rept. **393** (2004), 1–86.

[KTB80]   H. Krivine, J. Treiner, and O. Bohigas, *Derivation of a fluid dynamic lagrangian and electric giant resonances*, Nucl. Phys. **A336** (1980), 155–184.

[Lan98]   D. E. Lanskoy, *Double-Λ hypernuclei in the Skyrme-Hartree-Fock approach and nuclear core polarization*, Phys. Rev. **C58** (1998), no. 6, 3351–3358.

[LCK08]   Bao-An Li, Lie-Wen Chen, and Che Ming Ko, *Recent Progress and New Challenges in Isospin Physics with Heavy-Ion Reactions*, Phys. Rept. **464** (2008), 113–281.

[Leh03]   Jurgen Lehr, *In-medium properties of nucleons and nuclear resonances in a semi-classical transport model*, PhD thesis, Universität Gießen (2003).

[LEL⁺00]   J. Lehr, M. Effenberger, H. Lenske, S. Leupold, and U. Mosel, *Transport Theoretical Approach to the Nucleon Spectral Function in Nuclear Matter*, Phys. Lett. **B483** (2000), 324–330.

[LLLM02]   J. Lehr, H. Lenske, S. Leupold, and U. Mosel, *Nuclear matter spectral functions by transport theory*, Nucl. Phys. **A703** (2002), 393–408.

[Lut60]   J. M. Luttinger, *Fermi Surface and Some Simple Equilibrium Properties of a System of Interacting Fermions*, Phys. Rev. **119** (1960), no. 4, 1153–1163.

[LY97]   D. E. Lanskoy and Y. Yamamoto, *Skyrme-Hartree-Fock treatment of Λ and ΛΛ hypernuclei with G-matrix motivated interactions*, Phys. Rev. **C55** (1997), no. 5, 2330–2339.

[MDG88]   D. J. Millener, C. B. Dover, and A. Gal, *Lambda Nucleus Single Particle Potentials*, Phys. Rev. **C38** (1988), 2700–2708.

[Mig57]   A. Migdal, Sov. Phys. JETP **5** (1957), 333.

[Mig75]   A.B. Migdal, *Theory of Finite Fermi Systems and Applications to Atomic Nuclei*, Bemjamin, New York (1975).

[Mor05]   L. Mornas, *Neutron stars in a Skyrme model with hyperons*, Eur. Phys. J. **A24** (2005), 293–312.

[NcvacVFR02] T. Nikšić, D. Vretenar, P. Finelli, and P. Ring, *Relativistic hartree-bogoliubov model with density-dependent meson-nucleon couplings*, Phys. Rev. **C66** (2002), no. 2, 024306.

[Neg82]   John W. Negele, *The mean-field theory of nuclear structure and dynamics*, Rev. Mod. Phys. **54** (1982), 913–1015.

[Nol02]   W. Nolting, *Grundkurs Theoretische Physik 7: Viel-Teilchen-Theorie*, Springer **Berlin** (2002).

[OV39]   J. R. Oppenheimer and G. M. Volkoff, *On Massive Neutron Cores*, Phys. Rev. **55** (1939), no. 4, 374–381.

[P+91]   P. H. Pile et al., *Study of hypernuclei by associated production*, Phys. Rev. Lett. **66** (1991), 2585–2588.

[PN66]   David Pines and Philippe Nozieres, *The Theory of Quantum Liquids*, Bemjamin, New York (1966).

[PSH97]   Vijay R. Pandharipande, Ingo Sick, and Peter K. A. deWitt Huberts, *Independent particle motion and correlations in fermion systems*, Rev. Mod. Phys. **69** (1997), 981–991.

[Ray81]   M. Rayet, *Skyrme parametrization of an effective lambda nucleon interaction*, Nucl. Phys. **A367** (1981), 381–397.

[RD92]   N. Rudra and J.N. De, *Landau parameters for asymmetric nuclear matter with a finite-range density-dependent interaction*, Nucl. Phys. **A545** (1992), 608–622.

[RD04]   N. J. Robertson and W. H. Dickhoff, *Correlation effects on Lambda propagation in nuclear matter*, Phys. Rev. **C70** (2004), 044301.

[RDP91]   A. Ramos, W. H. Dickhoff, and A. Polls, *Binding energy and momentum distribution of nuclear matter using Green's function methods*, Phys. Rev. **C43** (1991), 2239–2253.

[RF95]   P. G. Reinhard and H. Flocard, *Nuclear effective forces and isotope shifts*, Nucl. Phys. **A584** (1995), 467–488.

[RPD89]   A. Ramos, A. Polls, and W. E. Dickhoff, *Single-particle properties and short-range correlations in nuclear matter*, Nucl. Phys. **A503** (1989), 1.

Bibliography

[RSY99]   T. A. Rijken, V. G. J. Stoks, and Y. Yamamoto, *Soft-core hyperon nucleon potentials*, Phys. Rev. **C59** (1999), 21–40.

[Sjo76]   O. Sjoberg, *On the Landau Effective Mass in Asymmetric Nuclear Matter*, Nucl. Phys. **A265** (1976), 511.

[Sky59]   T. Skyrme, *The effective nuclear potential*, Nucl. Phys. **9** (1959), 615–634.

[SR07]   J. R. Stone and P. G. Reinhard, *The Skyrme Interaction in finite nuclei and nuclear matter*, Prog. Part. Nucl. Phys. **58** (2007), 587–657.

[TBFP84]   F. Tondeur, M. Brack, M. Farine, and J.M. Pearson, *Static nuclear properties and the parametrisation of the Skyrme forces*, Nucl. Phys. **A420** (1984), 297–319.

[VB72]   D. Vautherin and D. M. Brink, *Hartree-Fock calculations with Skyrme's interaction. 1. Spherical nuclei*, Phys. Rev. **C5** (1972), 626–647.

[Wei35]   Weizsäcker, C. F. V., *Zur Theorie der Kernmassen*, Z. Phys. **96** (1935), 431–458.

[Wro04]   A. K. Wroblewski, *Hypernuclei (and strange particles): How it all began?*, Acta Phys. Polon. **B35** (2004), 901–927.

[YBZ88]   Y. Yamamoto, H. Bando, and J. Zofka, *On the Lambda hypernuclear single particle energies*, Prog. Theor. Phys. **80** (1988), 757–761.

[Ynd98]   Ynduráin, *The Theory of Quark and Gluon Interactions*, Springer, Berlin (1998).

Deutsche Zusammenfassung

In den letzten Jahren ist das Interesse an Korrelationen in Atomkernen weiter gewachsen. Viele Eigenschaften von Atomkernen, wie etwa die Bindungsenergien, können zwar mit Hilfe der Annahme unabhängiger Teilchen, die sich in einem mittleren Potential bewegen, beschrieben werden. Allerdings zeigt sich in Experimenten bei denen ein oder zwei Nukleonen aus einem Atomkern durch ein einlaufendes Elektron heraus gestoßen werden [CdAPS91, DH90], dass sich die Nukleonen im Atomkern alles andere als unabhängig bewegen, es gibt sogenannte Korrelationen. Theoretisch wurden bisher Korrelationen in symmetrischer Kernmaterie bei der Temperatur $T = 0$ (z.B. [RPD89, RDP91, BFF92]) und bei endlicher Temperatur (z.B. [FLM03]) untersucht. Mittlerweile gibt es auch Rechnungen in asymmetrischer Kernmaterie mit einem hohen Überschuss an Neutronen [Boz04, HM04, KLM05]. Ein guter Überblick über die bisher verwendeten theoretischen Modelle gibt [DB04].

Über die Rolle, die Korrelationen von Nukleonen und Hyperonen in Neutronensternen spielen, ist bisher noch wenig bekannt. Hyperonen sind Baryonen, die mindestens ein Strange-Quark enthalten, sie treten vor allem in Materie unter extremen Bedingungen auf, wie es zum Beispiel in Neutronensternen oder Schwerionenkollisionen der Fall ist. Es gibt zwar theoretische Untersuchungen, die sich mit Korrelationen von einzelnen Λ-Hyperonen, dem leichtesten der Hyperonen, in unendlich ausgedehnter Kernmaterie beschäftigen [HJPRM96, RD04], allerdings fehlen bisher systematische Untersuchungen von Korrelationen in Systemen mit einem hohen Anteil von Hyperonen sogenannter Hyperkernmaterie.

Ziel dieser Arbeit ist es, die Rolle von dynamischen Korrelationen in Hyperkernmaterie und in Kernmaterie im β-Gleichgewicht zu untersuchen. Dazu berechnen wir die dynamischen Selbstenergien und die Spektralfunktionenen der Baryonen selbstkonsistent. Dabei nähern wir die Selbstenergie mit der 1-Teilchen-2-Loch und der 2-Teilchen-1-Loch Polarisations-Selbstenergie und vernachlässigen Terme höhere Ordnung. Den Anteil des mittleren Baryonenfeldes wird mit Hilfe einer modernen Skyrme Parametrisierung des Energiedichtefunktionals in unsere Rechnungen integriert. Für die Wechselwirkung der Baryonen nehmen wir eine Punktwechselwirkung an, welche sich bei Rechnungen von J. Lehr [LEL$^+$00, LLLM02] als sinnvoll erwiesen hat. Informationen über die Stärke der Wechselwirkung erhalten wir aus dem Skyrme Energiedichtefunktional. Dazu benutzen wir die Theorie der Fermiflüssigkeiten und bestimmen die Restwechselwirkung aus dem Energiedichtefunktional. Um nur

dem kurzreichweitigen Anteil der Wechselwirkung Rechnung zu tragen, berechnen wir den Anteil der Pionen, welche wir mit dem langreichweitigen Anteil identifizieren, und subtrahieren diesen von der Restwechselwirkung welche wir aus dem Energiedichtefuntional erhalten haben.

Nach einer allgemeinen Einführung in die Vielteilchen-Theorie und die Theorie der Greens Funktionen in Kapitel 2, untersuchen wir in Kapitel 3 die Skryme Parametrisierung des Energiedichtefunktionals. Dafür vergleichen wir verschiedene Eigenschaften des mittleren Feldes, wie die Zustandsgleichung, den Kompressibilitätskoeffizent, die Asymmetrieenergie, die effektive Masse und das effektive Potential für die SLy10, SkI3 und die SkM* Parametrisierungen. Es zeigt sich, dass die Eigenschaften von unendlicher Kernmaterie, wie die Sättigungsdichte, die Bindungsenergie und der Kompressibilitätskoeffizent, sehr gut von diesen Parametrisierungen beschrieben werden. Ein Vergleich der Zustandsgleichung, welche wir mit der SLy10 Skyrme Parametrierstation erhalten, mit Ergebnissen der Zustandsgleichungen des Urbana Modells [APR98], zeigt auch dort eine gute Übereinstimmung für symmetrische Kern- und reine Neutronenmaterie.

Im Kapitel 4 beschäftigen wir uns mit dem mittleren Wechselwirkungs-Matrixelement, welches wir für unsere Rechnungen verwenden. Aus dem Energiedichtefunktional berechnen wir die Landau-Migdal Parameter, welche einer Wechselwirkung an der Fermikante entsprechen. Nach dem Subtrahieren des langreichweitigen Pionen-Anteils von der Nukleonen-Restwechselwirkung, erhalten wir das Wechselwirkungs-Matrixelement durch eine Mittelung über die Spin-Freiheitsgarde. Es zeigt sich, dass die Subtraktion des Pionen-Anteil zu einer Erhöhung der Wechselwirkung führt. Qualitativ zeigen die Wechselwirkungs-Matrixelemente das gleiche Verhalten für die verschiedenen Skyrme Parametrisierungen: mit zunehmender Dichte wird die Wechselwirkung kleiner. Dies kann man damit erklären, dass mit zunehmender Dichte mehr Zustände besetzt sind und daher durch das Pauliprinzip geblockt werden. Quantitativ zeigt allerdings die Stärke der Wechselwirkungs-Matrixelemente leichte Abweichungen für die verschiedenen Skyrme Parametrisierungen.

Die Ergebnisse für Nukleon Breite,die Spektralfunkion, die Impulsverteilung und den Spetroskopischen Faktor für unendlich ausgedehnte Kernmaterie und verschiedene Skyrme Parametrisierungen haben wir in Kapitel 5 untersucht. Die Resultate der Breite in symmetrischer Kernmaterie zeigen dabei ein sehr gute Übereinstimmung für alle betrachteten Skyrme Parametrisierungen und stimmen quantitativ mit dem aus der Vielteilechen-Theorie zu erwartenden Verhalten überein. Leichte Abweichungen der Breiten für verschiedene Skyrme Parametrisierung ergeben sich allerdings für sehr hohe Energien. Ein Vergleich der Nukleonen Breite in neutronenreicher Kernmaterie zeigt, dass dort die Abweichungen etwas größer sind, wenn man verschiedene Skyrme Parametrisierungen benutzt. Allerdings treten solche Abwei-

chungen auch bei anderen vielteilchentheoretischen Rechnungen auf, wenn verschiedene Nukleon-Nukleon-Wechselwirkungen benutzt werden (z.B. [HM04]).

Ein Vergleich von unseren Ergebnissen mit den Ergebnissen einer Brückner-Hartree-Fock (BHF) Rechung von [HM04] zeigt, dass es auch für neutronenreiche Kernmaterie ein gute qualitative Übereinstimmung gibt. Lediglich quantitativ gibt es Abweichungen, die aber vergleichbar mit den Abweichungen für verschiedene Nukleon-Nukleon-Wesechlewirkungen bei der BHF Rechung von [HM04] sind.

Auch die Spektralfunktionen zeigen ein realistisches Verhalten, wie es aus der Vielteilchen-Theorie bekannt ist. Man sieht einen scharfen Quasiteilchen Pol mit ausgeprägter spektralen Verteilung. Während die Lage des Quasiteilchen Pols durch das mittlere Nukleonfeld gegeben ist, wird die spektrale Verteilung durch die Breite der Nukleonen bestimmt. Die Impulsverteilung der Nukleoen zeigt, dass im Vergleich mit einer Fermi-Verteilung die Zustände in der Fermikugel reduziert und zu höherem Implus verschoben werden. Auch dieser Effekt ist aus der Vielteilchen-Theorie bekannt. Ein Vergleich mit den Ergebnisse von [Leh03] and [BFF92] zeigt, dass die Subtraktion des langreichweitigen Pionen-Anteils für unser Modell eine große Rolle spielt. Während die Ergebnisse mit der Subtraktion des langreichweitigen Anteils gut mit den Ergebnissen von [Leh03] and [BFF92] übereinstimmen, ist der Effekt der Entvölkerung des Fermisees für Rechnungen ohne diese Subtraktion zu klein. Ein Vergleich der Implusverteilung für Protonen und Neutronen in neutronenreicher Kernmaterie zeigt, dass weniger Neutronen zu höhren Impulsen verschoben werden als dies für die Protonen der Fall ist. Dieser Effekt wurde auch bei den BHF Rechnungen von [HM04] beobachtet und durch die Tensorwechselwirkung des Nukleon-Nukleon-Potentials erklärt. In unserem Modell können wir darüber keine Aussage machen, da in unseren Rechnungen die Tensorwechselwirkung nicht explizit auftritt.

Am Ende des Kapitels untersuchen wir den Spektroskopischen Faktor in Kernamterie. Der Spektroskopischen Faktor sagt aus, wie viele Zustände in einem Quasiteilchenzustand bleiben und sich nicht in anderen Vielteilchen Zuständen befinden. Daher ist der Spektroskopische Faktor umgekehrt proportional mit der Anzahl der Korrelationen, je stärker ein System korreliert ist, desto niedriger ist der Spektroskopische Faktor. Er beträgt eins für ein unkorreliertes System. In Übereinstimmung mit [Leh03] und [BFF92] ist der Spektroskopische Faktor nur nahe der Fermikante stark von eins abweichend. Diese Beobachtung bestätigt unsere Annahme einer Punktwechselwirkung an der Fermikante.

Schließlich untersuchen wir in Kapitel 6 Korrelationen ind Hyperkernmaterie und in Kernmaterie im β-Gleichgewicht. Dazu benutzen wir eine Erweiterung der Skyrme Parametrisierung, welche auch die Λ-Hyperonen enthält. Es zeigt sich dabei, dass das lokale Minimum der Bindungsenergie bei einem Strangeness-Verhältnis $Y_\Lambda \simeq 0.15$ liegt, allerdings sorgt die höhere Masse der Λ-Hyperonen dafür, dass

unter normalen Bedingungen keine Hyperonen in der Materie vorhanden sind. Um die Eigenschaften des mittleren Baryonenfeldes zu untersuchten, benutzten wir die SLy10+LYI+SLL2 und die SkI3+YBZ6+SLL2 Parametrisierung für die NN-, ΛN- und $\Lambda\Lambda$-Wechselwirkung. Es zeigt sich dabei, dass die effektive Masse für die Nukleonen mit steigendem Strangeness-Verhältnis zunimmt. Hingegen hängt die effektive Masse für die Λ-Hyperonen von der verwendeten Parametrisierung ab. Da die Λ-Hyperonen nicht an die Pionen koppeln, erhalten wir das Wechselwirkungs-Matrixelement direkt aus den Landau-Migdal Parametern des Energiedichtefunktionals, ohne dass wir den Pionen Anteil abziehen. Qualitativ werden die NN- und und die ΛN-Wechselwirkungs-Matrixelemnte größer mit steigendem Strangeness-Verhältnis, während das $\Lambda\Lambda$-Matrixelemnt kleiner wird. Quantitativ hängt die Größe der ΛN- und der $\Lambda\Lambda$-Matrixelemente von der gewählten Skyrme Parametrisierung ab. Die Parametersätze LYI-LYIV ergeben dabei etwas $8-17\%$ der NN-Wechselwirkung und die Parametersätze YBZ1, YBZ5, YBZ6 sogar noch niedriger Werte. Während die ΛN-Wechselwirkungs Matrixelement scheinbar unterschätzt wird, wird das $\Lambda\Lambda$-Matrixelemente überschätzt und es ist sogar größer als das ΛN-Matrixelement. Diese Abweichung hängt mit dem beschränkten Zugang zu experimentellen Daten über die Wechselwirkung Λ-Hyperonen im Medium zusammen. Mit mehr experimentellen Daten könnte man die Parameter des Skyrme Energiedichefunktionals besser bestimmen.

Um Korrelationen in Hyperkernmaterie zu untersuchen, halten wir die Dichte der Baryonen konstant und variieren das Strangeness-Verhältnis. Qualitativ stimmen die Ergebnisse der Breite und der Spektralfunktion für die Nukleonen und Λ-Hyperonen mit denen in Kernmaterie überein. Quantitativ zeigen die Λ-Hyperonen weniger Korrelationen, da ihre Wechselwirkung mit den anderen Baryonen im Vergleich zu den Nukleonen reduziert ist. Daher zeigen die Λ-Hyperonen eine kleinere Breite, eine schärfer ausgeprägte Spektralfunktion und weniger Zustände oberhalb der Fermikante. Diese Beobachtung stimmt gut mit in Experimenten gesehen scharfen Strukturen in Hyperkernspektren überein [Hot01].

Es zeigt sich, dass die Situation für Kernmaterie im β-Gleichgewicht etwas anders ist. Um die Teilchenverhältnisse in Kernmaterie zu berechnen benutzen wir die SLy10+LYI+SLL2 und die SkI3+YBZ6+SLL2 Skyrme Parametrisierung, da diese Auswahl der Skyrme Parametrisierungen die Eigenschaften von Neutronensternen am besten beschreibt [Mor05]. Die Teilchenverhältnisse zeigen dabei eine große Abhängigkeit von der gewählten Parametrisierung. Für die SLy10+LYI+SLL2 Parametrisierung setzt die Bildung der Λ-Hyperonen bei eine höheren Dichte ein und die Anzahl der Λ-Hyperonen ist geringer als bei der SkI3+YBZ6+SLL2 Skyrme Parametrisierung. Gleichzeitig ist aber die Anzahl der Neutronen mit der SLy10+LYI+SLL2 Parametrisierung höher als mit SkI3+YBZ6+SLL2. Diese Beobachtungen sind direkt mit den Eigenschaften der Zustandsgleichung verbunden, eine steifere Zustandsgleichung erreicht die Energie zur Hyperonenbildung bei einer geringeren

Dichte. Qualitativ zeigen die Breite der Teilchen und die Spektralfunktion wiederum dieselben Eigenschaften wie in Hyperkernmaterie. Es überrascht allerdings, dass die Breit der Neutronen von derselben Größenordnung wie die Breit der Λ-Hyperonen und nicht wie die der Protonen ist. Diese Tatsache läßt sich durch den hohen Anteil an Neutronen in Kernmaterie im β-Gleichgewicht erklären. Dies führt dazu, dass ein großer Anteil der Neutronen durch das Pauli-Prinzip geblockt ist und führt zu weniger Korrelationen. Dieses Resultat wird auch durch den Spetroskopischen Faktor an der Fermi-Kante bestätigt. Die Korrelationen in unserem Modell werden eher durch den zur Verfügung stehenden Phasenraum und nicht von den Details der Wechselwirkung bestimmt.

Von zukünftigen Interesse ist eine Erweiterung unseres Modells um die restlichen Hyperonen, spezielle die Σ-Hyperonen. Auch Rechnungen bei endlichen Temperaturen würden zu einem besseres Verständnis von Neutronensternen beitragen.

Danksagung